

LOADED AND ELABORATED POLYESTER NANOMATERIALS FOR THE
TREATMENT AND DIAGNOSIS OF DISEASE

by

Anthony John Fowler

A dissertation submitted to the faculty of
The University of North Carolina at Charlotte
in partial fulfillment of the requirements
for the degree of Doctor of Philosophy in
Nanoscale Science

Charlotte

2017

Approved by:

Dr. Craig Ogle

Dr. Thomas Schmedake

Dr. Jerry Troutman

Dr. Juan Luis Vivero-Escoto

Dr. Michael Walter

Dr. Douglas Shafer

©2017
Anthony John Fowler
ALL RIGHTS RESERVED

ABSTRACT

ANTHONY JOHN FOWLER. Loaded and Elaborated Polyester Nanomaterials for the Treatment and Diagnosis of Disease. (Under the direction of CRAIG A. OGLE)

Cancer is not one disease but many. In fact, cancer is a collection of more than 100 different diseases. Cancer is the second leading cause of death in the United States with an estimated 1.7 million new cases expected in 2017 and approximately 600,000 Americans expected to succumb to the disease. While modern chemotherapeutics have provided considerable improvement to patient outcomes, we have yet to develop the “ideal” treatment for cancer. The medical community has long sought the ideal therapeutic – in fact Paul Ehrlich originally coined the concept of the “magic bullet” in the late 1800’s. Nanomedicine is a burgeoning field which can impact nearly every avenue of modern chemotherapeutics. Coupled with biological targeting agents, synthetic nanomaterials have the potential to render Ehrlich’s “magic bullet” concept a reality.

In the first part of this thesis we have developed a new bioconjugation platform, and have applied this technology to the functionalization of nanoparticles (NPs). This platform is unique having; high water solubility, an inherent chromophore for quantification, and is chemically diverse. Further, we have shown that this platform can be utilized in the chemoselective reaction of nucleophilic amines.

In the second part of the thesis we have constructed polyester based nanomaterials composed of poly(lactic-co-glycolic acid) (PLGA) and polycaprolactone (PCL). These nanomaterials were then adorned with a MUC1 specific antibody - TAB004 - and were shown to selectively accumulate at tumor sites in pancreatic cancers *in vivo*.

DEDICATION

For my family...without you this would never have happened.

TABLE OF CONTENTS

LIST OF FIGURES	vii
LIST OF TABLES	x
LIST OF SCHEMES	xi
LIST OF ABBREVIATIONS	xii
CHAPTER 1: Introduction	
1.1 Motivation	1
1.2 Nanotherapeutics a Historical Perspective	2
1.3 Polymeric Nanoparticles	3
1.4 Polyesters	4
1.5 Passive Targeting of Nanoparticles	5
1.6 Active Targeting of Nanoparticles	6
CHAPTER 2: Heterobifunctional Reagents for Bioconjugation	
2.1 Introduction	8
2.2 Experimental Design and Discussion	9
2.3 Conclusion	20
2.4 Materials and Methods	21
CHAPTER 3: Treatment of Pancreatic Ductal Adenocarcinoma with Tumor Antigen Specific-Targeted Delivery of Paclitaxel Loaded PLGA Nanoparticles	
3.1 Introduction	27
3.2 Results and Discussion	29
3.3 Conclusion	48
3.4 Materials and Methods	48
CHAPTER 4: Development of High-Capacity Nanomaterials Through Polymer Drug Conjugates	
4.1 Introduction	59
4.2 Results and Discussion	62
4.3 Conclusion	68
4.4 Materials and Methods	69
CHAPTER 5: Treatment of Bovine Mammary Mastitis with Polyester Nanomaterials	

5.1 Introduction	77
5.2 Results and Discussion	80
5.3 Summary	85
5.4 Materials and Methods	86
REFERENCES	92

LIST OF FIGURES

<i>Figure</i>	<i>Page</i>
Figure 2.1. ORTEP of 2b Crystal Data. C ₁₅ H ₁₇ N ₂ O ₃ Br, M = 353.21, orthorhombic, P na21 (No. 33, a = 7.1025(4) Å, b = 17.9372(15) Å, c = 11.9529(9) Å, α = β = γ = 90°, V = 1522.79(19) Å ³ , T = 100.00(10) K, Z = 4, μ(Mo Kα) = 3.787, 4592 reflections measured, 2099 unique (R _{int} = 0.0747) which were used in all calculations. The final wR2 was 0.1170 (all data) and R1 was 0.0469 (I > 2σ(I)).	10
Figure 2.2. Figure 2. Absorbance (A) and fluorescence (B) spectra of BSA (0.4 mg/ml), and BSA-2b conjugate (3), (0.4 mg/ml) in 10 mM bicarbonate buffer at pH 8.4 and 25°C.	13
Figure 2.3. Fluorescence of the 3 bioconjugate having undergone the CuAAC reaction with 3-azido-7-hydroxy-coumarin.	14
Figure 2.4. Proposed substrates for the incorporation of a second electrophilic center. A) Incorporation of an NHS ester. B) Incorporation of thioester.	16
Figure 2.5. Reactive thioesters for bioconjugation.	18
Figure 2.6. Labeling of Nanoparticles with an Ab using reagent 2f and 2g . TAB004 conjugation to PLGA NPs with FACS. Blank NPs were treated with: (A) control (red), TAB004 (blue), anti-mouse IgG ₁ FITC (green), and both TAB004 and anti-mouse IgG ₁ FITC (orange/yellow); (B) control (red), 2f linking reagent (blue), TAB004, and anti-mouse IgG ₁ FITC (green); (C) control (red), 2g linking reagent (blue), TAB004, and anti-mouse IgG ₁ FITC (green).	19
Figure 2.7. Possible outcomes upon reaction of 2g with 1 eq. of <i>n</i> -BuNH ₂ .	20
Figure 2.8. Reaction of 2c with <i>n</i> -BuNH ₂ .	22
Figure 2.9. Evolution of fluorescence at 470 nm upon formation of the BSA-2B/CuAAC Conjugate (4). Measured at λ _{ex} 404 nm, λ _{em} 470 nm.	23
Figure 3.1. Nanoparticle synthesis and design.	30
Figure 3.2. Nanoparticle functionalization with reagent 2g followed by incorporation of TAB004.	31

Figure 3.3. Pegylation reduces the amount of nonspecific binding of FL-mIgG1.	32
Figure 3.4. Compounds encapsulated in the NP platform. Paclitaxel (PTX), fluorescein diacetate (FL(OAC)2), Nile red (NR), indocyanine green (ICG).	33
Figure 3.5. SEM images of A. Paclitaxel (PTX) NPs, B. FL(OAC)2 NPs, C. NR NPs, D. ICG NPs. Scales as indicated.	34
Figure 3.6. FL(OAC)2 release profile from NPs in PBS pH 7.4. Results are mean \pm SD, $n = 3$.	35
Figure 3.7. Internalization of PLGA NPs in: (A) BxPC3 MUC1; (B) BxPC3 Neo. Results shown are representative images ($n=3$).	36
Figure 3.8. Cell viability of PDA cell lines treated with PTX and PTX loaded NPs: (A) BxPC3 Neo; (B) BxPC3 MUC1; (C) MIA PaCa-2; (D) HPAF-II; (E) HPAC. Data are shown as mean \pm SEM ($n=3$) and determined by a one-sided t-test comparing treatment groups at each concentration, * $p<0.05$, ** $p<0.01$, *** $p<0.001$, **** $p<0.0001$.	38
Figure 3.9. Specificity and internalization of TAB004 in BxPC3 MUC1 and Neo: (A) representative images of cells treated with TAB004 conjugated to pHRodo red ($n=3$); (B) quantification of images determined by the number of cells associated with TAB004 divided by total number of cells. Data are shown as mean \pm SEM ($n=3$) and determined by two-way ANOVA and Bonferroni's post-hoc test, * $p<0.05$, ** $p<0.01$, *** $p<0.001$, **** $p<0.0001$.	40
Figure 3.10. Confirmation of TAB004 conjugation to PLGA NPs with FACS. Blank NPs were treated with: (A) control (red), TAB004 (blue), anti-mouse IgG ₁ FITC (green), and both TAB004 and anti-mouse IgG ₁ FITC (orange/yellow); (B) control (red), reagent 2f (blue), and Thioester linking reagent, TAB004, and anti-mouse IgG ₁ FITC (green).	42
Figure 3.11. Internalization of T-NPs loaded with fluorescein diacetate (FL(OAC)2): (A) representative images of BxPC3 MUC 1 ($n=3$) treated with T-NPs; (B) representative images of BxPC3 Neo ($n=3$) treated with T-NPs; (C) and (D) quantification of fluorescence using Image J to determine corrected total cell fluorescence (CTCF). Data are shown as mean \pm SEM ($n=3$) and determined by a one-sided t-test, * $p<0.05$, ** $p<0.01$, *** $p<0.001$, **** $p<0.0001$.	43

Figure 3.12. Cell viability of PDA cell lines treated with PTX loaded NPs and PTX loaded T-NPs: (A) BxPC3 Neo; (B) BxPC3 MUC1; (C) MIA PaCa-2; (D) HPAF-II; (E) HPAC. Data are shown are mean \pm SEM (n=3) and determine by a one-sided t-test comparing treatment groups at each concentration, *p<0.05, **p<0.01, ***p<0.001, ****p<0.0001.	44
Figure 3.13. <i>In vivo</i> imaging of TAB004-ICG in orthotopically injected bioluminescent tumor bearing mice (ICG - red/yellow, tumor – rainbow, n=4): (A) mouse 1; (B) mouse 2; (C) mouse 3 and 4 ventral view; (D) mouse 3 and 4 side view.	46
Figure 3.14. <i>In vivo</i> imaging of ICG loaded NPs and ICG loaded T-NPs orthotopically injected bioluminescent tumor bearing mice (ICG - red/yellow, tumor – rainbow, n=3): (A) ICG loaded NPs injected into tumor bearing mouse; (B) ICG loaded T-NPs injected into tumor bearing mouse; (C) <i>ex vivo</i> imaging of liver and tumor from (A) and (B).	47
Figure. 3.15. Representative ^1H NMR (DMSO- <i>d</i> ₆ , 500 MHz) for determining PTX Loading.	50
Figure 4.1. Strategy of Cheng et. al. for the preparation of drug initiated PLA. A. Structures of paclitaxel (PTX) and camptothecin (CPT). B. Drug initiated polymerization of LA.	61
Fig. 4.2. Drug initiated polymerization of PCL.	62
Figure 4.3. Cholesterol initiated polymerization of PCL.	63
Figure 4.4. Synthetic route for the incorporation PTX through functionalization of the terminal OH of BzOH initiated PCL.	64
Figure 4.5. Paclitaxel (PTX). Numbering of PTX adapted from Beutler et. al.	65
Figure 4.6. Characterization of PCL PTX Conjugate. PCL-PTX conjugate (4e) red. Free PTX black.	66
Figure 4.7. Dosy spectrum of PCL-PTX conjugate (4e). A. PCL resonance at 4.0 ppm shown in red. B. Resonance of C2'-H of free PTX (blue) and of PCL-PTX (orange).	67
Figure 4.8. Nanoprecipitation of 4a or 4e resulting in high capacity NPs. Both PTX and cholesterol are expected to distribute evenly in both the NP core and surface.	68

Figure. 4.9. ^1H NMR (CDCl_3 , 500 MHz) 4a 0-5.6 ppm.	70
Figure. 4.10. ^1H NMR (CDCl_3 , 500 MHz) 4a 0.6-1.3 ppm.	71
Figure. 4.11. ^1H NMR (CDCl_3 , 500 MHz) 4b .	72
Figure. 4.12. ^1H NMR (CDCl_3 , 500 MHz) 4c .	73
Figure. 4.13. ^1H NMR (CD_3CN , 500 MHz) 4d .	74
Figure. 4.14. ^1H NMR (CD_3CN , 500 MHz) 4e .	75
Figure. 4.15. ^{13}C NMR (CD_3CN , 500 MHz) 4e .	75
Figure 5.1. Treatment of mastitis using MCMMM with (-) Nafcillin NPs.	84
Figure 5.2. Treatment of mastitis using MCMMM with (+) Nafcillin NPs.	85
Figure. 5.3. ^1H NMR (DMSO-d_6 , 500 MHz) used for determining nafcillin concentration in (-) nafcillin NPs.	89
Figure. 5.4. ^1H NMR (DMSO-d_6 , 500 MHz) used for determining nafcillin concentration in (+) nafcillin NPs.	90
Figure. 5.5. Experimental design for the MCMMM.	91

LIST OF TABLES

<i>Table</i>	<i>Page</i>
Table 2.1. Preparation of DMIA derivatives.	10
Table 2.2. Preparation of DMIA derivatives.	18
Table 2.3. Degree of labeling variables	24
Table 2.4. Data for BSA PDMIA bioconjugate for determination of DOL	24
Table 2.5. Data for BSA PDMIA bioconjugate after CUAAC reaction at 35 °C for determination of DOL	25
Table 3.1. Cargo Loading of PTX, FL(OAC) ₂ , NR, and ICG into Nanomaterials	33
Table 3.2. Structural Properties of PTX, FL(OAC) ₂ , NR, and ICG Nanomaterials.	34
Table 4.1. Characterization of high capacity nanomaterials	76
Table 5.1. Characterization of (-) Nafcillin NPs and (+) Nafcillin NPs	81
Table 5.2. Structural Properties of PTX, FL(OAC) ₂ , NR, and ICG Nanomaterials	82

LIST OF SCHEMES

<i>Scheme</i>	<i>Page</i>
Scheme 2.1. Preparation of DMIA from IA.	9
Scheme 2.2. Relative rates of reaction for 2b with D ₂ O and 10 eq of n-BuNH ₂ at RT.	12
Scheme 2.3. Labelling of BSA (0.53 mM) with 2b (1.8 mM) carried out in bicarbonate buffer for 1 hr. at RT; to give a degree of labelling (DOL) of 3.0 with an efficiency of 88%.	13
Scheme 2.4. CuAAC reaction of 3 (0.9 mg in 0.5 mL PBS buffer, 7.0 pH) and 3-azido-7-hydroxy-coumarin (2eq) at RT.	14
Scheme 2.5. The CuAAC reaction of 3 (0.9 mg in 0.5mL PBS buffer, pH 7.0) with 2c' (2eq) at RT.	15

LIST OF ABBREVIATIONS

Ab.....	Antibody
ACN.....	Acetonitrile
ADCs.....	Antibody Drug Conjugates
AMR.....	Antimicrobial Resistance
APT.....	Aptamers
BSA.....	Bovine Serum Albumin
BzOH.....	Benzyl Alcohol
CPT.....	Camptothecin
CDI.....	1,1'-Carbonyldiimidazole
CuAAC.....	Copper(I)-catalyzed Azide-Alkyne Cycloaddition
DCM.....	Dichloromethane
DLS.....	Dynamic Light Scattering
DMSO.....	Dimethyl Sulfoxide
DOL.....	Degree of Labeling
EDC.....	1-Ethyl-3-(3-dimethylaminopropyl)carbodiimide
EPR.....	Enhanced Permeability And Retention Effect
FACS.....	Fluorescence-Activated Cell Sorting
FDA.....	Food and Drug Administration
FL(OAC)2.....	Fluorescein Diacetate
ICG.....	Indocyanine Green
IMI.....	Intramammary Infections

MeI.....	Methyl Iodide
MCMMM.....	Modified Chronic Mouse Model Of Mastitis
NCL.....	Native Chemical Ligation
NHS.....	N-Hydroxysuccinimide
NP.....	Nanoparticle
NR.....	Nile Red
PCL.....	Polycaprolactone
PDA.....	Pancreatic Ductal Adenocarcinoma
PEG.....	Poly(ethylene glycol)
PhMe.....	Toluene
PLGA.....	Poly(lactic-co-glycolic acid)
PTX.....	Paclitaxel
RT.....	Room Temperature
SEM.....	Scanning Electron Microscope
SPAAC.....	Strain-Promoted Azide-Alkyne Cycloaddition
THF.....	Tetrahydrofuran
THPTA.....	Tris(3-hydroxypropyltriazolylmethyl)amine

CHAPTER 1: INTRODUCTION

1.1 Motivation

Since the discovery of the *nitrogen mustards* during world war II, the evolution of modern chemotherapeutic paradigms has resulted in significantly reduced cancer related mortality.^{1, 2} The five-year relative cancer survival rate has gradually increased by 38% from an estimated 25% in 1950¹ to approximately 63% from 2006-12.² Fundamental to this improvement has been; concerted efforts focused on disease prevention, early detection and diagnosis of disease, and the continued discovery of new chemotherapeutic compounds and therapeutic targets. Despite this, cancer remains the second leading cause of death in the United States with an estimated 1.7 million new cases expected in 2017 with approximately 600,000 people expected to succumb to the disease.³ Front-Line treatment regimens aimed at killing malignant neoplasms often suffer from several limitations. Therapeutic selectivity delineating healthy and diseased tissues, coupled with systemic toxicity are the principal limitations in today's standard treatment paradigms.⁴ Efforts to overcome these inadequacies has brought about multiple new avenues of research focusing on strategies of targeted therapeutics.⁵ The work in this thesis is motivated by the critical need to overcome these limitations in cancer chemotherapy. The burgeoning field of nanomedicine is poised to address these limitations through the construction of novel materials with attributes not achievable in materials otherwise constructed at the macro-scale.⁶

1.2 Nanotherapeutics a Historical Perspective.

With the evolution of molecular biology and biotechnology, the focus on the treatment of disease states has concomitantly evolved to expressly view treatment options at the cellular level. Today, treatment options are available which can manipulate key biological processes at nearly every level of transcriptional/translational control. Treatments such as this, whilst effective, are often hampered due to broad systemic delivery and off-target toxicity. Liposomes (first characterized in 1965) are some of the first nanotherapeutics approved by the U.S. Food and Drug Administration (FDA).^{7, 8} DOXIL®, a liposomal formulation of doxorubicin, was first approved in 1995 as a second-line treatment in patients found to be intolerant to other chemotherapy.⁸ To improve circulating half-lives strategies for the pegylation of the liposomal surface were developed. This simple strategy would generate formulations with “stealth” like properties capable of increased circulation times *in vivo*.⁹ Since the first introduction of DOXIL® this formulation has been approved for several indications (e.g. Kaposi sarcoma, ovarian cancer, and multiple myeloma),¹⁰ and several liposomal formulations of a diverse set of chemotherapeutics have entered the market. In 2005 Abraxane® was the first Albumin-bound nanoformulation of the blockbuster drug paclitaxel to receive FDA approval.¹¹ This formulation consists of human serum albumin (HSA) bound paclitaxel particles with a mean particle size of approximately 130 nm. These particles are a first in class formulation and exhibit improved solubility and target delivery when compared directly to paclitaxel. Since the introduction of DOXIL® and Abraxane® controlled drug delivery utilizing nanoformulations has been one of the most rapidly advancing areas of research in nanotechnology. To date there are approximately 51 FDA approved nanomedicines and 77 products in clinical trials

consisting of a wide variety of nanomaterials platforms.¹² These technological platforms include, but is not limited to; liposomes, protein carriers, PEGylated biomolecules and chemotherapeutics, nanocrystals, and polymer based nanomaterials.

1.3 Polymeric Nanoparticles

While the strictest definition of nanotechnology refers to structures where one dimension is in the 1-100 nm size regime, it widely accepted that term nanoparticles (NPs) refers to structures extending beyond this limitation.¹³ NP formulations constructed from polymers are perhaps one of the most amenable and effective nanocarriers available. The use of polymers to construct nanocarriers has several distinct advantages. Polymers used in the construction of such nanoformulations can be pooled from a wide variety of synthetic or natural sources.¹⁴⁻¹⁶ Such polymers can also be sourced from constitutively stable materials to bioresorbable materials offering exquisite control over nanomaterial stability and physiochemical parameters. Construction of nanomaterials from polymers also benefits from a wide variety of preparative techniques enabling control over parameters dictating NP size,¹⁷ morphology,¹⁸ and drug loading characteristics.¹⁹ Polymeric nanoparticles also provide a modular platform which can be readily manipulated to alter drug loading levels and surface chemistries.²⁰⁻²³ The dominant form of polymeric nanocarriers include the encapsulation of a drug within the hydrophobic core of the nanocarrier. Drug released from nanocarriers can be controlled by manipulating the polymeric matrix used in the construction of the nanocarrier. Generally, drug release is subject to first-order kinetics resulting from the diffusion of the encapsulated drug through the matrix of the NP into the cellular environment. Polymeric NPs can be rendered responsive to physiochemical stimuli through incorporation of self-immolating polymer

backbones or pH responsive moieties which can selectively trigger drug release under predetermined conditions.²⁴ The chemical surface of the nanomaterial offers an isolated environment for selectively adorning the particle with a wide variety of pendant functionality. Surface grafting of hydrophilic polymers can confer greater stability to the particle, provide improved circulation time, and aid in generating “stealth-like” particles capable of avoidance of the reticular endothelial system (RES).²⁵ Due to the direct interaction of the nanoparticle surface with the physiochemical environment pendant functionalities capable of altering the effective electric charge of the NP surface can confer substantial benefits for particle stability and cellular uptake.^{26, 27}

1.4 Polyesters.

Polyesters are one of the most studied biomedical materials with a wide variety of FDA approved application. Of all polyesters approved by the FDA for biomedical applications Poly(lactic-co-glycolic acid) (PLGA) has received considerable attention as a drug delivery material.²⁸ PLGA has many desirable characteristics. Byproducts of PLGA hydrolysis result in the liberation of metabolic monomers lactic and glycolic acids which can be readily cleared by the body.²⁸ Degradation time of the PLGA polymer can be controlled by varying the monomer ratios and stability can be provided from months to years.²⁹ PLGA is amenable to chemical modification and can be achieved synthetically in both pre-particle and post-particle formulations using a variety of synthetic techniques. Long circulating NPs composed of PLGA/Polyethylene Glycol (PEG) diblock polymers were first characterized in 1995 by Gref et. al.³⁰ Currently PLGA and compositions thereof are perhaps the most commonly employed polyester materials for the formulation of polymeric nanoparticles.

Polycaprolactone (PCL) is another polyester with FDA approval and is receiving renewed interest in biomedical applications. PCL was first used in the biomedical field during the development period of resorbable-polymers during the 1970s and 1980s. PCL is a hydrophobic, semicrystalline polymer which can be easily manipulated, and is biodegradable and biocompatible.³¹ PCL was, however, surpassed by the faster resorbing polylactides and polyglycolides in vogue at the time. With the advent of modern approaches to tissue engineering and nano engineering, the relatively low cost and mechanical compliance of PCL has seen renewed interest in PCL for these applications.³² Further, with this renewed interest there has been a concomitant rise in synthetic methodologies for generating PCL with exacting stringencies under facile conditions at the lab scale.³³

1.5 Passive Targeting of Nanoparticles

Nanocarriers are particles which can interact with biological environments in favorable ways not possible with small-molecule therapeutics.³⁴ Beyond merely providing a means of delivering a therapeutic cargo, nanoparticles have been shown to accumulate at tumor sites through the enhanced permeability and retention effect (EPR).³⁵ The EPR effect is mediated through the interaction of nanomaterials and structural abnormalities of tumor vasculature. Interendothelial defects result in larger than normal gap junctions which can facilitate the extravasation of materials on the nanoscale.³⁶ Transient accumulation of particles within the tumor site is further increased due to impaired lymphatic drainage.^{36,37} Upon accumulation at the tumor site nanomaterials can begin to release the chemotherapeutic cargo in the extravascular space. This process is advantageous to the increased local concentration of the therapeutic cargo whereby it can then undergo

diffusion or active transport into the cell. Further, upon accumulation, endocytosis of the nanomaterial at the tumor site can directly facilitate the delivery of the cargo directly into tumor cells.³⁸ Critical parameters affecting the passive targeting of nanomaterials include particles size and morphology, zeta potential, and density of hydrophilic materials on the NP surface. NPs up to 400 nm are typically amenable to accumulation at tumor sites through the EPR effect.³⁹ DeSimone's group have reported on the bio distribution and internalization pathways of polymeric nanoparticles of different size and shapes.⁴⁰ Data from these studies suggest a cellular preference for shape dependent uptake of rod shaped nanomaterials. This observation has been demonstrated by several other studies where aspect ratio can mediate cellular internalization.⁴¹

1.6 Active Targeting of Nanoparticles

Paul Ehrlich originally coined the concept of the “magic bullet” in the late 1800's. Ehrlich reasoned that chemicals could be tailored to selectively target disease-causing pathogens while concomitantly sparing host organisms. With the rise of biological targeting agents, the discrimination of different cellular antigens is readily achievable.⁴²⁻⁴⁴ Targeted nanomaterials were first introduced in 1980s in the form of antibodies (Ab) conjugated immunoliposomes.⁴⁵⁻⁴⁸ Modern development of targeted nanocarriers utilize a breadth of targeting agents and includes; Abs,⁴⁹⁻⁵¹ nucleic acid aptamers (APT),^{22, 23, 52} peptides or peptidomimetics,^{43, 53-55} and small molecules.⁵⁶ Mechanistically, active targeting of NPs occurs through a highly conserved interaction between the targeting moiety affixed to the NP surface, and cellular antigens known ideally to be expressed differentially in various tumors or tumor microenvironments. Binding of the targeting moiety with its membrane bound receptor can facilitate cellular uptake⁵⁷ or enhance NP

retention in the tumor microenvironment. Receptor-mediated targeting of cell-surface antigens is perhaps the most commonly exploited mechanism in targeted therapeutics. This mechanism is exploited in several strategies including antibody drug conjugates (ADCs),^{58, 59} immunotherapeutic applications,⁶⁰ and targeted nanomaterials.⁶¹ The virtue of targeting of NPs to the cell surface is the efficient cellular uptake of NPs through receptor-mediated endocytosis for the intracellular delivery of the therapeutic cargo. In one such application, Farokhzad et. al. utilized a modified A10 RNA aptamers specific for the extracellular domain of the prostate-specific membrane antigen (PSMA) to selectively target docetaxel (Dtxl) encapsulated Poly(D,L-lactic acid) NPs (APT-Dtxl-NPs) to LNCaP xenograft nude mice tumor models.²³ Results indicated improved Dtxl uptake, increased biocompatibility, and reduced tumor volume when compared to non-targeted Dtxl-NPs and free Dtxl. In a second related strategy targeting of cellular antigens present and overexpressed in the tumor microenvironment can result in increased residence times of nanomaterials which in-turn can result in increased local concentration of therapeutics upon release from the nanocarrier. Jiang et. al. utilized CLT1 peptide-conjugated PLA-PEG nanoparticles (CNP) to target fibronectins within the extracellular matrix of glioma microenvironments.⁶² *In vivo* and *ex vivo* analysis indicated an improved accumulation in the glioma site. Paclitaxel loaded CNP (CNP-PTX) was positively correlated with increased median survival times compared control treatments.

CHAPTER 2: Heterobifunctional Reagents for Bioconjugation

Forward

This chapter recognizes the contributions of: *Adam Fessler,¹ Corey Garmon,¹ Thomas Heavey,¹ Anthony Fowler,¹ and Craig Ogle.¹* Water-soluble and UV traceable isatoic anhydride-based reagents for bioconjugation. *Org Biomol Chem*, **2017**. Results have been reproduced here with permission. Anthony J. Fowler wrote and prepared the manuscript, and along with Craig A. Ogle prepared experimental design. Craig A. Ogle and Anthony J. Fowler are assignees to the patent (PCT/US15/11751 - patent approved) published on this work.

2.1 Introduction

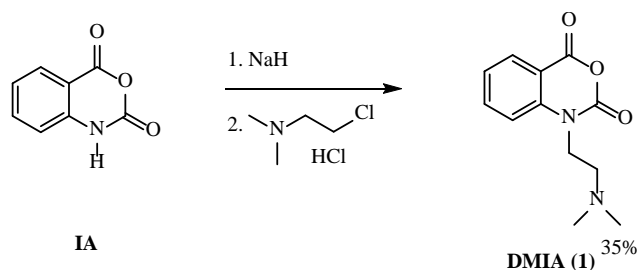
The nucleophilic lysine residue is one of the most commonly exploited targets in bioconjugation.^{63, 64} Lysine modification is classically achieved through nucleophilic acyl-substitution upon reaction with amine reactive succinimidyl (NHS) or sulfo-NHS esters. This bioconjugation strategy results in amide bond formation between the biomolecule and chemical functionality being installed. Similar modification strategies involving isocyanates and isothiocyanates are also employed in lysine modification resulting in urea and thiourea linkages in the final bioconjugate respectively. Although capable of installing a wide variety of chemical functionality, the resulting bioconjugates often require exogenous secondary assays for the quantification of the installed chemical functionality.

¹ Department of Chemistry, University of North Carolina at Charlotte. 9201 University City Blvd, Charlotte, NC 28223.

To circumvent this issue, modifying reagents with an intrinsic chromophore capable highly sensitive detection are desired. We sought to develop an acylating reagent with an intrinsic chromophore, which could support the incorporation of a wide variety of chemical functionality. Moreover, we sought a reagent set that could be accessed readily and in high yield from inexpensive, and commercially available materials, avoid the need for NHS chemistry, and remain functional under physiological conditions. We envisaged N-(N', N'-dimethylaminoethylene)-isatoic anhydride (DMIA) could fulfil all these criteria. Derivatives of isatoic anhydride (IA) have been previously reported for the modification of biomolecules.^{65, 66} Particularly, N-methyl Isatoic anhydride (NMIA) and its derivatives has been utilized as a selective acylating agent of 2'OH of RNA and is a principle component of SHAPE analysis.⁶⁷⁻⁶⁹ Despite this, derivatives of IA have found minimal application in the modification of either proteins, or peptides, likely due to poor chemical diversity and water solubility of IA derivatives.

2.2 Results and Discussion

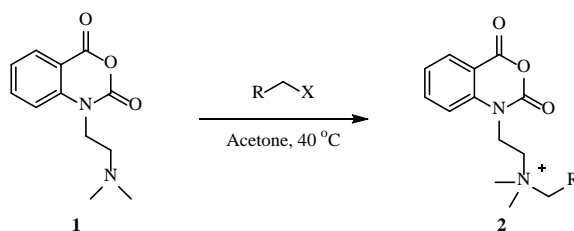
We accessed **1** and its derivatives (**2a-e**) in a simple two-step synthetic sequence below. Firstly, **1** can be accessed in a single step from IA in moderate yields (scheme 1).



Scheme 2.1. Preparation of DMIA from IA.

Upon isolation of DMIA, derivatives are accessible in a second high-yielding, high-purity step (Table 1). Alkylation of the N,N-dimethyl moiety of **1** in anhydrous acetone or THF result in the precipitation of the resultant quaternary ammonium salts. Using this method, we have isolated x-ray quality crystals of **2b** (Fig. 1).

Table 2.1. Preparation of DMIA derivatives



Entry	RCH ₂ X	ϵ (M ⁻¹ cm ⁻¹)	Yield (% , isolated)
1	CH ₃ I	3745	69 (2a)
2	HC≡CCH ₂ Br	3750	89 (2b)
3	N ₃ (CH ₂) ₃ I	3611	64 (2c)
4	H ₂ C=CHCH ₂ Br	3882	84 (2d)
5	p-H ₂ C=CH(C ₆ H ₄)CH ₂ Br	3850	53 (2e)

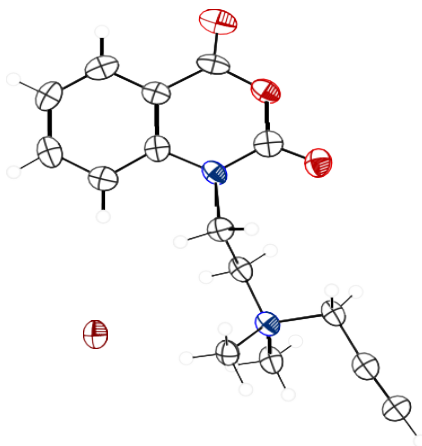
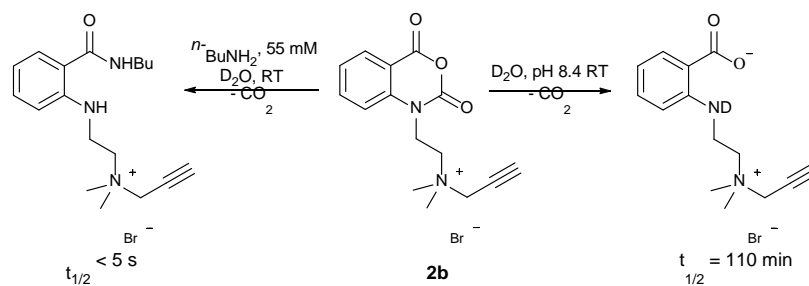


Figure 2.1. ORTEP of **2b** Crystal Data. C₁₅H₁₇N₂O₃Br, M = 353.21, orthorhombic, P na21 (No. 33, a = 7.1025(4) Å, b = 17.9372(15) Å, c = 11.9529(9) Å, $\alpha = \beta = \gamma = 90^\circ$, V = 1522.79(19) Å³, T = 100.00(10) K, Z = 4, μ (Mo K α) = 3.787, 4592 reflections measured, 2099 unique (Rint = 0.0747) which were used in all calculations. The final wR2 was 0.1170 (all data) and R1 was 0.0469 (I > 2 σ (I)).

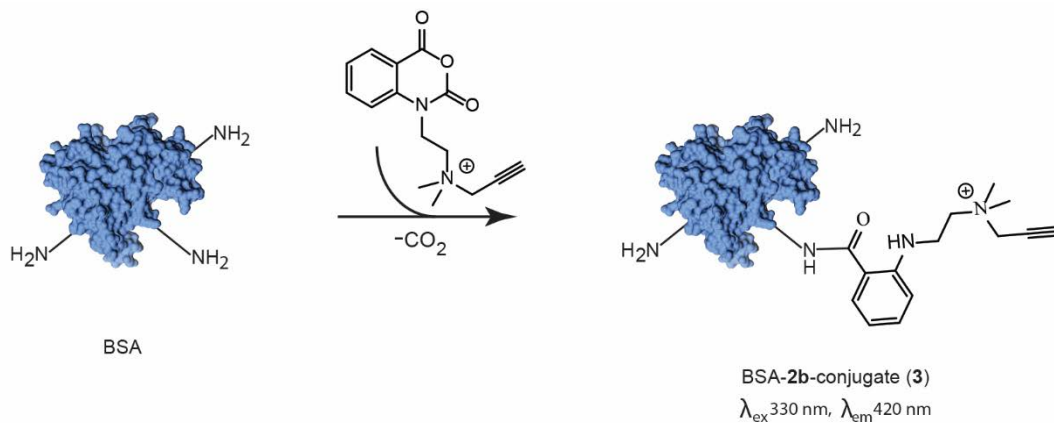
We chose **2b** to serve as our model for this new bioconjugation platform due to its obvious application to the widely used copper-catalyzed azide-alkyne cycloaddition (CuAAC).^{70,71} **2b** and other derivatives of **1** share several desirable properties making these compounds ideal for applications under physiological conditions. Firstly, the quaternary ammonium salt conveniently renders derivatives of **1** water-soluble minimizing the need for water-miscible organic solvents such as DMF or DMSO that is typical of reactions involving NHS esters. The solubility of **2b** is similar to sulfo-NHS esters and working concentrations of **2b** at > 20 mg/ml in DI water are readily achieved. Secondly, the anhydride moiety of **2b** reacts rapidly with primary amines under aqueous conditions and results in the liberation of innocuous CO₂ as the only leaving group in the reaction (scheme 2). We characterized the hydrolytic stability of **2b** using ¹H NMR (Supplementary Fig. S1). **2b** exhibits a high degree of hydrolytic stability having a half-life of over 16 hrs at pH 7.0, and ≈ 2 hrs. at pH 8.4 in 25 mM bicarbonate buffer. In comparison, we used rapid injection NMR (RI-NMR) to characterize the reaction of **2b** with 10 equivalents *n*-butyl amine in D₂O. We chose *n*-butyl amine as a model for lysine due to its high water solubility, isostructural comparison to the lysine side chain, and similar pK_a of the *n*-butyl amine and lysines ε-NH₂ (10.59⁷² and 10.53⁷³ respectively). Indeed, the RI-NMR experiment showed that the **2b** was completely consumed in the first 5 seconds by the excess *n*-butyl amine.



Scheme 2.2. Relative rates of reaction for **2b** with D_2O and 10 eq of $n\text{-BuNH}_2$ at RT.

Derivatives of **1** have an intrinsic 7-atom spacer that is extended by virtue of the installed functionality. This built-in chemical spacer can remediate the need for additional spacers, yet derivatives bearing increased spacer-distance can be tailored according to need. Finally, derivatives of **1** all exhibit a characteristic excitation and emission wavelength of 330 and 420 nm respectively on labelled biomolecules (Fig. 2), similar to values reported for NMIA.⁷⁴ Because the principle absorbance of the derivatives of **1** is outside the range of typical biomolecules, quantification is simple and can be carried out with a series of simple single-point scans.

2b readily undergoes amide bond formation with bio-molecules. To test the ability for **2b** to serve as a scaffold for installing functionality on a bio-molecule we chose bovine serum albumin (BSA) as a model protein (scheme 3). BSA is inexpensive, readily available, and has multiple lysine's available for reactivity. While much focus has been on the site selective functionalization of proteins, derivation through amide bond formation using lysine residues remains one of the most common avenues for installation of chemical functionality onto proteins.



Scheme 2.3. Labelling of BSA (0.53 mM) with **2b** (1.8 mM) carried out in bicarbonate buffer for 1 hr. at RT; to give a degree of labelling (DOL) of 3.0 with an efficiency of 88%.

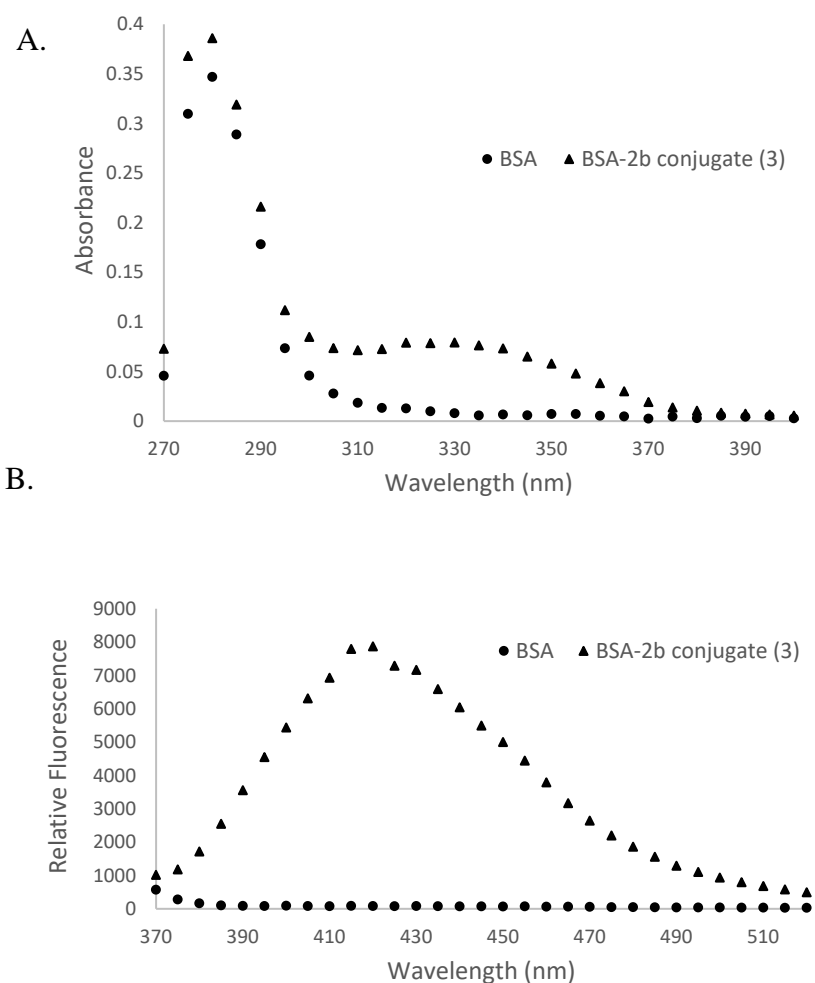
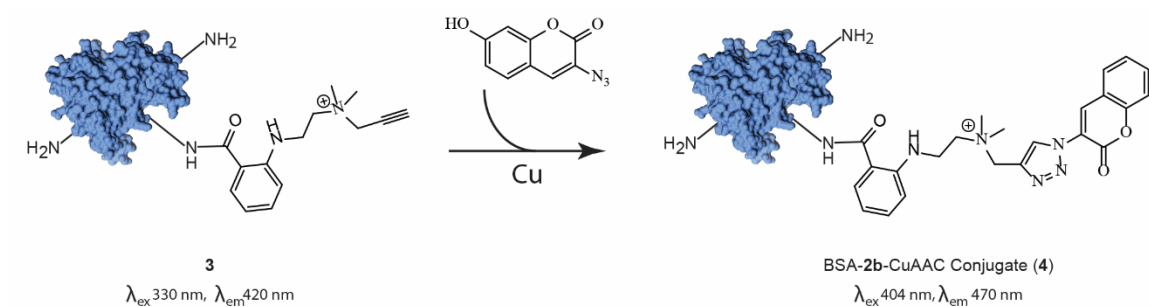


Figure 2.2. Figure 2. Absorbance (A) and fluorescence (B) spectra of BSA (0.4 mg/ml), and BSA-2b conjugate (3), (0.4 mg/ml) in 10 mM bicarbonate buffer at pH 8.4 and 25 °C.

We further characterized **3** to undergo CuAAC utilizing the strategy of Finn et. al. (scheme 4).⁷⁵ Briefly, the purified **3** bioconjugate with a DOL of 3.0 was reacted with 3-azido-7-hydroxy-coumarin resulting in the formation of the described fluorescent triazole product as evidenced by the evolution of the indicative fluorescence at 470 nm (Fig. 3).⁷⁶



Scheme 2.4. CuAAC reaction of **3** (0.9 mg in 0.5 mL PBS buffer, 7.0 pH) and 3-azido-7-hydroxy-coumarin (2eq) at RT.

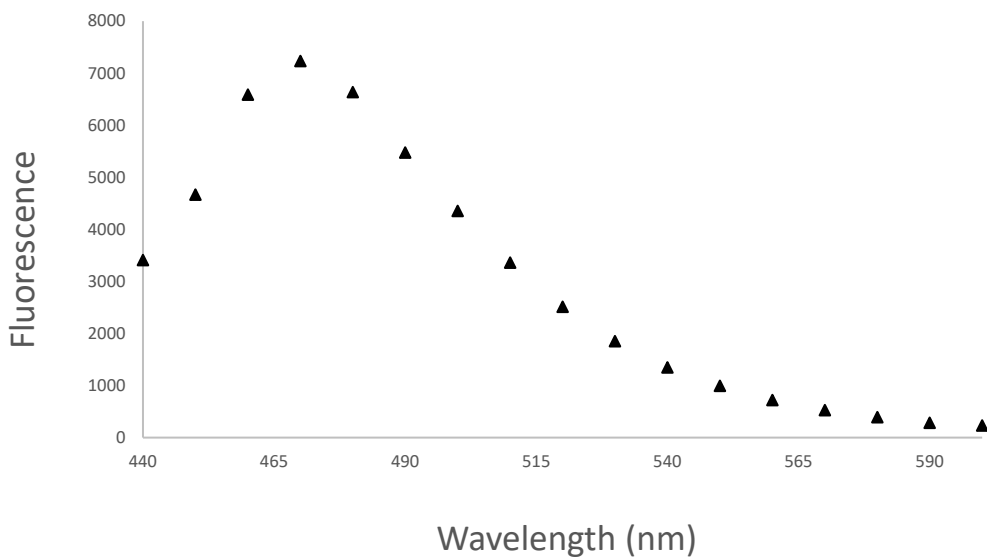
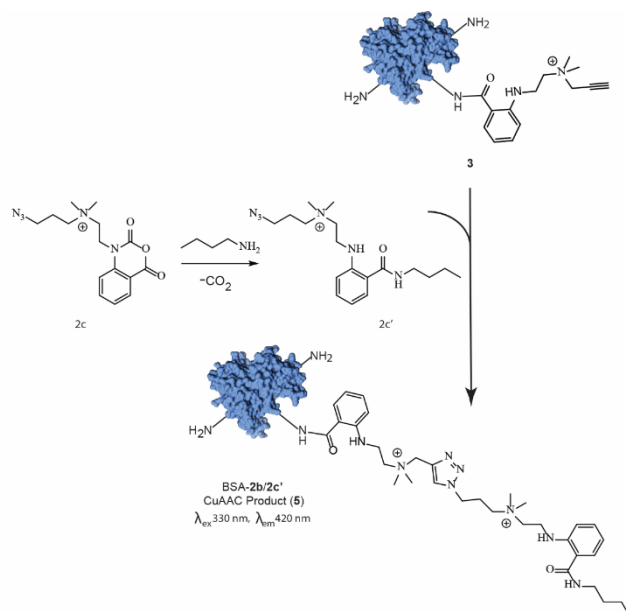


Figure 2.3. Fluorescence of the BSA-2b conjugate (**3**) having undergone the CuAAC reaction with 3-azido-7-hydroxy-coumarin to yield (**4**).

Having shown that **3**, the BSA-**2b** bioconjugate, can successfully undergo the CuAAC protocol, we sought to demonstrate the isatoic anhydride platform described herein could facilitate the conjugation of an exogenous cargo molecule onto a biomolecular platform. Using the isatoic anhydride platform, incorporation of a cargo is readily detected using a series of single-point-scans to track the evolution of the chromophore, which is ideally expected to double upon completion of the reaction. We tested the simplest case wherein **3** with a DOL of 3.0 was reacted with **2c'** formed from the reaction of **2c** with *n*-BuNH₂ (scheme 5). The CuAAC reaction was carried out at 25 °C for 24 hrs. Over the 24 hr period the reaction to form **5** proceeds to approximately 92 % as suggested by the increase in absorbance at 330 nm. Whilst these results clearly indicate the ability for the isatoic anhydride platform to readily incorporate a simple cargo molecule such as *n*-BuNH₂ onto a biomolecular platform, the application of such mild conditions readily demonstrates this platform can be adapted to the incorporation of a variety of cargoes ranging from fluorophores to chemotherapeutics alike.



Scheme 2.5. The CuAAC reaction of **3** (0.9 mg in 0.5mL PBS buffer, pH 7.0) with **2c'** (2eq) at RT.

These results indicate that bioconjugate **3** can readily furnish the installation of a chemically diverse series of cargoes limited by only the need for the presence of a cognate azide capable of undergoing the aforementioned CuAAC chemistry.

To extend the scope of this platform, we sought to develop a reagent which could undergo two sequential electrophilic reactions. Unlike **1** which possesses both an electrophilic and a nucleophilic center, we reasoned that a reagent bearing two kinetically differentiated reaction centers could be utilized to readily functionalize a nucleophilic surface with a biomolecule without the need for altering the native functionality of that biomolecule. To introduce the second electrophilic center into the platform, we reasoned the installation of a reactive ester would facilitate this goal. To achieve this, we surmised that substrates of the following composition would achieve the desired results.

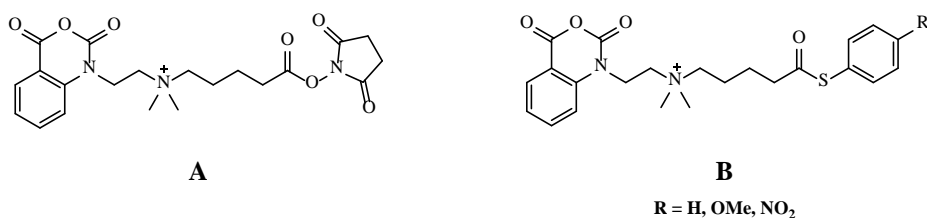
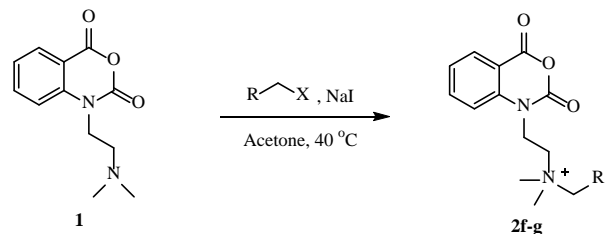
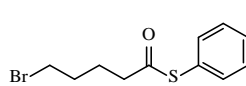
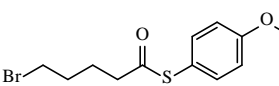


Figure 2.4. Proposed substrates for the incorporation of a second electrophilic center. A) Incorporation of an NHS ester. B) Incorporation of thioester.

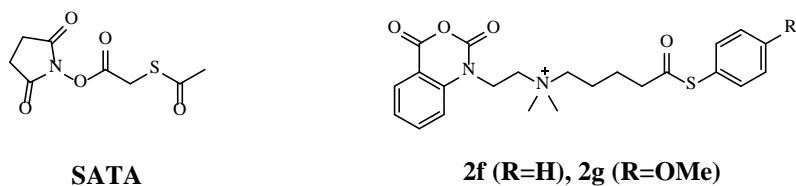
NHS esters have a half-life of approximately 10 min at pH 8.6 and 4 °C, and readily reacts with amines from pH 7.2-9.0 to yield stable amide bonds.⁷⁷ Accordingly, due to the similarity in reactivity of NHS esters compared to the anhydride reactivity of **2b**, it was expected that reagent **A** could not be chemically

differentiated. Conversely, thioesters have improved hydrolytic stabilities. Alkyl thioesters have been shown to have hydrolysis half-lives of 155 days at pH 7.0 with aryl-thioesters having half-lives of 15 days under similar conditions.⁷⁸ Further in a study of electron deficient aryl thioesters with nitrogen based nucleophiles, Kalia et. al. have demonstrated these thioesters exhibit relatively slow reaction with amines at pH 7.0.⁷⁹ Due to the ability to modify the electronic characteristics of aryl-thioesters, and the improved hydrolytic stability of such substrates we chose to pursue thioesters as a means of developing a kinetically controlled asymmetric bis-electrophiles. We developed reagents **2f** and **2g** using our strategy established with minor modification (table 2). As can be seen from table 1 the alkylation of **1** is optimally achieved through use of either activated bromides or primary iodides. To access our proposed reagents, we used commercially available 5-bromovaleric acid to generate the desired thioester. To incorporate the thioester onto **1** we utilized a simple Finkelstein reaction to generate a primary iodide which could therefore alkylate **1** under the established conditions.

Table 2.2. Preparation of DMIA derivatives.

Entry	RCH ₂ X	ϵ (M ⁻¹ cm ⁻¹)	Yield (%; isolated)
1		~ 3700	62 (2f)
2		~ 3700	35 (2g)

Thioesters have been extensively studied in the literature. Thioesters exist as important biosynthetic intermediates in a variety of biochemical pathways.⁸⁰ Further thioesters are important synthetic reagents and have been employed as bis-electrophiles for this incorporation of thiols. Particularly, *N*-Succinimidyl-*S*-acetylthioacetate (SATA) (fig. 5) is used for the incorporation of thiol onto a biomolecule platform. Unlike SATA, reagents **2f** and **2g** reverse this chemistry allowing for the formation of a second electrophilic center.

**Figure 2.5.** Reactive thioesters for bioconjugation.

We characterized the ability for **2f** and **2g** to incorporate an antibody (Ab) onto the nucleophilic surface of polyester nanoparticles. Nanoparticles composed of PLGA with an aminated surface were first functionalized with either **2f** or **2g** under neutral conditions to reduce hydrolysis and decrease particle aggregation. In a second step the functional nanomaterials were treated with a MUC1 specific Ab TAB004. The incorporation of the Ab was then detected using a fluorescein labeled secondary Ab and fluorescence-activated cell sorting (FACS) analysis. Under these conditions reagent **2f** was successful in the incorporation of TAB004 whereas **2g** failed to incorporate TAB004 which we reason is likely due to its decreased reactivity due to the electron-rich nature of the aryl thiol.

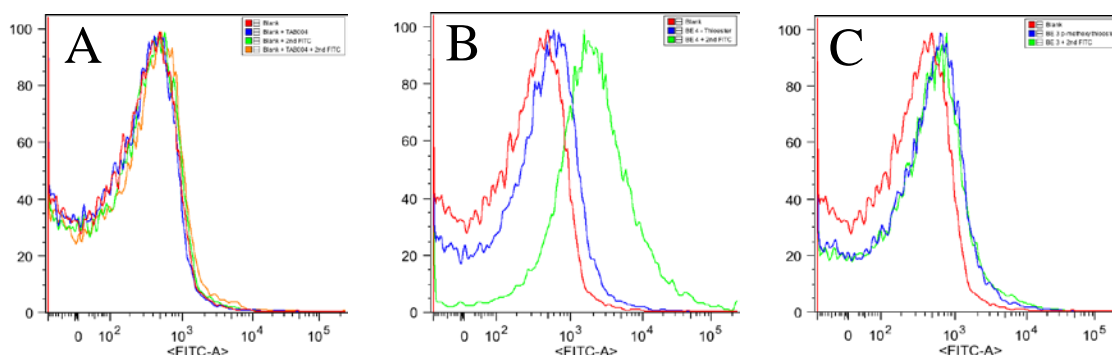


Figure 2.6. Labeling of Nanoparticles with an Ab using reagent **2f** and **2g**. TAB004 conjugation to PLGA NPs with FACS. Blank NPs were treated with: (A) control (red), TAB004 (blue), anti-mouse IgG₁ FITC (green), and both TAB004 and anti-mouse IgG₁ FITC (orange/yellow); (B) control (red), **2f** linking reagent (blue), TAB004, and anti-mouse IgG₁ FITC (green); (C) control (red), **2g** linking reagent (blue), TAB004, and anti-mouse IgG₁ FITC (green).

To assess the reactivity of **2g**, we tested the ability for **2g** to undergo asymmetric amination with 1 equivalent of *n*-BuNH₂ at 25 °C and pH 8.4 (Fig. 2.7). Results were analyzed by LC/MS. Under these conditions reagent **2f** was selective for amination at the anhydride yielding only product A (Fig. 2.7) with no detectable product formation through

reaction with the thioester to yield **B** (Fig. 2.7). This result supports those obtained from our previous study demonstrating Ab incorporation onto NP surfaces.

Because **2f** was capable of incorporating TAB004 on the NP surface we chose to pursue this reagent for modifying NP surfaces (see chapter 3). Although **2g** has superior hydrolytic stability and attenuated reactivity with amines compared to **2f**, its inability to react with primary amines render it unusable for our proposed application. However, thioesters have been shown to undergo rapid thioester exchange with phenyl thioesters undergoing thiol-thioester exchange with half-lives of 34 min.⁷⁸ Therefore, **2g** could find chemoselective applications where thioester exchange is the predominate mechanism such as native chemical ligation (NCL).^{81, 82} Further, previous studies have demonstrated thio-inteins undergo rapid reaction with α -hetero nucleophiles and **2g** will likely serve as a suitable substrate for reagents with increased nucleophilicity compared to *n*-BuNH₂.⁷⁹ Future studies optimizing these asymmetric bis-electrophiles are underway.

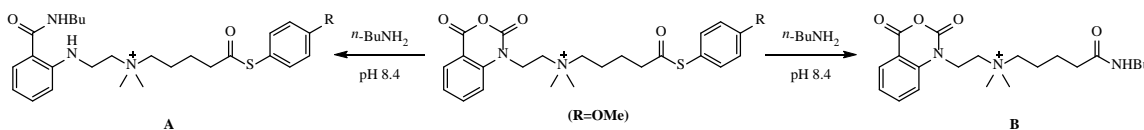


Figure 2.7. Possible outcomes upon reaction of **2g** with 1 eq. of *n*-BuNH₂.

2.3 Conclusion

Herein we have exploited isatoic anhydride for the construction of a highly versatile bioconjugation platform which has the benefits of being water-soluble, UV traceable, fluorescent, and reactive to nucleophilic amines under relatively mild conditions. We have used the described strategy to generate protein-bioconjugates using BSA as a model

protein. The installation of the alkyne did not interfere with the solubility of the BSA, and we have shown that the installed alkyne was available for the installation of a cargo molecule through the use CuAAC chemistry. We anticipate reagents such as **2b** will find broad application due its ability to undergo orthogonal reactivity with a host of commercially available reagent, or be coupled with derivatives of **2c** allowing for a purely customized coupling procedure. Additionally, we have demonstrated the installation of a second electrophilic center onto the platform in reagents **2f** and **2g** for the installation of a second functionality through two sequential nucleophilic acyl substitutions. Further, we have shown that these reactions can be used to furnish chemoselective reactivities by controlling the electronic nature of the reagents.

Finally, we note that this new platform can be easily adapted to any suitably reactive substrate to furnish a plethora of new reagents. Continued development of this platform is underway.

2.4 Materials and Methods

All chemical reagents use for the study were of analytical grade and above. Unless otherwise mentioned all reagents were purchased from Sigma Aldrich (St. Louis, MO). ¹H and ¹³C NMR was obtained on a JEOL ECX-500 MHz spectrophotometer and referenced to the solvent.

Reagent Synthesis. Reagents 1, and 2a-g were previously reported in the thesis of Corey B. Garmon at the University of North Carolina at Charlotte.

Labeling of BSA by with **2b (**3**).** A stock solution of BSA (40 mg/ mL) (0.60 mM) was prepared in 25 mM bicarbonate buffer (pH 8.40). 300 μ L of the solution was transferred to an Eppendorf tube. To this was added 40 μ L of **2b** (15mM) and reacted for 1 h, RT. To this was added 5 μ L NH_4OH . 3 Princeton Separations CS-800 Pro Spin GPC columns were used to purify 300 μ L of the solution. 20 μ L of purified solution was diluted with 480 μ L 25 mM bicarbonate buffer (pH 8.40). This solution was placed in a 500 μ L quartz cuvette on a Molecular Devices Spectramax M5 plate reader and absorbance was read (250-450 nm). The DOL was determined to be 3.0.

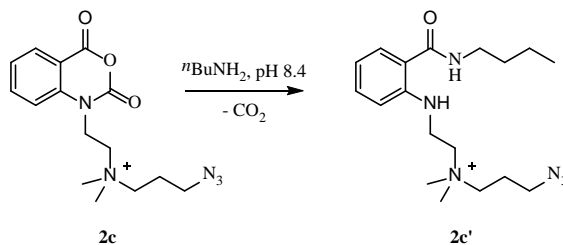


Figure 2.8. Reaction of **2c** with *n*-BuNH₂.

Ring opening of **2c (**2c'**).** **2c** was transferred to a 1.5 mL Eppendorf tube (5.0 mg, 0.01 mmol), to this was added butylamine (20 μ L, 0.2 mmol) and vortexed until all salts were dissolved into solution. The solution was then diluted to 15 mM with DI H₂O and excess butylamine is removed under reduced vacuum. The solution is then used directly without further purification. *m/z* (ESI): Calc. 347.26; Found (M⁺) 347.23.

CuAAC reaction between bioconjugate **3 and 3-azido-7-hydroxy-coumarin (**4**).** The procedure of Hong et. al. was used without modification. Briefly, the bioconjugate **3** (25

μL , 34 mg/ml) with a DOL of 3.0 was diluted in 407.5 μL of 100 mM PBS buffer (pH 7.0) in a 1.5 ml Eppendorf tube. To this was added 10 μL of the 3-azido-7-hydroxy-coumarin (20 mM). THPTA ligand (50 mM, 5 μL) was premixed with CuSO_4 (20 mM, 2.5 μL) and added to the solution. Aminoguanidine hydrochloride (100 mM, 25 μL) was added to the solution followed by freshly made sodium ascorbate (100 mM, 25 μL). The solution was vortexed and 150 μL transferred to an opaque walled 96 well plate. The reaction was monitored for evolution of fluorescence at 470 nm using the excitation wavelength of 404 nm.

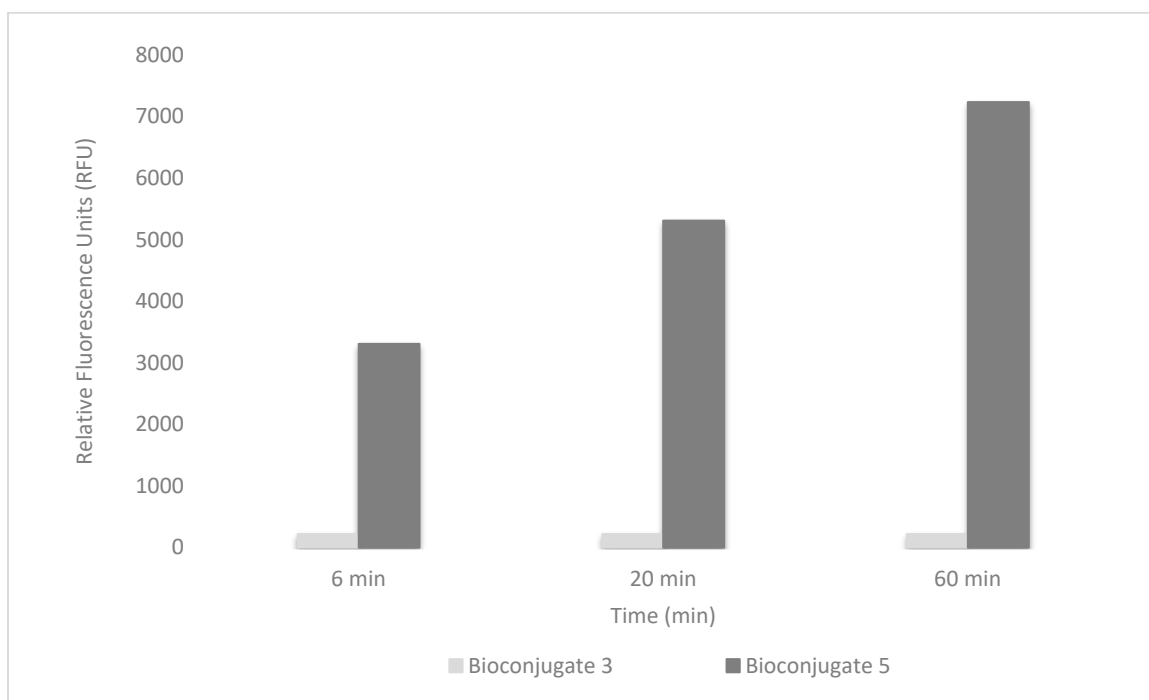


Figure 2.9. Evolution of fluorescence at 470 nm upon formation of the BSA-2B/CuAAC Conjugate (4). Measured at λ_{ex} 404 nm, λ_{em} 470 nm.

CuAAC reaction between bioconjugate 3 and 2c'. The procedure of Hong et. al. was used with minor modification. Briefly, the bioconjugate 3 (25 μL , 34 mg/ml) with a DOL of 3.0 was diluted in 385.5 μL of 100 mM PBS buffer (pH 7.0). To this was added 32 μL

of the Azide **2c'** (6.25 mM). THPTA ligand (50 mM, 5 μ L) was premixed with CuSO₄ (20 mM, 2.5 μ L) and added to the solution. Aminoguanidine hydrochloride (100 mM, 25 μ L) was added to the solution followed by freshly made sodium ascorbate (100 mM, 25 μ L). The solution was vortexed and incubated at 25 °C for 24 hrs. The reaction was stopped by passing 100 μ L of the reaction mixture through a Princeton Separations CS-800 Pro Spin GPC column. 20 μ L of purified solution was diluted with 480 μ L 25 mM bicarbonate buffer (pH 8.40). This solution was placed in a 500 μ L quartz cuvette on a Molecular Devices Spectramax M5 plate reader and absorbance was read (250-450 nm).

Degree of labeling (DOL) was determined using equation 1 below.²

$$DOL = \frac{A_{330}\epsilon_{prot}}{(A_{280} - A_{330}C_{280})\epsilon_{reagent}}$$

Equation 1. Degree of labeling calculation

Table 2.3. Degree of labeling variables	
Abbreviation	Definition
A ₃₃₀	Absorbance of the sample at 330 nm
ϵ_{prot}	Molar extinction coefficient (in M ⁻¹ cm ⁻¹) of pure protein at 280 nm
A ₂₈₀	Absorbance of the sample at 280 nm
C ₂₈₀	Correction factor of reagent at 280 nm
$\epsilon_{reagent}$	Molar extinction coefficient (in M ⁻¹ cm ⁻¹) of the reagent at 330 nm

Table 2.4. Data for BSA PDMIA bioconjugate for determination of DOL	
Abbreviation	Value
A ₃₃₀	0.1707
ϵ_{prot}	43,824 M ⁻¹ cm ⁻¹
A ₂₈₀	0.7215
C ₂₈₀	0.3184
$\epsilon_{reagent}$	3750 M ⁻¹ cm ⁻¹

² Abberior Degree of Labeling (DOL) <http://www.abberior.com/support/protocols/degree-of-labeling-doi/> (accessed July 25, 2016).

Table 2.5. Data for BSA PDMIA bioconjugate after CUAAC reaction at 35 °C for determination of DOL

Abbreviation	Definition
A ₃₃₀	0.5086
ε _{prot}	43,824 M ⁻¹ cm ⁻¹
A ₂₈₀	0.2069
C ₂₈₀	0.3037
ε _{reagent}	3680 M ⁻¹ cm ⁻¹

Conjugation of TAB004 to PLGA NPs. TAB004 conjugation to PLGA nanoparticles was performed using reagents **2f** and **2g**. PLGA nanoparticles were weighed out into an appropriate Eppendorf tube. To a vial containing 1 mg of either **2f** or **2g** was added 1 drop of DMSO to assist with dissolution, then 500µl of 18Ω H₂O was added. The solution was vortexed until all of the labeling reagent was dissolved. The PLGA nanoparticles were re-suspended in 200µl of 18Ω H₂O. The labeling solution was added dropwise to the nanoparticles while under a gentle vortex and allowed to incubate at room temperature 15 min after mixing. The labeled nanoparticles were centrifuged at 21,000 rcf and 4 °C to pellet them. The supernatant was removed, and the labeled nanoparticles re-suspended in 200µl of 18Ω H₂O. 30µg of TAB004 at mg/ml conc (in azide free buffer) was then added to the labeled NP solution in one portion. The next day, the nanoparticles were centrifuged at 21,000 rcf and 4 °C to pellet them and the supernatant discarded. Nanoparticles were re-suspended into desired working volume of PBS. Successful TAB004 conjugation to the PLGA nanoparticle was confirmed using FACS (BD Fortessa) and an anti-mouse IgG₁-FITC secondary antibody.

Reaction of 2g with *n*-BuNH₂. To an Eppendorf was added 1 mg of **2g** and the reagent dissolved into 1 ml of 25 mM bicarbonate buffer at pH 8.4 (1 mg/ml). To this solution was added To confirm complete conversion to product the reaction was analyzed by HPLC on a Thermo Scientific Vanquish system with a RS diode array detector (330 nm) on a reverse-phase column (Thermo Scientific Accucore C18, 150 x 2.1 mm, 2.6 μm) and Thermo Scientific Velos Pro mass spectrometer.

Chapter 3: Treatment of Pancreatic Ductal Adenocarcinoma with Tumor Antigen Specific-Targeted Delivery of Paclitaxel Loaded PLGA Nanoparticles.

Forward

This chapter recognizes the contributions of: *Shuta Wu*,³ *Anthony J. Fowler*,⁴ *Corey B. Garmon*,³ *Adam B. Fessler*,³ *Joshua D. Ogle*,³ *Kajal R. Grover*,² *Bailey C. Allen*,² *Chandra D. Williams*,⁵ *Ru Zhou*,³ *Laura J. Moore*,³ *Mahboubeh Yazdanifar*,³ *Craig A. Ogle*,⁴ and *Pinku Mukherjee*.³ (*Manuscript Submitted*). Biological methods and results have been reproduced here with permission.

3.1 Introduction

Pancreatic cancer has one of the poorest clinical prognosis. The five-year survival rate for pancreatic cancer is approximately 8% with most patients being diagnosed with advanced disease.² Of newly diagnosed cases if surgical resection is possible the median survival rate is 27%, and if the patient presents with metastatic disease the expected five-year survival rate drops to 2%⁸³ - a value reminiscent of the five-year survival rate of the 1970's.² Surgical resection followed by systemic chemotherapy remains the first-line treatment option in most cases for qualifying patients. Pancreatic cancers poor clinical prognosis is due to several interconnected factors. Originally thought to possess minimal clinical impact, the tumor microenvironment of pancreatic cancer is now believed to play an intricate role in the chemoresistance of pancreatic cancers.⁸⁴ This dense stromal tissue

³ Department of Biological Sciences, University of North Carolina at Charlotte, Charlotte, North Carolina 28223, United States.

⁴ Department of Chemistry, University of North Carolina at Charlotte, Charlotte, North Carolina 28223, United States.

⁵ Department of Animal Laboratory Resources, University of North Carolina at Charlotte, Charlotte North Carolina 28223, United States.

is not only expected to provide a steric barrier to chemotherapeutic accumulation, but harbor a variety of cell types and extracellular components responsible for tumor cell invasion, metastasis, and proliferation.^{84, 85}

Gemcitabine (GEM) has been the leading monotherapy for pancreatic cancer treatment since its approval in 1997.⁸⁶ Only recently has combination therapies such as FOLFIRINOX (FOLinic acid, Fluorouracil, IRINotecan and OXaplatin) and nab-paclitaxel (nab-P) plus GEM, shown improved efficacies over the GEM monotherapy. Phase III clinical survival rates of FOLFIRINOX treatment groups exhibited a mean survival increase of 11.1 months compared to 6.8 months for Gem monotherapy.⁸⁷ Similar results were obtained for the nab-P + GEM treatments, with median survival rates increasing to 8.5 months compared to the 6.7 months obtained for GEM monotherapy.⁸⁸ Although each of these regimens confer statistically relevant benefits there remains a critical need for considerable improvements to therapeutic outcomes.

Targeted nanocarriers are attractive materials for the treatment and diagnosis of pancreatic cancer. Targeted polyester NPs adorned with RNA aptamers have been shown to increase cellular uptake and tumor residence times resulting in improved pharmacokinetics and therapeutic outcomes of Docetaxel (Dtx) encapsulated materials.²² Pancreatic cancer-associated tumor antigens are numerous⁸⁹ and several of these have been prioritized as highly selective antigens for tumor targeting.⁹⁰ Mucin-1 (MUC1) is one such antigen. MUC1 is a transmembrane protein consisting of intracellular and extracellular domains. The extracellular domain of MUC1 (MUC1-N) is a glycoprotein densely functionalized through O-linked glycosylation under normal physiological conditions.

During oncogenic transformation MUC1-N becomes hypoglycosylated exposing its protein core rendering it “visible” for targeting.⁹¹

Herein we reasoned that polyester based nanomaterials could serve to function as suitable nanocarriers for both paclitaxel (PTX) and Indocyanine Green (ICG) for the treatment and diagnosis of pancreatic tumors. Further when combined with a suitable targeting agent for MUC1 these nanocarriers could be rendered an active targeting platform.

3.2 Results and Discussion

Nanoparticle Preparation and Characterization. We chose to utilize the nanoprecipitation method to encapsulate the selected cargoes inside the hydrophobic cores of PLGA NPs. Nanoprecipitation has several tangible benefits, including; simple setup and ease of preparation, control over NP size and NP polydispersity (PDI), ability to encapsulate both hydrophobic and hydrophilic molecules, and simple processing of the resultant NPs. To compose the core of the NP we chose to utilize PLGA which has been FDA approved for multiple biomedical applications, and has been broadly applied in the manufacture of NPs through a variety of methods including nanoprecipitation.^{28, 31} To improve NP pharmacokinetics we elected to PEGylate the NP surface. Surface pegylation helps reduce NP aggregation, opsonization and phagocytosis, cellular uptake by non-targeted cells, and improves systemic circulation half-lives by reducing clearance rates by the reticuloendothelial system (RES).^{25, 92} Unlike previously reported methods for composing the NP matrix from PLGA-b-PEG diblock polymers, we chose to titrate in the amount of PEG through incorporation of a PCL-b-PEG diblock polymer (Fig. **3.1**). Like

PLGA, PCL is FDA approved for a variety of applications.³¹ The PCL-b-PEG partitions selectively with PCL segregating into the hydrophobic core of the NP, while PEG partitions onto the solvent exposed surface of the NP (Fig. 3.1).

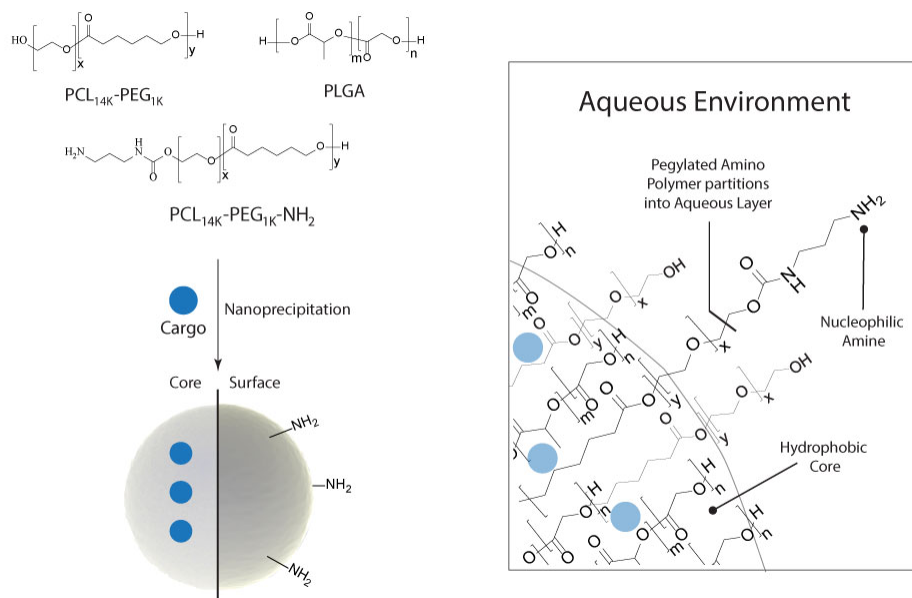


Figure 3.1. Nanoparticle synthesis and design.

Due to the presence of surface bound carboxyl groups from PLGA, or incorporation via PLGA-b-PEG-CO₂H diblock polymers, the predominant avenue for installing functionality onto NP surfaces has been through the formation of activated esters. Chemistries such as N-(3-Dimethylaminopropyl)-N'-ethylcarbodiimide (EDC) have been extensively employed to activate the carboxyl group rendering it susceptible for attack by nucleophilic substrates on biomolecules – a strategy employed for the incorporation of biological targeting agents such as antibodies and aptamers. This strategy however has potential drawbacks. The use of EDC often requires an excess of reagent which could

become associated with the NP making its removal difficult. Further, the use of EDC is often associated with the need for NHS to generate an NHS-ester as a suitable intermediate more stable towards hydrolysis. However, with a half-life of merely 10 min at pH 8.4 and 25 °C processing must be quick to avoid de-activation of the surface substrates. To overcome this, we chose to utilize substrate **2g** through incorporation via a nucleophilic NP surface (Fig. **3.2**). To install this surface, we utilized a similar strategy to that outlined above for the incorporation of PEG. We utilized a PCL-b-PEG-NH₂ polymer which can then be used to titer in the NH₂ functional group at the surface of the NP in the desired ratios. This strategy avoids the need for introducing “activated” functional groups at the NP surface during time-sensitive procedures. This activated surface was then used for the incorporation of the MUC1 specific Ab TAB004 through nucleophilic acyl substitutions.

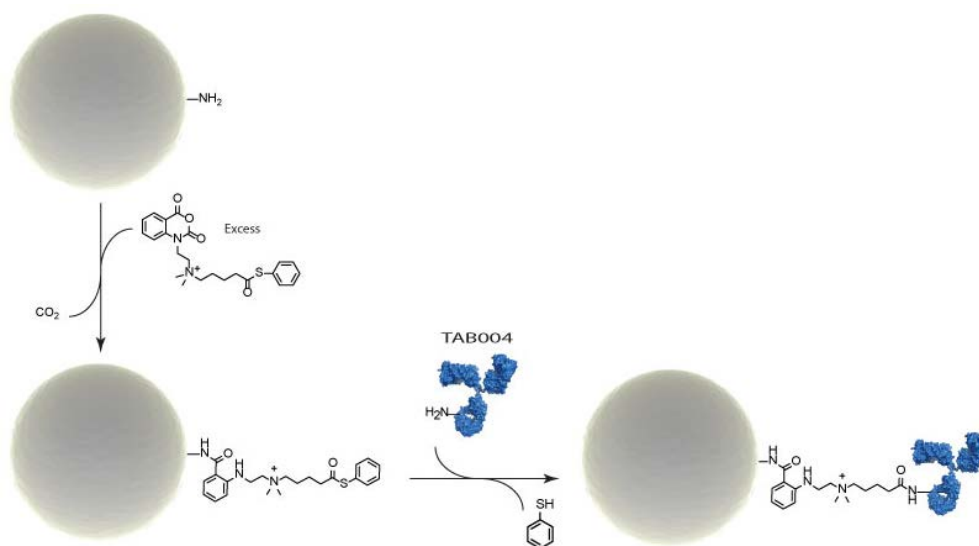


Figure 3.2. Nanoparticle functionalization with reagent **2g** followed by incorporation of TAB004 Ab.

To ensure labeling of the NP surface with the Ab TAB004 is specific, we demonstrated the nucleophilic surface in absence of derivatization with reagent **2g** inhibits Ab binding. We tested the ability for 5% pegylation to inhibit Ab binding by treating NPs with a fluorescein labeled mouse IgG1 (FL-mIgG1) to mimic the isotype of TAB004. 5% Pegylation is effective at inhibiting the non-specific binding of the FL-mIgG1, thereby validating the strategy for titrating the relative amounts of PEG through incorporation of the PCL-b-PEG and PCL-b-PEG-NH₂ polymers.

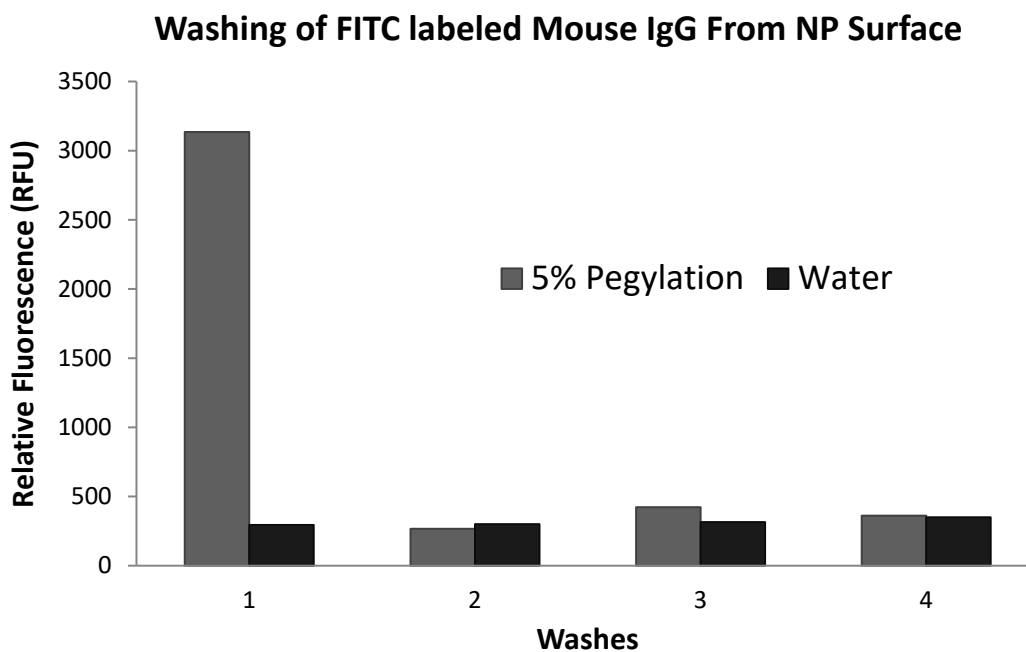


Figure 3.3. Pegylation reduces the amount of nonspecific binding of FL-mIgG1.

Several NP compositions were prepared for this study. For cellular toxicity studies we chose to encapsulate PTX in the NP platform. PTX is a front-line chemotherapeutic for a variety of cancers including pancreatic cancer. Further PTX is used in combination

therapies, and is the subject of several ongoing biomedical studies involving the treatment of pancreatic cancer. PTX is a hydrophobic drug and its incorporation into polymeric nanomaterials has been reported.⁹³⁻⁹⁶ For cellular imaging, fluorescein diacetate (FL(OAC)2), Nile red (NR), and indocyanine green were all encapsulated (Fig. 3.4). Results for these materials are summarized in tables 3.1 and 3.2 below.

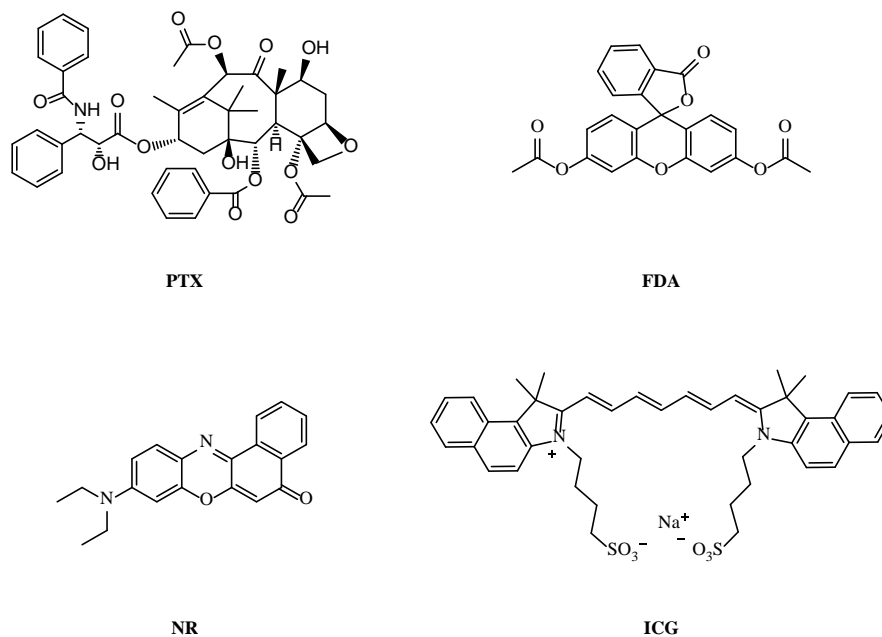


Figure 3.4. Compounds encapsulated in the NP platform. Paclitaxel (PTX), fluorescein diacetate (FDA), Nile red (NR), indocyanine green (ICG).

Table 3.1. Cargo Loading of PTX, FL(OAC)2, NR, and ICG into Nanomaterials

Nanomaterial	Cargo Loading (mg)	Amount Encapsulated (mg /100 mg NPs)	EE (%)
PTX NPs	5	2*	40
FL(OAC)2 NPs	2	.11**	5.5
NR NPs	2	.28**	14
ICG NPs	1.75	.38**	22

EE = Encapsulation Efficiency. * Determined by ¹H NMR. ** Determined by UV-Vis.

Nanomaterial	HD (nm)	PDI	ZP (ζ)
PTX NPs	152.8	.169	-7.6 \pm .2
FL(OAC)2 NPs	192.5	.129	-6.4 \pm .2
NR NPs	227.5	.175	-6.7 \pm .1
ICG NPs	196.1	.076	-6.8 \pm .1

HD = Hydrodynamic Diameter, PDI = Polydispersity Index, ZP = Zeta Potential.

Particle size was characterized by dynamic light scattering (DLS) and scanning electron microscopy (SEM) imaging. Each of the particles formed above are sub 400 nm, and are accordingly expected to be suitable platforms for systemic delivery. Particles in this size range are expected to be colloiddally stable under physiological conditions and be able to accumulate at tumor sites via the EPR effect.

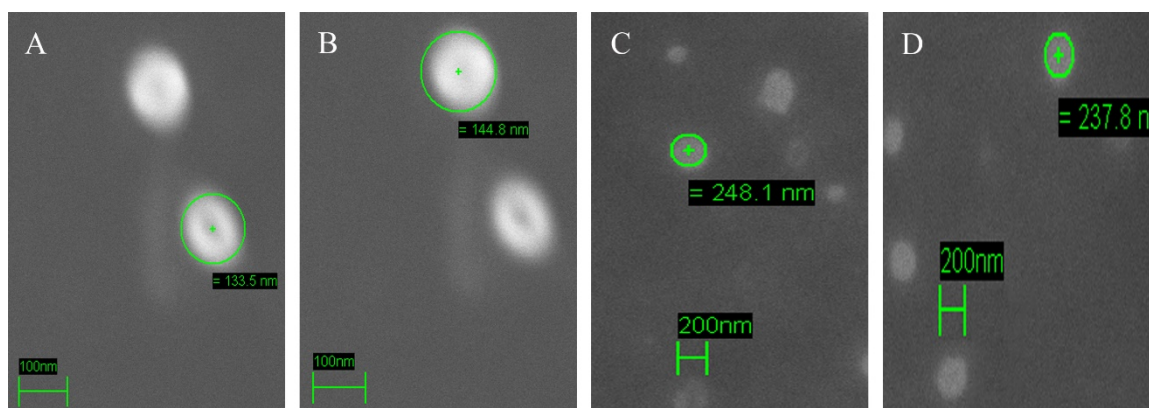


Figure 3.5. SEM images of A. Paclitaxel (PTX) NPs, B. FDA NPs, C. NR NPs, D. ICG NPs. Scales as indicated.

Like other PLGA based NPs reported in the literature, the particles described above all have a negative surface charge (zeta potential, ζ) despite the presence of the amine surface. This ζ is expected as the amines only account for a very small portion of the total weight of the NP composition. The dominant contributor to the surface charge of the NP is expected

to be the core matrix material (PLGA) which presents surface carboxyl and hydroxyl groups in an orientation dependent manner.

To further characterize the NPs we chose to study the release of FL(OAC)₂ as a model compound (Fig. 3.4). FL(OAC)₂ has several characteristics which make it an ideal model compound. First, it is hydrophobic making it a tractable mimetic for many chemotherapeutics. Secondly, its fluorescence is only visible upon hydrolysis of its esters only possible upon release from the NP. Finally, detection of its fluorescence enables highly sensitive detection possible. These characteristics make method development simple, and use of very small amounts of valuable material feasible. Release of FL(OAC)₂ from model NPs shows a gradual release from NP over 120 hrs. This release profile is ideal, as systemic distribution requires time for NP accumulation at tumor sites.

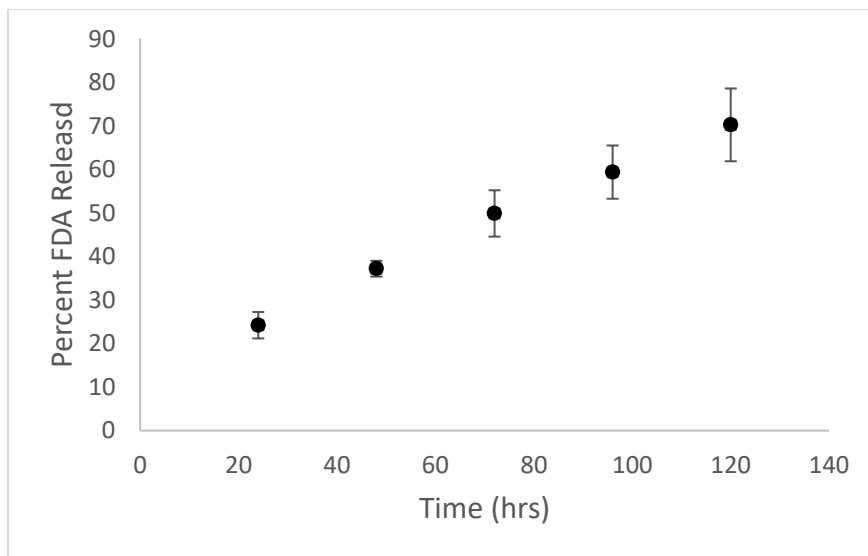


Figure 3.6. FDA release profile from NPs (1 mg/ml) in PBS at pH 7.4. Results are mean \pm SD, $n = 3$.

PLGA NPs Internalize into BxPC3. We determined the PLGA NPs internalized into BxPC3 pancreatic ductal adenocarcinoma (PDA) cell line (Fig. 3). BxPC3 cell lines were treated for 1.5 hours with FL(OAC)2 and Nile Red loaded NPs. This matched the total treatment time of PDA cell lines in the cell viability assay. After 1.5 hours FL(OAC)2 loaded PLGA NPs internalize through endocytosis and punctate green fluorescence, from the hydrolysis of FL(OAC)2 in the NPs, can be seen inside the cells, indicating internalization of the NPs (Fig. 3). Overall, cellular uptake of PLGA NPs without TAB004 conjugation in PDA cell lines is expected.⁹⁷

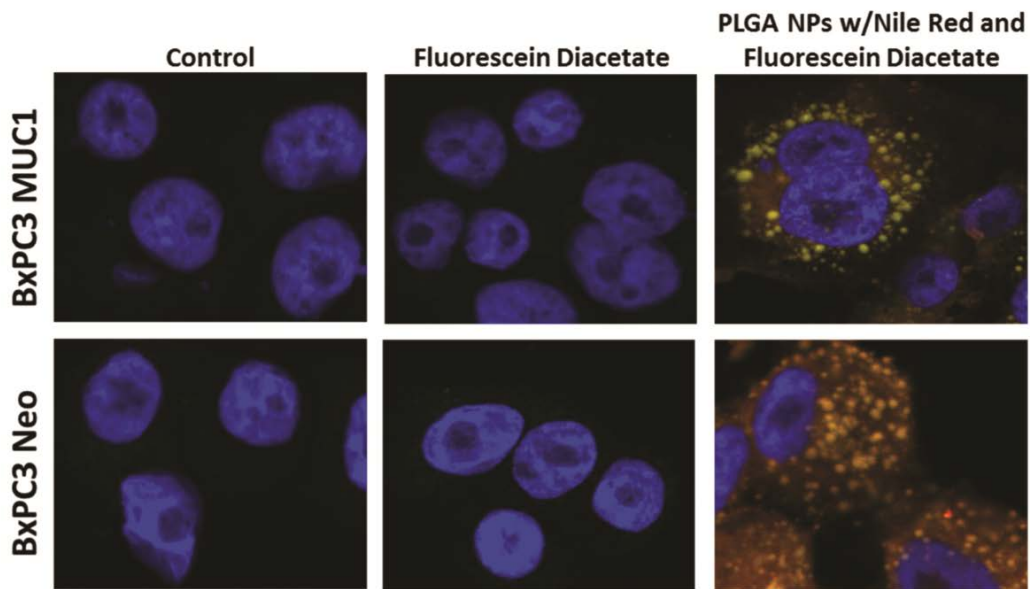


Figure 3.7. Internalization of PLGA NPs in: (A) BxPC3 MUC1; (B) BxPC3 Neo. Results shown are representative images (n=3).

PTX loaded PLGA NPs Decrease Cell Viability in PDA Cells. Next, we determined if PTX loaded NPs were more efficacious than PTX by itself. We compared the cytotoxicity of PTX loaded NPs to PTX alone *in vitro* using the MTT assay. The amount of PTX in the NPs is ~ 2% (wt/wt). A dose-dependent cell death was observed with PTX in for HPAC and HPAF-II cells (Fig. 4). HPAC and HPAF-II cells are highly resistant to killing by PTX but when treated with PTX enclosed in PLGA NPs, the cells respond to the PTX in a dose dependent manner. A significant decrease in cell viability between PTX loaded NPs and PTX alone was detected at higher concentrations in all cell lines (Fig. 4). We were able to reach the IC50 for BxPC3 Neo, BxPC3 MUC1, and MIA PaCa-2 with both PTX-loaded NPs and PTX alone (Fig. 4A-C), but were only able to do so in HPAF-II and HPAC with the NPs, not PTX alone (Fig. 4D, E). Each of the cell lines tested saw a significant decrease in cell viability when treated with PTX loaded NPs compared to PTX alone at the higher concentrations - even though the amount of PTX in NPs was the same as the free PTX in this study. Although studies performed herein characterizing the release of NP cargo modeled on FL(OAC)2 demonstrate a slow release profile, the internalization of NPs via endocytic pathways have been associated with increased NP degradation and therefore increased rates in release profiles. Albeit, the release of PTX release is expected to increase time-dependent concentrations of PTX compared to free PTX, and result in increase intracellular residence times of PTX during the course of the experiment. Results obtained herein could therefore be a result of the treatment benefiting from the slow release profile of the NPs,^{98,99} due to effective increase in intracellular accumulation of PTX.

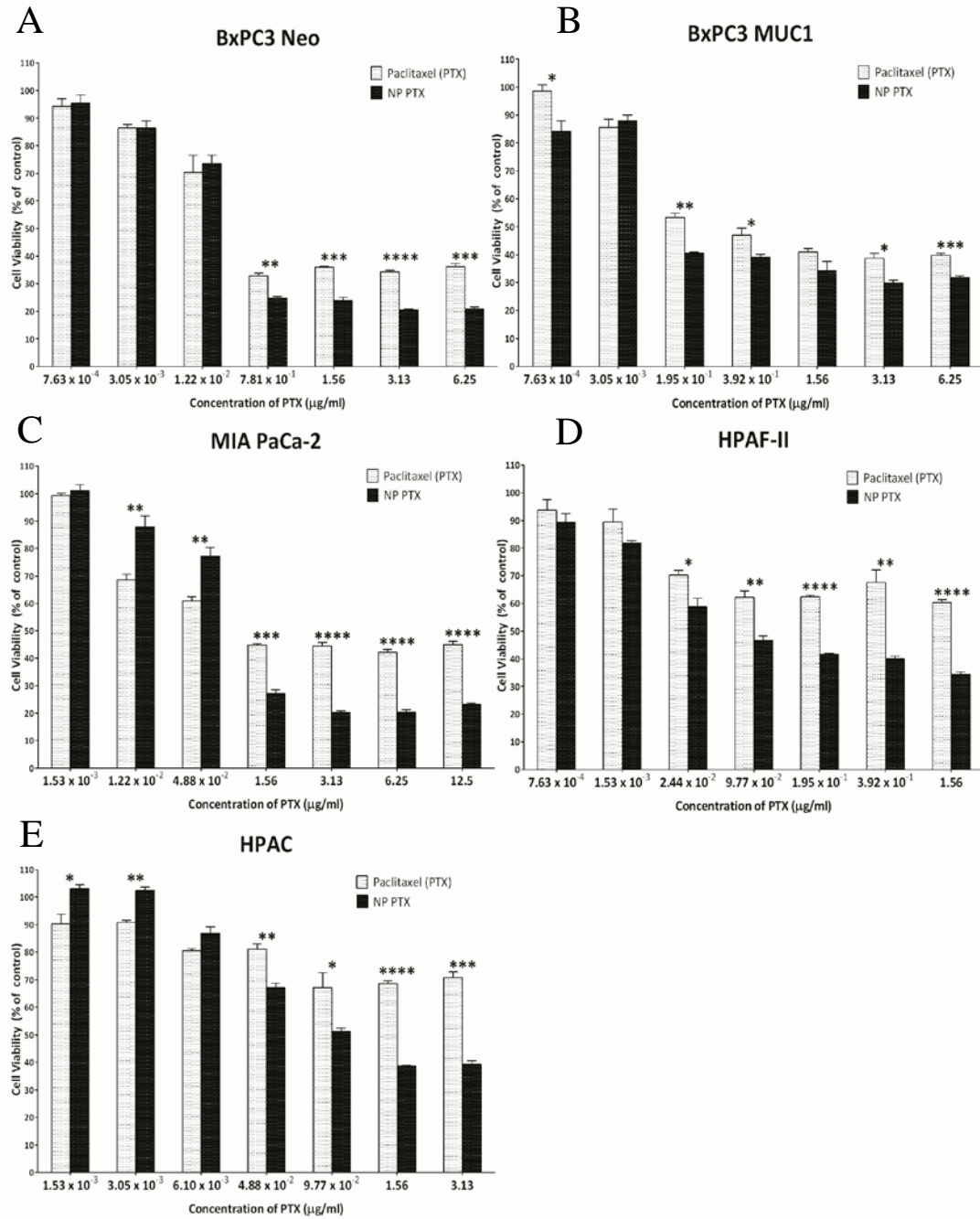


Figure 3.8. Cell viability of PDA cell lines treated with PTX and PTX loaded NPs: (A) BxPC3 Neo; (B) BxPC3 MUC1; (C) MIA PaCa-2; (D) HPAF-II; (E) HPAC. Data are shown as mean \pm SEM (n=3) and determined by a one-sided t-test comparing treatment groups at each concentration, * $p < 0.05$, ** $p < 0.01$, *** $p < 0.001$, **** $p < 0.0001$.

TAB004 Antibody is Specific for and Internalizes into PDA Cell Lines. We determined the specificity and quantified the internalization of TAB004 antibody by fluorescent microscopy (Fig. 5). The presence and uptake of TAB004 was visualized by conjugating the antibody to pHrodo Red, which is non-fluorescent outside the cell, but fluoresces red during endocytosis (Fig. 5A). The fluorescent signal from TAB004 is significantly increased in BxPC3 MUC1 when compared to BxPC3 Neo at all time points (Fig. 5B). There is some internalization observed in BxPC3 Neo, which can be caused by the very low level of endogenous MUC1 that is present, or by non-specific endocytosis as PDA cells have been shown to actively swallow their surroundings through micropinocytosis.

100, 101

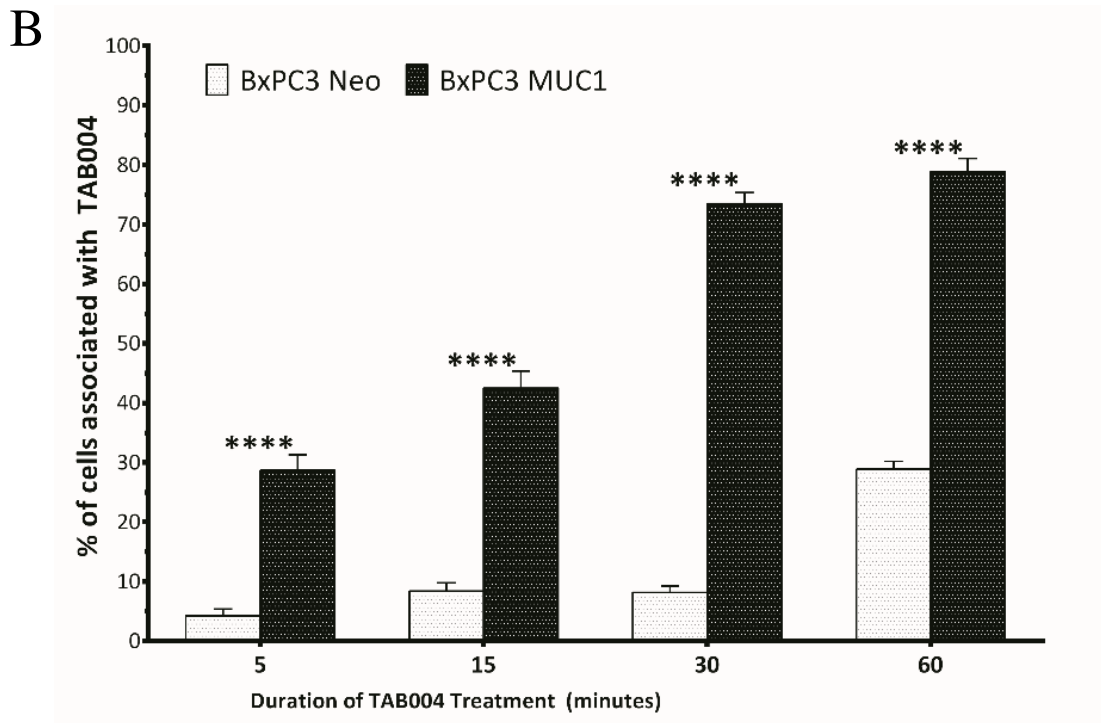
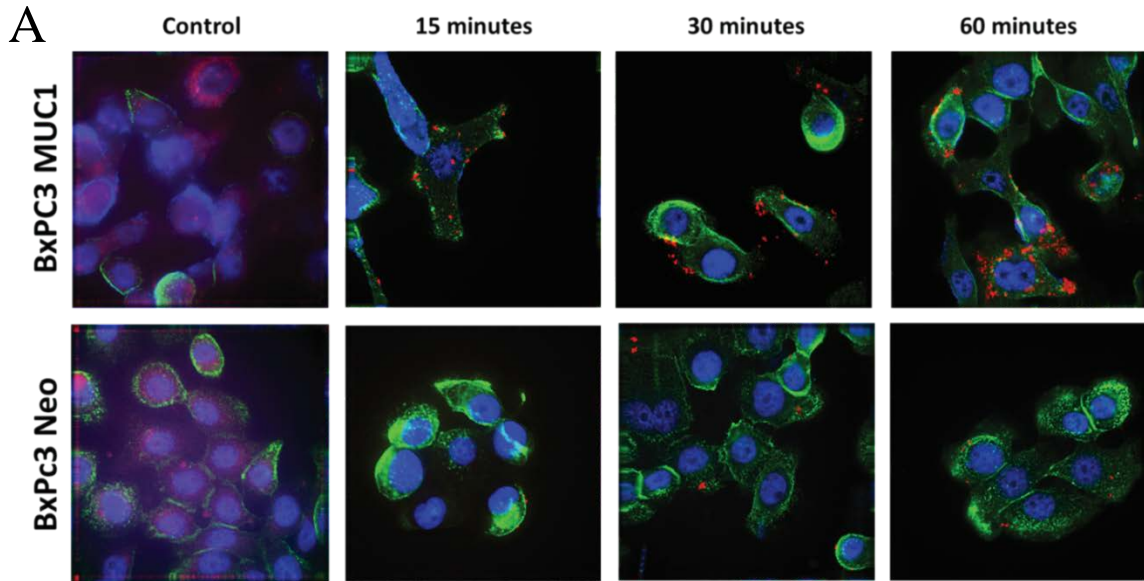


Figure 3.9. Specificity and internalization of TAB004 in BxPC3 MUC1 and Neo: (A) representative images cells treated with TAB004 conjugated to pHRedo red (n=3); (B) quantification of images determine by the number of cells associated with TAB004 divided by total number of cells. Data are shown are mean \pm SEM (n=3) and determine by two-way ANOVA and Bonferroni's post-hoc test, *p<0.05, **p<0.01, ***p<0.001, ****p<0.0001.

Specificity and Cell Viability Evaluation of TAB004 Conjugated PTX loaded PLGA NPs. The successful conjugation of TAB004 to the surface of the NPs (T-NPs) was determined by flow cytometry (Fig. 3.9). The linking reagent, a thioester, was tested and successful in linking TAB004 to the NPs (Fig 3.9B). Flow cytometry data shows a shift in fluorescence when NPs are conjugated to TAB004 and labeled with anti-mouse IgG1 FITC. Unconjugated NPs did not display any shift in fluorescence (Fig 3.9A). NPs without linking reagents but treated TAB004, anti-mouse IgG1 FITC, or both also served as controls and as expected did not show any shift in fluorescence signal. This suggests that the linker was successfully at conjugating. To determine if NP internalization could be affected by the presence of TAB004, BxPC3 MUC1 and BxPC3 Neo were treated with FL(OAC)2 loaded T-NPs over a time period (Fig. 3.10A, B). No significant increase in fluorescence between FL(OAC)2 loaded NPs and FL(OAC)2 loaded T-NPs was observed in BxPC3 Neo (Fig. 3.10C). A significant increase in fluorescence between FL(OAC)2 loads NPs and FL(OAC)2 loaded T-NPs was observed at 60 and 90 minutes in BxPC3 MUC1 (Fig. 3.10D). The data indicates that linking TAB004 to the NPs was highly effective in longer term retention of the NPS within the cells compared to NPs alone and that this retention was antigen specific.⁹⁷ Therefore, we next determined the cytotoxicity of PTX loaded T-NPs compared to PTX loaded NPs in the same cells (BxPC3.Neo and BxPC3.MUC1) as well as in a panel of other PDA cell lines with varying levels of MUC1 expression and sensitivity to PTX (Fig.3.11). There was a significant decrease in cell viability when BxPC3 Neo was treated with T-NPs at the lowest concentration, but all other concentrations either did not have any significant differences or the NPs caused more cytotoxicity than the T-NPs (Fig. 3.11A). This was expected based on the low MUC1

expression and the similar retention of the NPs versus T-NPs in the BxPC3.Neo cells (Fig. 3.10C). On the other hand, BxPC3 MUC1, MIA PaCA-2, and HPAC all saw significant decreases in cell viability with PTX loaded T-NP treatment at high and low concentrations of PTX as compared to PTX-loaded NPs (Fig. 3.11B, C, and E). Significant decreases in cell viability was also observed in HPAF-II, but only in 3 of the higher concentrations (Fig. 3.11D). Overall, the addition of TAB004 to the surface of the PTX-loaded NPs decreased cell viability when compared to NPs alone. Although the effect of T-NPs versus NPs is modest, it is highly significant for the very resistant cell lines such as HPAFII and HPAC. We speculate that *in vivo* the effect would be more pronounced. The fact that these cells are only treated for 1.5hrs and then all drugs washed out from the cell culture suggests that the modest efficacy of T-NPs versus NPs may likely be due to the limitations of the *in vitro* cell viability assay.

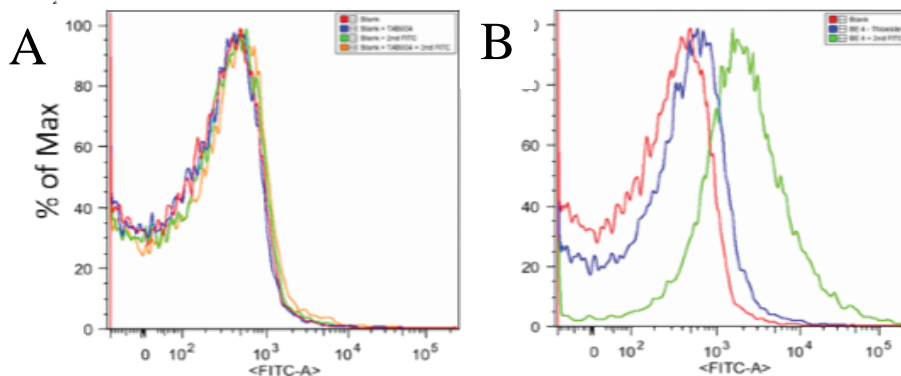


Figure 3.10. Confirmation of TAB004 conjugation to PLGA NPs with FACS. Blank NPs were treated with: (A) control (red), TAB004 (blue), anti-mouse IgG₁ FITC (green), and both TAB004 and anti-mouse IgG₁ FITC (orange/yellow); (B) control (red), reagent **2f** (blue), and Thioester linking reagent, TAB004, and anti-mouse IgG₁ FITC (green)

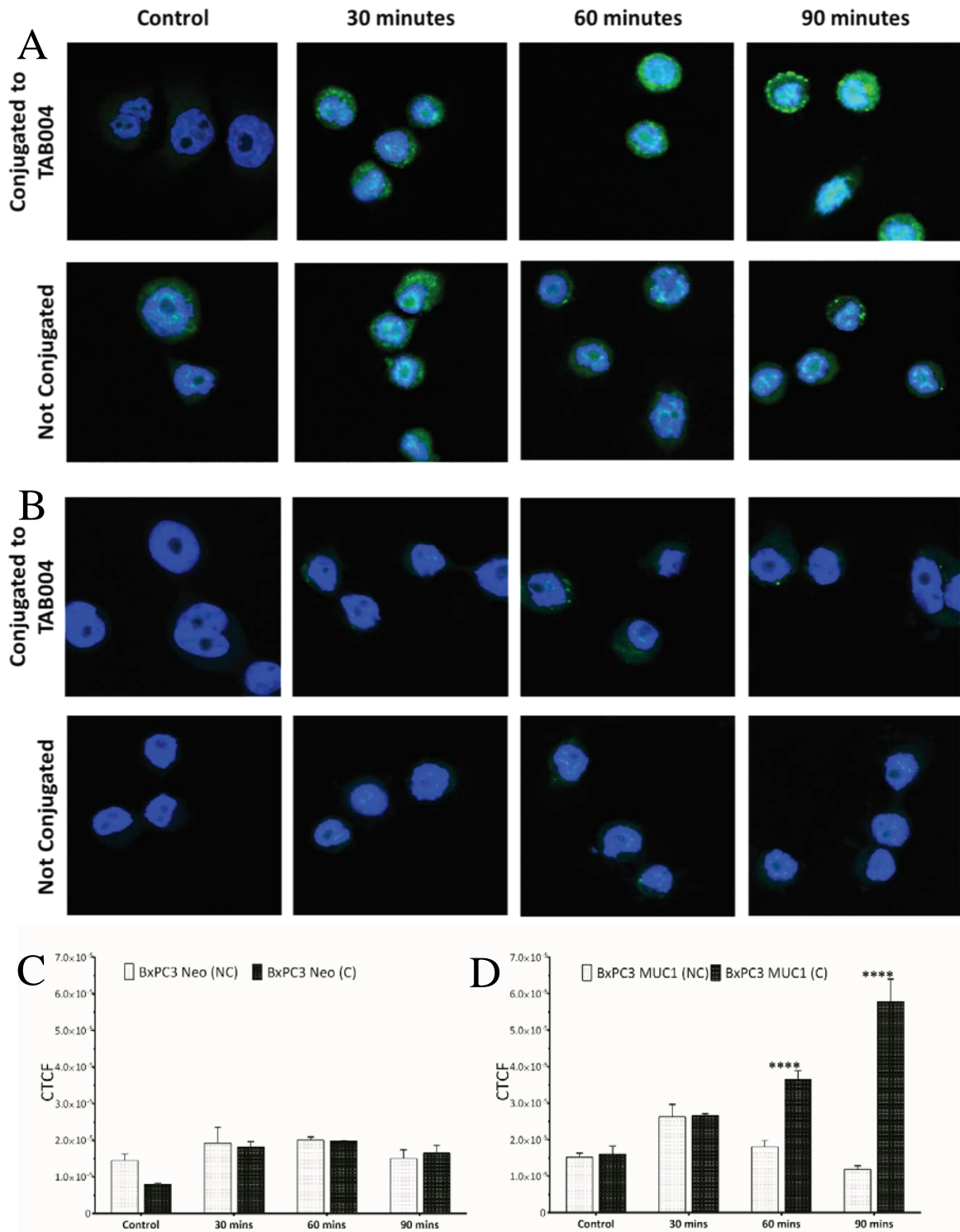


Figure 3.11. Internalization of T-NPs loaded with fluorescein diacetate (FDA): (A) representative images of BxPC3 MUC 1 (n=3) treated with T-NPs; (B) representative images of BxPC3 Neo (n=3) treated with T-NPs; (C) and (D) quantification of fluorescence using Image J to determine corrected total cell fluorescence (CTCF). Data are shown as mean \pm SEM (n=3) and determined by a one-sided t-test, * p <0.05, ** p <0.01, *** p <0.001, **** p <0.0001.

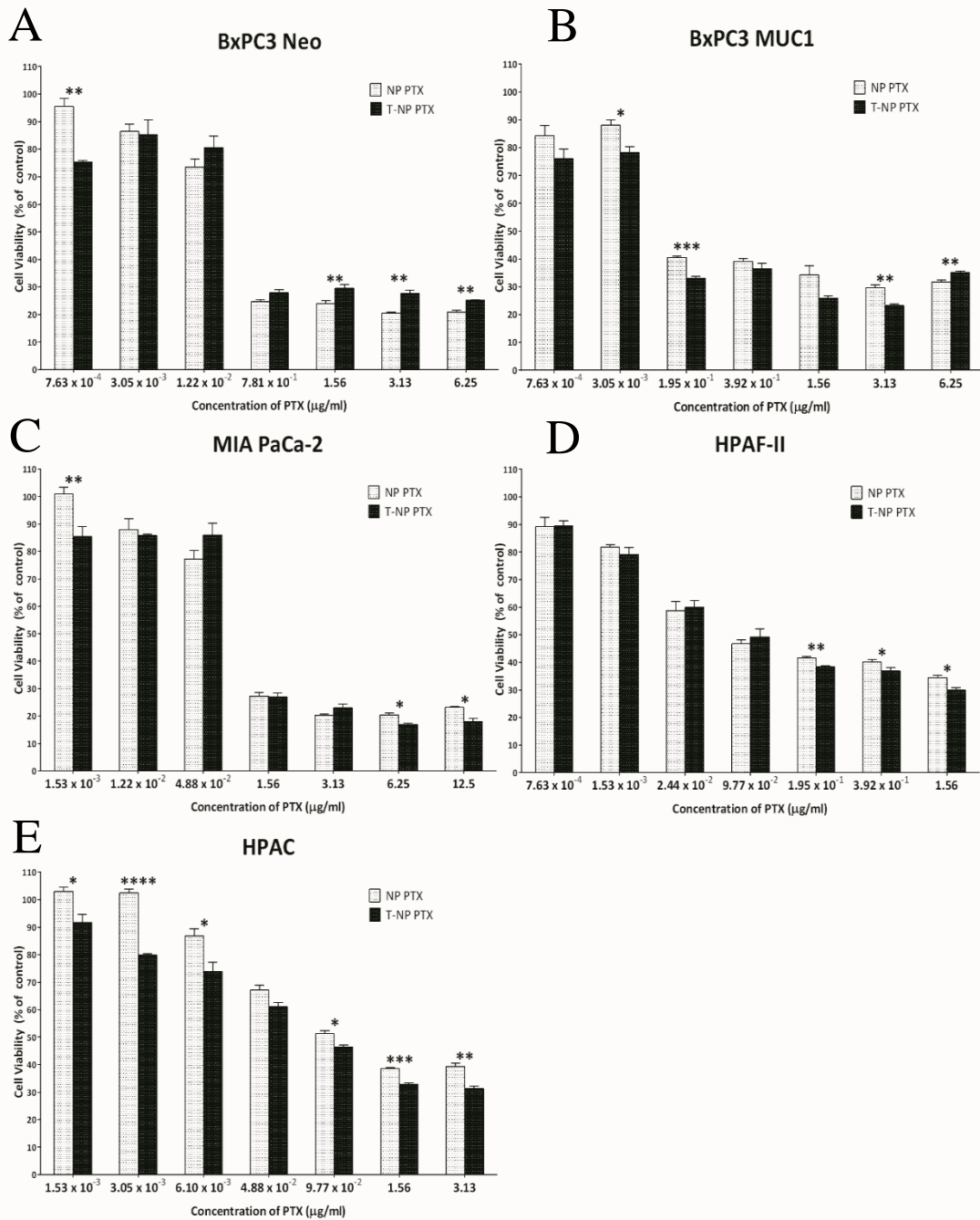


Figure 3.12. Cell viability of PDA cell lines treated with PTX loaded NPs and PTX loaded T-NPs: (A) BxPC3 Neo; (B) BxPC3 MUC1; (C) MIA PaCa-2; (D) HPAF-II; (E) HPAC. Data are shown as mean \pm SEM (n=3) and determined by a one-sided t-test comparing treatment groups at each concentration, * $p < 0.05$, ** $p < 0.01$, *** $p < 0.001$, **** $p < 0.0001$.

Targeting Properties of TAB004 Conjugated PLGA NPs in Orthotopic PDA Tumor

Model. We demonstrated the specificity of TAB004 *in vitro*, but the same needed to be determined *in vivo*. C57BL/6 immune competent mice bearing murine syngeneic pancreatic orthotopic tumors (KCM tumors) were injected intraperitoneal with TAB004 conjugated with indocyanine green (ICG) and imaged 24 hours post injection. These KCM cells stably express the luciferase gene and can therefore be visualized via imaging post luciferin injection. TAB004 localizes and persists specifically at the tumor site 24 hours later (Fig. 3.12). Images of 4 representative mice are shown. It is clear that the TAB 004-ICG localizes to the bioluminescent pancreatic tumors.

Next, we tested ICG loaded NPs and ICG loaded TAB004-conjugated NPs in C57BL/6 mice bearing the same bioluminescent murine syngeneic pancreatic orthotopic tumors to determine if TAB004 can increase the accumulation of NPs at the tumor site (Fig. 3.13). ICG loaded NPs appear to clear from the mouse between 24 and 48 hours post injection (Fig. 3.13A), similar to the biodistribution profile of ICG loaded NPs injected in non-tumor bearing mice (data not shown). ICG loaded T-NPs displayed greater accumulation and persistence at the tumor site 24 and 48 hours post injection (Fig. 3.13B). *Ex vivo* images of the tumor and liver of the mice were taken 48 hours post injection. It is clear that the ICG loaded T-NPs are accumulating and persisting in the tumor more than the ICG load NPs, while fluorescence in the liver, where a majority of nanoparticles tend to accumulate, of both mice are relatively identical (Fig. 3.13C). These results suggest that TAB004 conjugated to NPs is a potential platform for targeted delivery of not only PTX, but many other drugs, to pancreatic cancer, significantly enhancing the treatment efficiency and

decreasing the risks of serious side effects. The next study will evaluate the *in vivo* anti-tumor efficacy in several models of PDA.

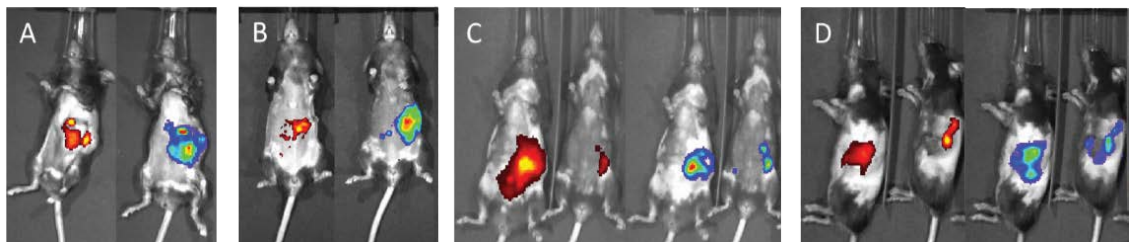


Figure 3.13. *In vivo* imaging of TAB004-ICG in orthotopically injected bioluminescent tumor bearing mice (ICG - red/yellow, tumor – rainbow, n=4): (A) mouse 1; (B) mouse 2; (C) mouse 3 and 4 ventral view; (D) mouse 3 and 4 side view.

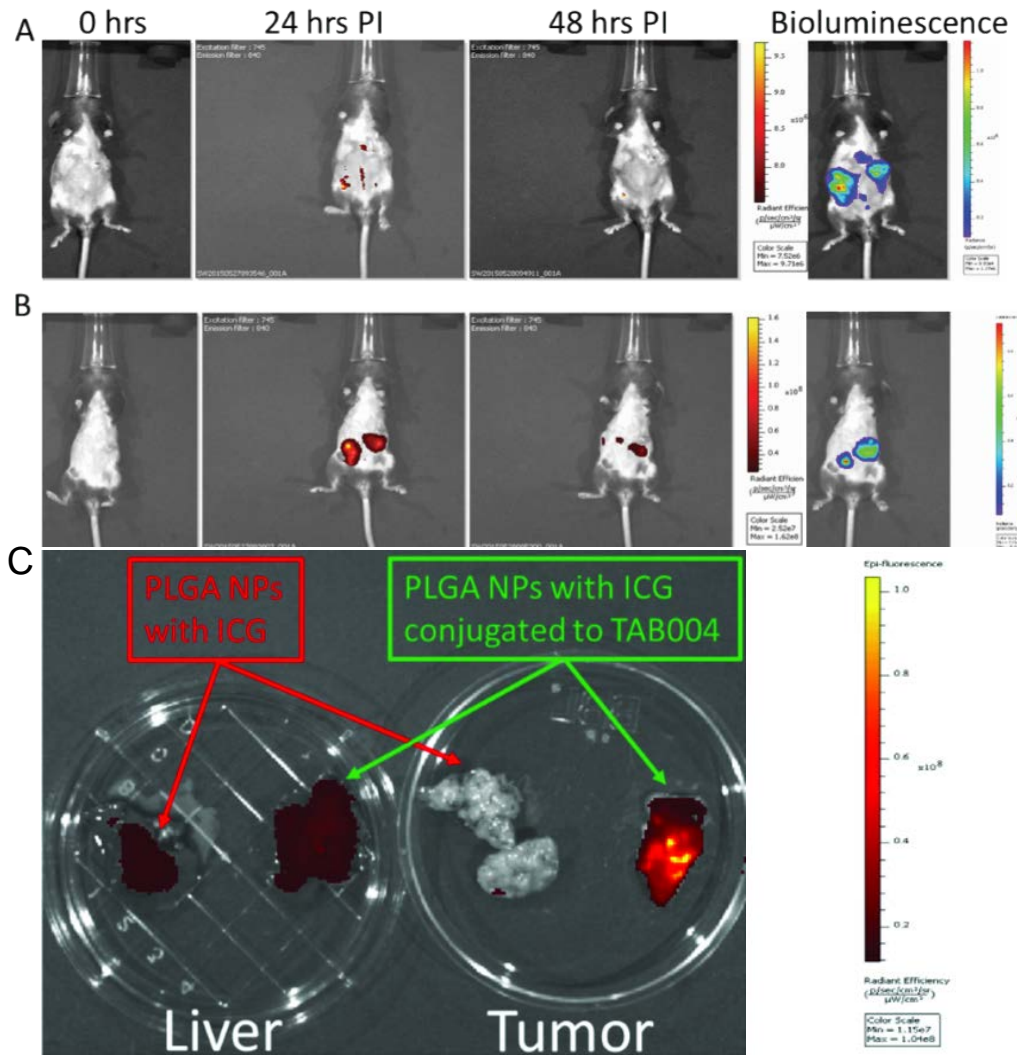


Figure 3.14. *In vivo* imaging of ICG loaded NPs and ICG loaded T-NPs orthotopically injected bioluminescent tumor bearing mice (ICG - red/yellow, tumor – rainbow, n=3): (A) ICG loaded NPs injected into tumor bearing mouse; (B) ICG loaded T-NPs injected into tumor bearing mouse; (C) *ex vivo* imaging of liver and tumor from (A) and (B).

3.3 Conclusion

In this study we aimed to investigate the use of polymeric NPs conjugated with a MUC1 specific Ab (T-NPs) for the targeted delivery and uptake by PDA cells and tumor models. Herein we have demonstrated the *in vitro* and *in vivo* efficacy of the T-NPs against a PDA cell panel and an orthotopic PDA mouse model bearing murine syngeneic pancreatic orthotopic tumors (KCM tumors). These T-NP bioconjugates have the benefit of being prepared from materials which are already FDA approved, are modular in design, and are generated from a relatively simple fabrication process which can be readily scaled for production scale manufacture. Using this modular design, we postulate NPs can be prepared having an assortment of cargoes, and targeting agents for the generation of a comprehensive NP platform for the treatment and diagnosis of other critical diseases.

3.4 Material and Methods

All chemical reagents use for the study were of analytical grade and above. Poly(DL-lactide-co-glycolide) M_w 20,000 (PLGA) (50:50) PolySciences, Inc. (Warrington, PA). Polyethylene glycol M_w 1000 (PEG₁₀₀₀), Poly(vinyl alcohol) MW 6000 (PVA) (80 mol% hydrolyzed), 1,1'-carbonyldiimidazole (CDI), 1,3-diaminopropane (DAP), Dextrose were purchased from Sigma Aldrich (St. Louis, MO). Paclitaxel was purchased from Matrix Scientific (Columbia, SC), ICG was purchased from Chem-Impex (Wood Dale, IL). TAB004 monoclonal antibody was obtained from OncoTAb, Inc. (Charlotte, NC, USA).

Cell Culture. BxPC3, HPAC, HPAFII, and MIA PaCa-2 were purchased from ATCC (Manassas, VA). HPAC, HPAF II, and MIA PaCa-2 were maintained in Dulbecco's modified Eagle's medium (DMEM, 11965-092, Gibco). BxPC3 cell lines were maintained in RPMI medium 1640 (RPMI, 11875-093, Gibco). Growth media for these cell lines were supplemented with 10% fetal bovine serum (FBS, Gibco), 3.4mM L-glutamine, 90 units (U) per ml penicillin, and 90µg/ml streptomycin (Cellgro).

Determination of NP loading. For the PTX NP formulation a 20 mg sample of was dissolved into 600 µl of DMSO-*d*6 and the concentration of the respective cargo determined using ¹H NMR at 25 °C by comparing unique resonances of the cargo to the methylene residue of PLGA at [5.2 ppm]. For the FL(OAC)2, ICG, and NR NP formulations, a sample of nanomaterial (2-4 mg) was dissolved into DMSO and the amount of cargo quantified by UV-Vis.

$$\text{Encapsulation Efficiency} = \frac{\text{Amount of cargo encapsulated}}{\text{Amount of cargo used}} \times 100$$

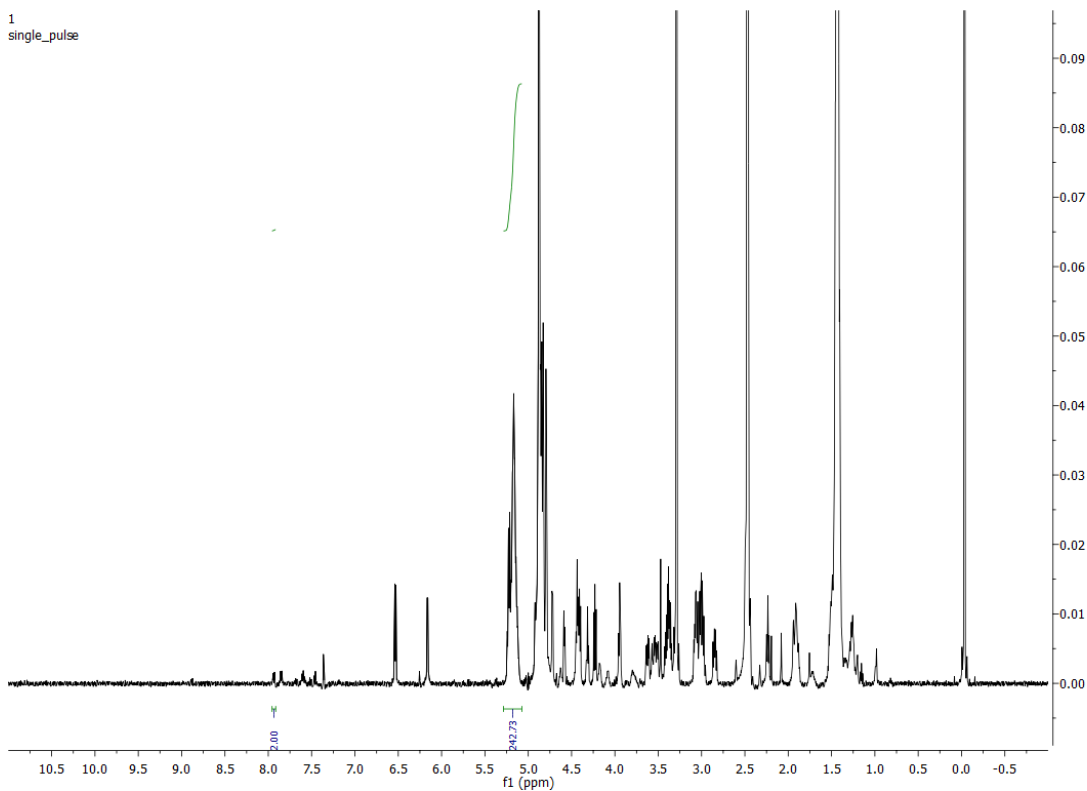


Figure. 3.15. Representative ^1H NMR (DMSO- d_6 , 500 MHz) for determining PTX Loading.

Determination of NP size and polydispersity. Particle size, polydispersity index (PDI), along with zeta potential were performed using a Zetasizer Nano (Malvern Instruments).

Cargo Release Profiles. Release profiles of NPs were modeled using FL(OAC)2 NPs. The release characteristics of these particles were characterized in phosphate buffered saline (PBS) at pH 7.4.

Synthesis of PCL_{14K}-PEG₁₀₀₀. PCL_{14K}-PEG₁₀₀₀ was prepared according to the following procedure. Polycaprolactone (2 g, $M_w \sim 14,000$) was added to a 50 ml oven dried round-bottom flask fitted with a claisen adapter and equipped with a magnetic stir bar, a rubber septum, and a reflux condenser with attached drying tube. To this was added 20 ml of thionyl chloride via syringe, and the rubber septum replaced with a ground-glass stopper, and the resulting solution heated to reflux for 3 hrs. The thionyl chloride was then removed under reduced pressure using a rotary evaporator. The resulting residue was placed under a nitrogen atmosphere and 50 ml of freshly distilled THF was added by cannula followed by PEG₁₀₀₀-diol (2.9 g, 20 equivalent) and triethylamine (2ml, 14.35 mmol). The resulting solution was left to stir for 18 hrs at room temperature. This solution was then poured into 500 ml of DI water under vigorous stirring to precipitate the desired product and remove unreacted PEG₁₀₀₀ diol. The precipitate was isolated by filtration, re-dissolved into THF (50 ml), and precipitated as before. This process was repeated three times. Finally, the isolated product was dried under vacuum at 25 °C for 72 hrs. The desired product was isolated as a solid white material (1.13 g, 53 %). ¹H NMR (500 MHz CDCl₃): δ 1.36 (m, -CH₂CH₂CH₂-), 1.63 (m, -CH₂CH₂CH₂-), 2.28 (t, -C(O)CH₂-), 3.62 (s, -OCH₂CH₂-), 4.04 (t, -OCH₂).

Synthesis of PCL_{14K} -PEG₁₀₀₀-NH₂. PCL_{14K} -PEG₁₀₀₀-NH₂ was prepared by the according to the following procedure. PCL_{14K} -PEG₁₀₀₀ (1 g) was added to a 50 ml oven dried 2-neck round-bottom flask equipped with a magnet stir bar and a rubber septum with nitrogen inlet. To this was added 20 ml of dry methylene chloride (DCM) followed by 1,1'-carbonyldiimidazole (100 mg, .62 mmol) and the resulting solution left to stir for 6 hrs at

room temperature. To this was added 1,3-diaminopropane (1 ml, 12.19 mmol) and the resulting solution left to stir for 12 hrs at room temperature. The DCM was then removed under reduced pressure using a rotary evaporator. The resulting viscous yellow liquid was dissolved into THF (20 ml) and precipitated by pouring the solution into 250 ml of vigorously stirred DI water. The precipitate was isolated by filtration, re-dissolved into THF (20 ml), and precipitated as before. This process was repeated three times. Finally, the isolated product was dried under vacuum at 25 °C for 72 hrs. The desired product was isolated as a yellow solid (0.5 g, 50%). Although the resonances for the end-group -C(O)NHCH₂CH₂CH₂NH₂- are not assigned due to obfuscation of these resonances by the polymer backbone, the polymer tested positive for the presence of primary amines using the Kaiser test. ¹⁰² ¹H NMR (500 MHz CDCl₃): δ 1.37 (m, -CH₂CH₂CH₂-), 1.64 (m, -CH₂CH₂CH₂-), 2.29 (t, -C(O)CH₂-), 3.63 (s, -OCH₂CH₂-), 4.05 (t, -OCH₂).

Nanoparticle preparation: general method. Nanoparticles (NPs) were prepared by the nanoprecipitation method. Briefly; 100 mg of PLGA (50:50, M_w ~ 20 K), 5 mg of PCL-PEG₁₀₀₀, 1 mg PCL-PEG₁₀₀₀-NH₂, and 1 - 5 mg of cargo was dissolved into 10 ml of acetone. This solution was then added dropwise via syringe into a stirred solution of 1% PVA (20 ml) at a rate of 90 ml/hr controlled using a syringe pump. The resulting colloidal suspension was then transferred to a 100 ml round-bottom flask, and the acetone removed under reduced pressure using a rotary evaporator. NPs were then purified by centrifugation (25 min, 30,000 × g) using three successive washes of sterile filtered 18 Ω water at 4 °C. The resulting NP pellet was then resuspended into sterile filtered 18 Ω water (10 ml), whereupon dextrose (10 mg) was added as a lyoprotectant. This colloidal suspension was

then flash frozen in liquid nitrogen then lyophilized at 25 °C and 50 mTorr for 24 - 48 hrs resulting in a flocculent solid. Paclitaxel (PTX), Fluorescein Diacetate (FL(OAC)₂), and Nile Red (NR) were all prepared according to the general method described above. See table 1 for the amount of cargo used in the preparation of the respective nanomaterials.

Indocyanine green (ICG) preparation. ICG NP's were prepared similar to the general method with minor modification. Briefly; 100 mg of PLGA (50:50, $M_w \sim 20$ K), 5 mg of PCL-PEG₁₀₀₀, 1 mg PCL-PEG₁₀₀₀-NH₂ was dissolved into 9 ml of acetone. Meanwhile 1 mg of ICG was dissolved into 1 ml of sterile filtered 18 Ω water. The two solutions were then mixed, and vortexed rapidly for 2 min. The resulting solution was then added dropwise via syringe into a stirred solution of 1% PVA (20 ml) at a rate of 90 ml/hr controlled using a syringe pump. The resulting colloidal suspension was then transferred to a 100 ml round-bottom flask, and the acetone removed under reduced pressure using a rotary evaporator. NPs were then purified by centrifugation (25 min, 30,000 × g) using three successive washes of sterile filtered 18 Ω water at 4 °C. The resulting NP pellet was then resuspended into sterile filtered 18 Ω water (10 ml), whereupon dextrose (10 mg) was added as a lyoprotectant. This colloidal suspension was then flash frozen in liquid nitrogen, and lyophilized at 25 °C and 50 mTorr for 24 - 48 hr. resulting in a flocculent green solid.

FL(OAC)2 Release Profiles. 1 ml Solutions of FL(OAC)2 NPs (1 mg/ml) were incubated with constant stirring at 37 °C over 72 hrs. 100 µl samples were taken at the indicated time-points and centrifuged (16,000 x g) to pellet out the remaining NPs. 50 µl of NP free buffer was removed carefully so as not to disturb the pellet, and 20 µl of 5% NaOH added to hydrolyze the liberated FL(OAC)2. Absorbance measurements were recorded at 490 nm. These values were compared to a control sample having been dissolved in a 50:50 ACN:H₂O solution to liberate the entire sample of FL(OAC)2 from the NPs, and hydrolyzed as above.

SEM Imaging. Lyophilized nanoparticles were re-suspended in H₂O at 0.01 mg/mL concentrations and sonicated for 10 s. Samples were placed on SPI 5x5 silicon chips and dried overnight at 40 °C. Scanning electron microscopy (SEM) images were obtained with a Raith 150 microscope operated at 10 kV.

Generation of BxPC3 MUC1, BxPC3 Neo, and KCM-Luc. MUC1 WT was cloned into the pLNCX.1 vector consisting of the neomycin resistance gene for retroviral infection. GP2-293 cells were transfected with MUC1 WT and pVSV-G vectors and the resulting viral supernatant used to infect BxPC3 cells. Cells designated as BxPC3 MUC1 represents cells expressing full length MUC1 that consists of the extracellular domain, the transmembrane domain and wild type cytoplasmic tail domain. Cells designated as BxPC3 Neo represent cells that only express an empty vector control and therefore represents the endogenous levels of MUC1 in these cells. KCM cell line was generated by the Mukherjee lab from spontaneous PDA tumors from KCM mice. This cell line expresses both mouse

Muc1 and human MUC1. Retroviral transduction of KCM cells with MSCV Luciferase PGK-Hygro (MSCV Luciferase PGK-hygro was a gift from Scott Lowe, Addgene plasmid # 18782) was performed by transfecting GP2-293 cells with the MSCV Luciferase PGK-Hygro and pVSV-G vectors and using the subsequent viral supernatant to infect KCM cells.

Conjugation of TAB004 to PLGA NPs. TAB004 conjugation to PLGA nanoparticles was performed using reagent **2f**. PLGA nanoparticles were weighed out into an appropriate Eppendorf tube. To a vial containing 1 mg of the **2f** was added 1 drop of DMSO to assist with dissolution, then 500 μ l of 18 Ω H₂O was added. The solution was vortexed until all of the labeling reagent was dissolved. The PLGA nanoparticles were re-suspended in 200 μ l of 18 Ω H₂O. The labeling solution was added dropwise to the nanoparticles while under a gentle vortex and allowed to incubate at room temperature for 15 min after mixing. The labeled nanoparticles were centrifuged at 21,000 rcf and 4 °C to pellet them. The supernatant was removed and the labeled nanoparticles re-suspended in 200 μ l of 18 Ω H₂O. 30 μ g of TAB004 at mg/ml conc (in azide free buffer) was then added to the labeled NP solution in one portion. The next day, the nanoparticles were centrifuged at 21,000 rcf and 4 °C to pellet them and the supernatant discarded. Nanoparticles were re-suspended into desired working volume of PBS. Successful TAB004 conjugation to the PLGA nanoparticle was confirmed using FACS (BD Fortessa) and an anti-mouse IgG₁-FITC secondary antibody.

Cell Viability Assays. Cell viability assays were performed using MTT (3-(4,5-Dimethylthiazol-2-yl)-2,5-Diphenyltetrazolium Bromide) (Fisher Scientific, USA). Optimal number of cells per cell line were plated into 96-well tissue culture plates to ensure cells would not be over confluent after 48 hours post treatment. 24 hours after cells were plated, they were treated with corresponding concentrations of dimethyl sulfoxide (DMSO), PTX, blank PLGA nanoparticles, PTX loaded PLGA nanoparticles, and TAB004 conjugated PTX loaded PLGA nanoparticles for 1.5 hours. After 1.5 hours the treatments were washed off with 1x PBS and 200 μ l of fresh media was added to the wells and cell lines were incubated for 48 hours at 37°C, >90% humidity, and 5% CO₂ conditions. Following the 48 hour incubation, the media was replaced with 100 μ l of phenol red free media and 10 μ l of MTT was added to each well. Plates were incubated at 37°C, >90% humidity, and 5% CO₂ conditions for 4 hours, after which the media and MTT were removed, 100 μ l of DMSO added, and incubated at 37°C for 10 minutes. The plates were then read using a ThermoFisher Scientific MultiScan GO.

Internalization of NPs. Cell lines were plated into 4-chamber well slides (154917, LAB-TEK) at optimal concentration to ensure cells would not be over confluent after 24 hours. 24 hours after cells were plated, they were treated with fluorescein (20 μ g/ml) , or fluorescein diacetate and Nile Red containing PLGA nanoparticles at 1mg/ml concentration for 1.5 hours at 37°C, >90% humidity, and 5% CO₂ conditions. After treatment, cells were washed with PBS for 5 minutes (3x) and fixed with 4% formaldehyde. Prolong Gold Antifade reagent with DAPI (P36935, Molecular Probes) was applied to

mount coverslips. Images were acquired on an Olympus Fluoview FV 1000 confocal microscope.

Specificity and Internalization of TAB004. TAB004 conjugation to pHrodo Red was performed using the pHrodo Red, succinimidyl ester (pHrodo Red, SE) kit (P36600, Molecular Probes). TAB004 conjugation to indocyanine green (ICG) was performed using the ICG Labeling Kit -NH₂ (LK31-10, Dojindo Molecular Technologies, Inc.). All conjugations were performed using manufacturer protocols. Cell lines were plated into 4-chamber well slides (154917, LAB-TEK) at optimal concentration to ensure cells would not be over confluent after 24 hours. 24 hours after cells were plated, they were treated with 5µl of TAB004-phRodo Red conjugation solution for various time points at 37°C, >90% humidity, and 5% CO₂ conditions. During the last 5 minutes of treatment, Wheat Germ Agglutinin-Alexa Fluor 488 conjugate (W11261, Molecular Probes), was added to each chamber at 5µg/ml. The cells were washed with PBS for 5 minutes (3x) and fixed with 4% formaldehyde. Prolong Gold Antifade reagent with DAPI (P36935, Molecular Probes) was applied to mount coverslips. Images were acquired on a GE Healthcare Life Sciences DeltaVision Elite Imaging microscope.

Mouse Strains. C57Bl/6 mice were purchased from Jackson Laboratory and housed at UNC Charlotte's vivarium.

Orthotopic tumor model. C57/Bl6 female mice were injected in the pancreas with 5x10⁵ KCM-Luc cells and allowed to recuperate for 7 days before any experiments were performed.

Visualization of KCM-Luc orthotopic tumors, TAB004-ICG, and TAB004 conjugated PLGA NPs with ICG. Orthotopic KCM-Luc tumor bearing C57/B16 mice were injected with 125 μ l of Redijet D-Luciferin (760504, Perkin Elmer) intraperitoneally and imaged 25 minutes later with a Perkin Elmer IVIS Spectrum. Orthotopic KCM-Luc tumor bearing C57/B16 mice were injected with 25 μ g of TAB004-ICG, 50mg/kg of NP w/ICG, or 50mg/kg of TAB004-NP w/ICG intraperitoneally and imaged at various time points with a Perkin Elmer IVIS Spectrum. Mice were euthanized at the end of imaging studies. All procedures were conducted in accordance to the Institutional Animal Care and Use Committee of UNC Charlotte.

CHAPTER 4: Development of High-Capacity Nanomaterials Through Polymer Drug Conjugates.

Forward

This chapter recognizes the contributions of: Anthony J. Fowler, Michael D. Murphy and Craig A. Ogle. *Manuscript in preparation.*

4.1 Introduction

Nanomaterials for drug delivery are rapidly evolving into a well-established technology which promises to positively impact nearly all aspects of traditional chemotherapeutic paradigms. With FDA approval of several nanomaterials, and a growing number of clinical trials, the evolution of nanoscaled systems from bench-to-bedside continues for a variety of disease states.⁶ Nanomaterials possess several interesting features not achievable with related small-molecule therapeutics. Constructed with dimensions typically less than 400 nm, NPs can; solubilize hydrophobic therapeutics to aid in delivery, systemically deliver therapeutics whilst being able to selectively permeate tissues, or be chemically modified to confer cell-selective targeting to enable differentiation of diseased tissues and healthy tissues thereby lowering associated off-target side effects.¹⁰³

The clear majority of NP formulations are prepared through the encapsulation of therapeutics during the fabrication process. While there exist a host of processes for the construction of polymeric nanomaterials, self-assembly remains one of the most popular. There are several defining characteristics of self-assembled NP formulations.¹⁰⁴ Principal among those are; 1) Morphology which defines physical interactions of NPs within the biological environment, 2) Zeta potential which governs electrostatic interactions, 3)

Surface chemistry which can be altered to confer a series of benefits, 5) NP material which greatly influences drug release and other pharmacokinetic behaviors, and 6) Drug loading – a design parameter which ultimately governs NP dosage. While most characteristics can be directly controlled, drug-loading in self-assembled NP formulation is often highly variable, with encapsulation efficiencies (EE) rarely achieving 100%, and is dependent on several interconnected variables. For the self-assembly of polymeric NP formulations there is a wide distribution in reported drug loadings. For nanoprecipitation, drug loadings are typically found within 1-2% (wt/wt) of the nanomaterial. In contrast, solvent-emulsion methodologies have consistently reported higher drug loadings, with values of 14% (wt/wt) or higher being consistently reported for a variety of therapeutic cargoes.¹⁹

Nanoprecipitation is arguably the simplest of the self-assembly techniques for the construction of polymeric NPs. This process is fast, highly reproducible, and often generates NPs with narrow PDI. In contrast to oil-water (single) or oil-water-oil (double) solvent-emulsion techniques, nanoprecipitation is a simple one-step technique easily executed under ambient conditions. Like solvent-emulsion, nanoprecipitation can adapt to a wide variety of both polymers and drugs, but is primarily limited by the drug loading capacity and EE. To address this limitation, nanoprecipitation has been recently reported for polymer-drug conjugates (PDCs) of PTX and camptothecin (CPT). To construct the PDC of both PTX and CPT, Cheng et. al.¹⁰⁵ utilized a Zn based catalyst with the hydroxyl containing PTX or CPT as initiators for the ring opening polymerization (ROP) of lactide (LA) (Fig. 4.1). Synthetically, the resulting polylactide results in the covalent incorporation of the drug at the termini as a stable ester. Construction of NPs through the use of these PDCs is a novel prodrug strategy which inexorably overcomes the drug loading limitation

of nanoprecipitation. Due to the covalent linkage of PDCs the drug loading is effectively 100% regardless of the fabrications conditions employed. Further, *in vivo* tumor reduction studies demonstrated enhanced efficacy against Lewis lung carcinoma induced in C57BL/6 mice. In a similar strategy Nicholas et. al.¹⁰⁶ demonstrated that reversible addition-fragmentation (RAFT) polymerization can be used for the construction of gemcitabine based PDCs which were then self-assembled into NPs with narrow PDI and were found to exhibit *in vitro* toxicity against several cell lines.

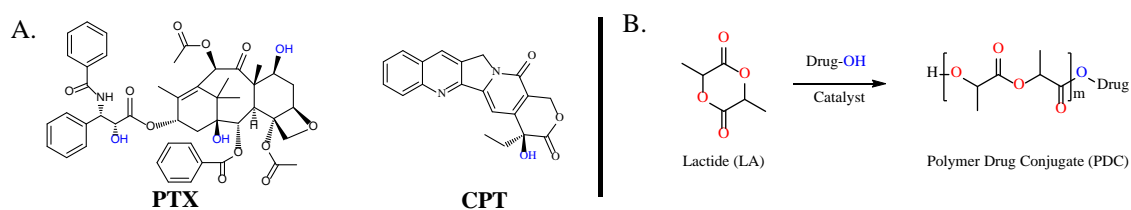


Figure 4.1. Strategy of Cheng et. al. for the preparation of drug initiated PLA. A. Structures of paclitaxel (PTX) and camptothecin (CPT). B. Drug initiated polymerization of LA.

To extend this strategy we sought to build a complementary PDC platform constructed from biocompatible and FDA approved ϵ -polycaprolactone (PCL) for the construction of NPs with high drug loadings. While many polyesters are being considered for NP formulations, the overwhelming majority are constructed with poly(lactic-co-glycolic acid) (PLGA) or polylactide (PLA). We chose PCL for several desirable characteristics, namely; ease of synthesis through a variety of synthetic routes, highly defined biocompatibility with characterized routes of biodegradation,¹⁰⁷ and compatibility with a variety of fabrication processes with the ability to easily blend using a multitude of related polyesters to aid in controlling rates of degradation. Additionally, PCL is a heterobifunctional reagent which can be chemically differentiated at either terminus. We reasoned we could exploit this to

incorporate a drug or therapeutic at either end through drug initiated polymerization of PCL, or through incorporation via the hydroxy terminated polymer (Fig. 4.2).

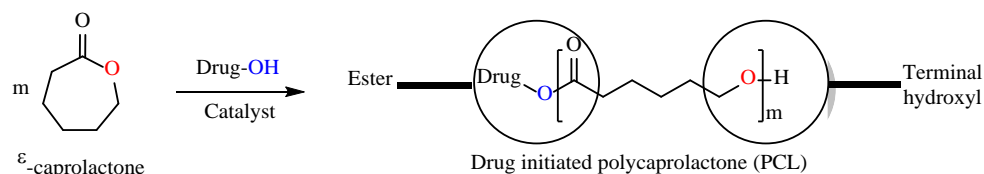


Fig. 4.2. Drug initiated polymerization of PCL.

4.2 Results and Discussion

Synthesis of cholesterol initiated PCL (4a). While there are a variety of techniques for the synthesis of polyesters, metal catalyzed ROP of lactones is the dominant methodology. Synthetically, however, metal catalyzed ROP of ϵ -caprolactone typically results in broader polymer PDI and requires the use of higher temperature (> 120 °C) which is incompatible with a variety of pharmaceutical compounds.³³ To generate PCL with narrow PDI under milder conditions we chose to utilize the methodology of Magnet et. al.¹⁰⁸ This method is relatively simple, avoids the need for a glove-box, and can be executed using simple Schlenk techniques. Briefly, the ROP of ϵ -caprolactone is catalyzed by methane sulfonic acid (MSA) in toluene using alcohol initiators at 35 °C. These polymers are thereby chemically differentiated via an ester at the point of initiation and a terminal hydroxyl group. Using these conditions, we first investigated the formation of PCL based PDCs using cholesterol as a model compound (Fig. 5.3). Cholesterol has a single hydroxyl for initiation, is hydrophobic in nature, and has similar structural characteristics to a variety of therapeutics. Further, because the reported rate of initiation is rapid, we reasoned that cholesterol would hold-up to the presences of a strong acid such as MSA. Due to our goal

of preparing NP with high drug loadings, we sought to develop PCL based PDC of cholesterol ~ 16% (wt/wt).

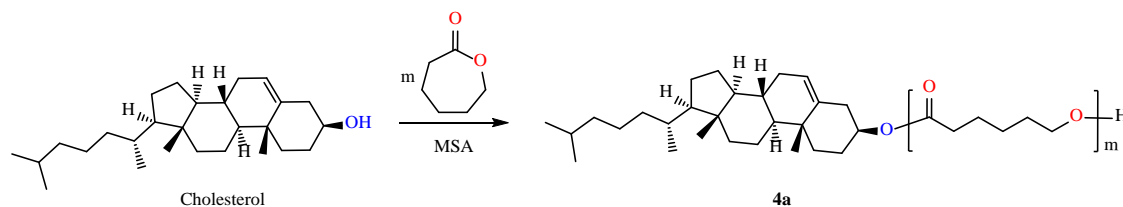


Figure 4.3. Cholesterol initiated polymerization of PCL.

Accordingly, using the prescribed conditions, we prepared PDC **4a** with the polymeric segment having number averages (M_N) of 17.5 repeat units per cholesterol in quantitative yield (determined by ^1H NMR using end-group analysis). PDC **4a** was prepared on a multigram scale in high yields and high purity.

Synthesis of terminal functionalized PCL. To chemically differentiate PCL we wanted to incorporate a pharmaceutical through incorporation at the terminal hydroxyl of the PCL polymer. PTX was chosen as a model compound due to its wide application in chemotherapeutics, and its multiple references demonstrating prodrug formation through both ester^{109,110} and carbonate¹¹¹⁻¹¹³ formation. We chose to conjugate PTX to PCL through a carbonate linkage as alkyl carbonate prodrugs exhibit high levels of stability under physiological conditions, yet are substrates for enzymatic cleavage.¹¹⁴ As a model polymer, we prepared a benzyl alcohol (BzOH) initiated PCL_{2K} polymer (**4b**). Successful incorporation of PTX onto the PCL_{2K} polymer would result in a PDC having a PTX incorporation of 29% (wt/wt). Installation of PTX was achieved using the scheme outlined in figure 4.4. Activation of the terminal hydroxyl group was achieved using 1,1'-carbonyldiimidazole (CDI) which results in the incorporation of a reactive *o*-acylimidazole

(4c). The clean *o*-acylimidazole of 4c can further be derivatized directly with any amine containing substrate to prepare a urethane derivative, or can be further activated to enable the formation of a carbonate – a necessity for the introduction of PTX. To introduce PTX, we activated the *o*-acylimidazole with MeI to generate the Me-salt (4d) of the 4c thereby increasing its electrophilicity. Treatment of 4d with PTX in the presence of triethylamine (TEA) resulted in the quantitative incorporation of PTX onto the PCL terminus via a carbonate linkage. The PCL-PTX conjugate was easily purified of liberated *N*-methylimidazole using a simple aqueous wash.

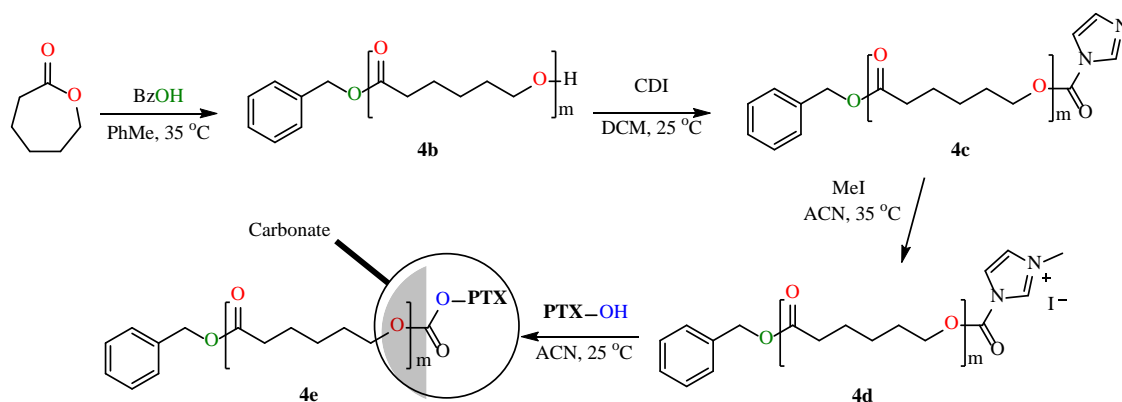


Figure 4.4. Synthetic route for the incorporation PTX through functionalization of the terminal OH of BzOH initiated PCL.

PTX is complicated by the presence of three reactive hydroxyls of differing chemical reactivity (Fig. 4.5) which is expected to result in low regioselectivity. For our purposes, this would result in a polymer of differing physiochemical properties, but would still be expected to result in a PDC capable of forming biologically active NP formulations. Acylation of the hydroxyls of C2' and C7 of PTX was expected to occur without complete regioselectivity. This observation would be in-line with previous reports of the acylation

of PTX with small molecules. Due to increased steric demand for the acylation of the hydroxyl of C1 this product was, as expected, not observed.

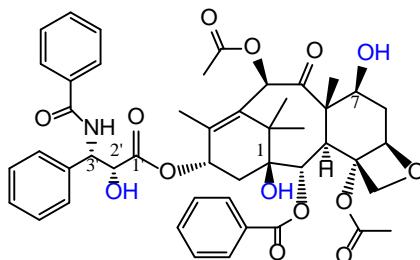


Figure 4.5. Paclitaxel (PTX). Numbering of PTX adapted from Beutler et. al.

To determine the regioselectivity of the reaction between PTX and **4d**, we analyzed product formation by ^1H NMR and compared that to PTX (Fig. **4.6**). The chemical shift of the C2'-H of compound **4e** had shifted downfield relative to that of PTX (4.69 to 5.37), whereas the chemical shift of the C7-H was nearly identical for PTX (4.28) and **4e** (4.30). Additionally, the resonances for both the C7-OH and C1-OH were identified in **4e** and demonstrated no significant change relative to PTX. Based on these results we have identified the reaction of **4d** and PTX to be nearly 100% regioselective for acylation of the C2'-OH.

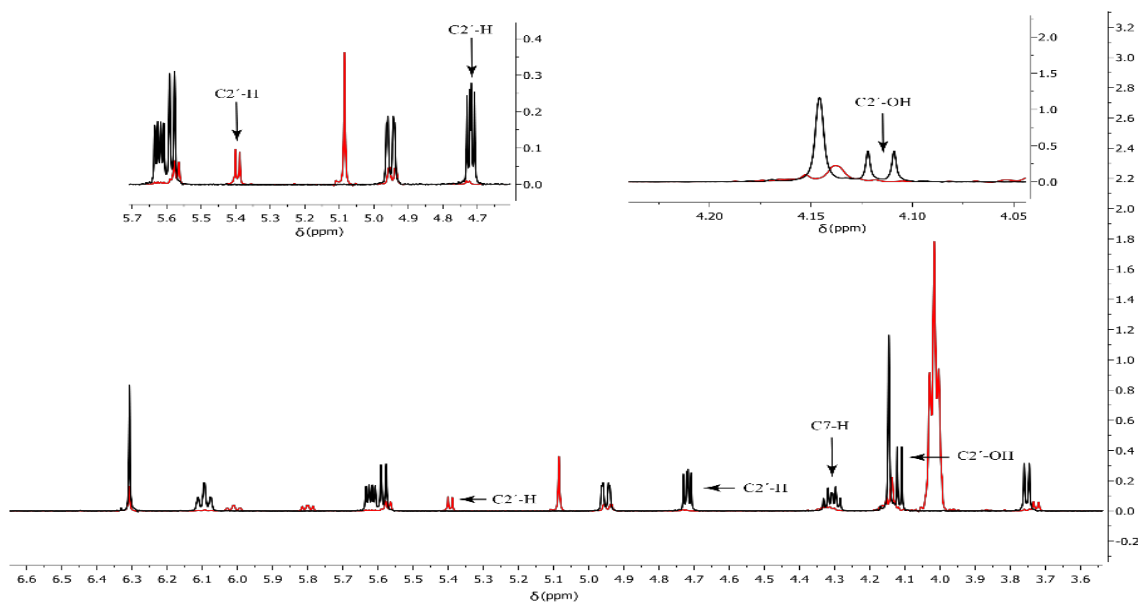


Figure 4.6. ^1H NMR (CD_3CN , 500 MHz) Characterization of PCL PTX Conjugate. PCL-PTX conjugate (**4e**) red. Free PTX black.

To further characterize the conjugation between PTX and **4d** we chose to utilize Diffusion Ordered Spectroscopy (DOSY). This technique is convenient, non-destructive, and can be performed under relatively mild conditions which will not degrade the compound investigated. Looking at the DOSY spectrum of **4d** we compared the resonances of C13-H of free PTX and **4d** to that of the polymer resonance at 4.0 ppm. Of the two C13-H resonances, only that of **4d** diffused at the same level as that of the polymer resonance. By comparison, the free C13-H resonance diffused at a considerably different level. The structural analysis of the ^1H NMR coupled with the DOSY spectrum of **4d** clearly indicate the connection of PTX to the terminal hydroxyl of PCL through the C2'-OH.

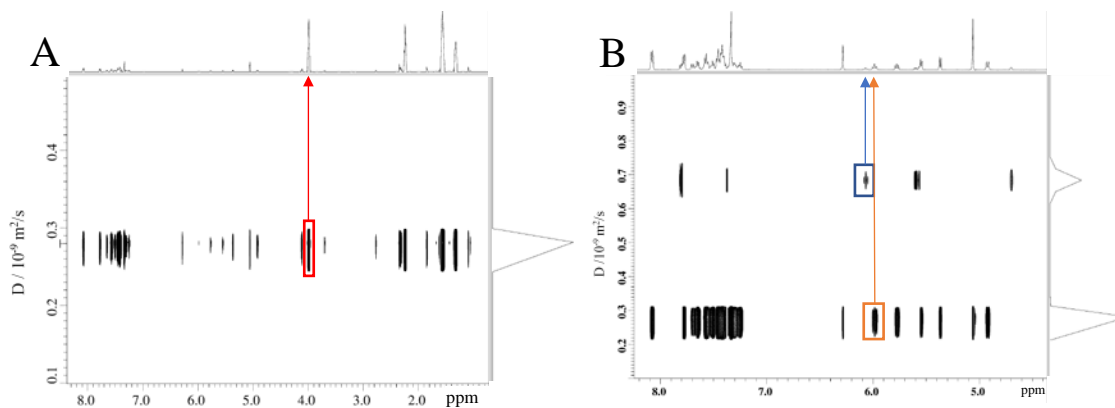


Figure 4.7. DQSY (CD_3CN , 500 MHz) spectrum of PCL-PTX conjugate (**4e**). A. PCL resonance at 4.0 ppm shown in red. B. Resonance of C2'-H of free PTX (blue) and of PCL-PTX (orange).

Preparation of Cholesterol-PCL and PTX-PCL NPs. To screen the ability for the prepared PDCs to form NPs we utilized nanoprecipitation (Fig. **4.8**) according to conditions previously described in chapter 3 and chapter 5. Polymers were dissolved into acetone at (10 mg/ml) and added dropwise to a 1% PVA (aq.) solution under vigorous stirring. Under these conditions each of the PDCs were successful in the formation of NPs with relatively narrow PDI. For the cholesterol PDC, NPs of approximately 100 nm were readily prepared and found to possess a negative zeta potential (-12 mV). In contrast, the PDC of PTX demonstrated the formation of NPs with a diameter of 140 nm and a near neutral zeta potential of (1.4 mV). While the NP formation is consistent with previous reports for the construction of NPs from PDCs, we were relatively surprised by the difference in the zeta potentials, but we believe this is due to the formation of the carboxylic acids during the preparation of the cholesterol PTX-conjugate which confers the negative zeta potential. While the NP formation was expected, we were surprised to see minimal aggregation noting that we did not incorporate any pegylation which is typically needed to

maintain colloidal stability through minimization of aggregation. Future studies investigating the incorporation of pegylation and the effects of different drug loadings is underway.

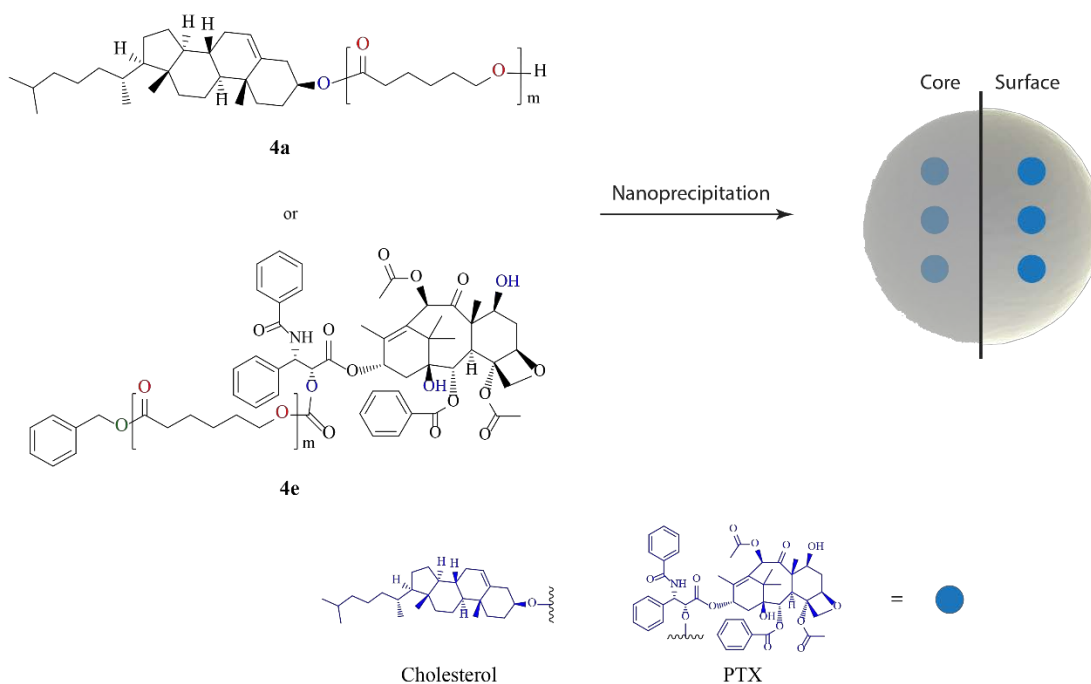


Figure 4.8. Nanoprecipitation of **4a** or **4e** resulting in high capacity NPs. Both PTX and cholesterol are expected to distribute evenly in both the NP core and surface.

4.3 Conclusion

Herein we have demonstrated the facile preparation of polymer drug conjugates of PCL and the application thereof in the preparation of NPs. Using cholesterol as a model compound for therapeutics, we have demonstrated that drugs of appropriate composition can successfully initiate PCL polymerization using metal-free catalysis to prepare multi-gram quantities of the resulting PDC. Further, we have also demonstrated the incorporation

of a shelf-stable and reactive *o*-acylimidazolium salt onto the termini of PCL can be successfully used to covalently conjugate PTX to PCL. Particularly noteworthy was the observed regiochemistry of the acylation of PTX. While we did not expect complete regioselectivity between the C2'-OH and C7-OH, we were surprised to note the nearly complete regioselectivity for the C2'-OH. PTX is indicative of a variety of complex therapeutics, and this result suggests we can extend this method to a variety of molecular architectures. We have successfully shown these PDCs can be nanoprecipitated to prepare NPs. These NPs have the benefit of being prepared from FDA approved materials, have relatively narrow particle size distributions, and possess nearly 100% drug loading. Further, by simply varying the drug-to-polymer ratio, the effective drug loading can be easily varied. By combining these two methods, we reason we will be able to extend this process for the fabrication of asymmetrically functionalized PCL resulting in the incorporation of different drugs to generate effective combo therapeutics. Additionally, these PDCs could be utilized for the encapsulation of therapeutics which could provide additional benefits by providing NPs having a variety of different release profiles.

4.4 Materials and Methods.

All chemical reagents used for the study were of analytical grade and above. ϵ -Caprolactone, benzyl alcohol (BzOH), cholesterol, Poly(vinyl alcohol) MW 6000 (PVA) (80 mol% hydrolyzed), 1,1'-carbonyldiimidazole (CDI), methane sulfonic acid (MSA), and methyl iodide (MeI) was purchased from Sigma Aldrich (St. Louis, MO). Paclitaxel was purchased from Matrix Scientific (Columbia, SC). ^1H and ^{13}C NMR was obtained on a JEOL ECX-500 MHz spectrophotometer and referenced to the solvent. Particle size,

polydispersity index (PDI), along with zeta potential were performed using a Zetasizer Nano (Malvern Instruments).

Synthesis of Cholesterol-PCL_{2K} (4a). Cholesterol-PCL_{2K} was prepared according to the procedure of Magnet et. al.¹⁰⁸ Briefly; 1.94 ml (35 mmol, 17.5 eq.) of ϵ -Caprolactone was dissolved into 40 ml of anhydrous toluene. To this was added (0.77 g, 2 eq.) of cholesterol and 0.13 ml (2 mmol) of methanesulfonic acid under rapid stirring. The solution was stirred for 90 min at 35 C. Following this, the polymerization was quenched by the addition of approximately 0.5 g of Amberlyst® A21 resin to eliminate the catalyst. The polymer was then precipitated in anhydrous pentane and dried under vacuum. The precipitated was isolated as a white solid (2.5 g, 92%).

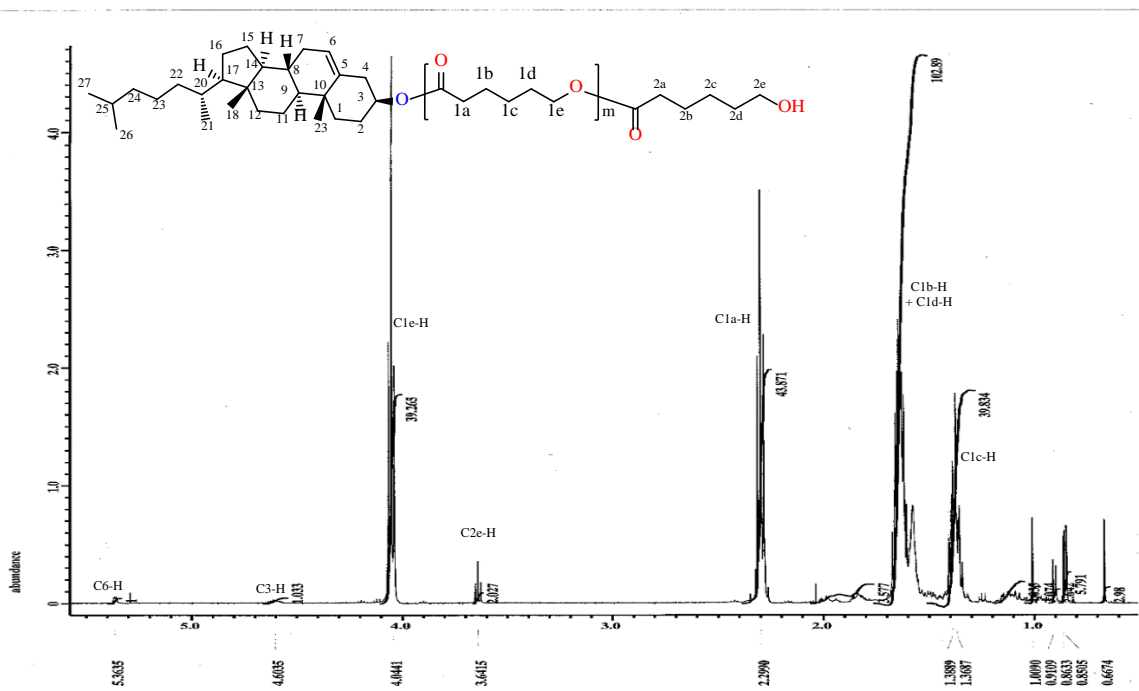


Figure 4.9. ¹H NMR (CDCl₃, 500 MHz) **4a** 0-5.6 ppm.

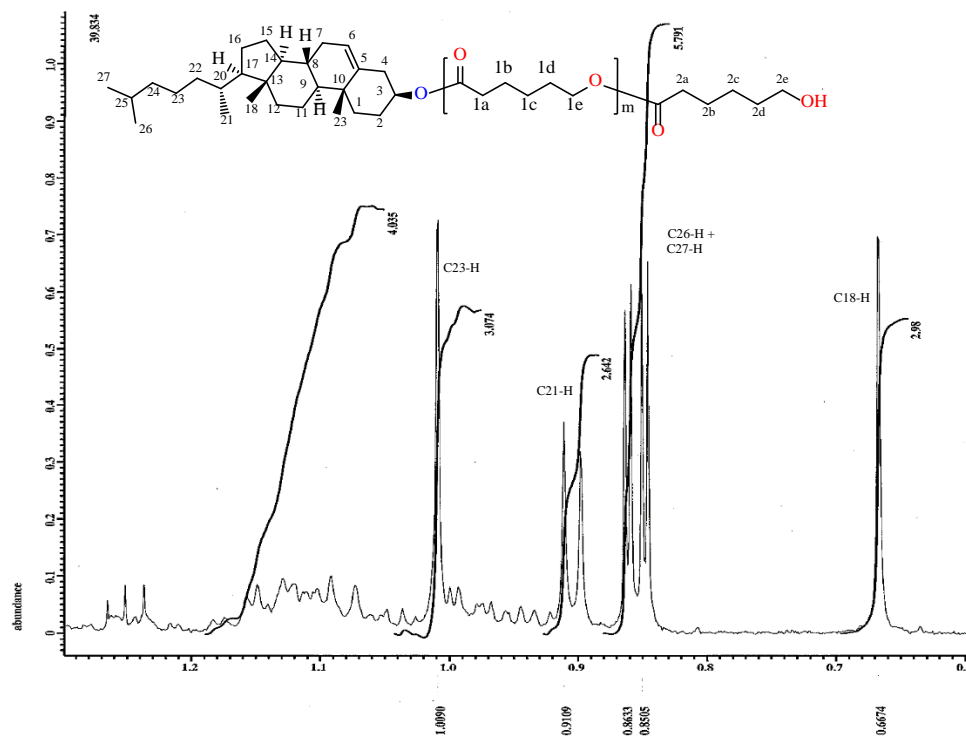


Figure. 4.10. ^1H NMR (CDCl_3 , 500 MHz) **4a** 0.6-1.3 ppm.

Synthesis of (4b). 1.94 ml (35 mmol, 17.5 eq.) of ϵ -Caprolactone was dissolved into 40 ml of anhydrous toluene. To this was added (.22 g, 2 eq.) of BzOH and 0.13 ml (2 mmol) of methanesulfonic acid under rapid stirring. The solution was stirred for 90 min at 35 C. Following this, the polymerization was quenched by the addition of approximately 0.5 g of Amberlyst® A21 resin to eliminate the catalyst. The polymer was then precipitated in anhydrous pentane and dried under vacuum. The precipitated was isolated as a white solid (1.9 g, 90%).

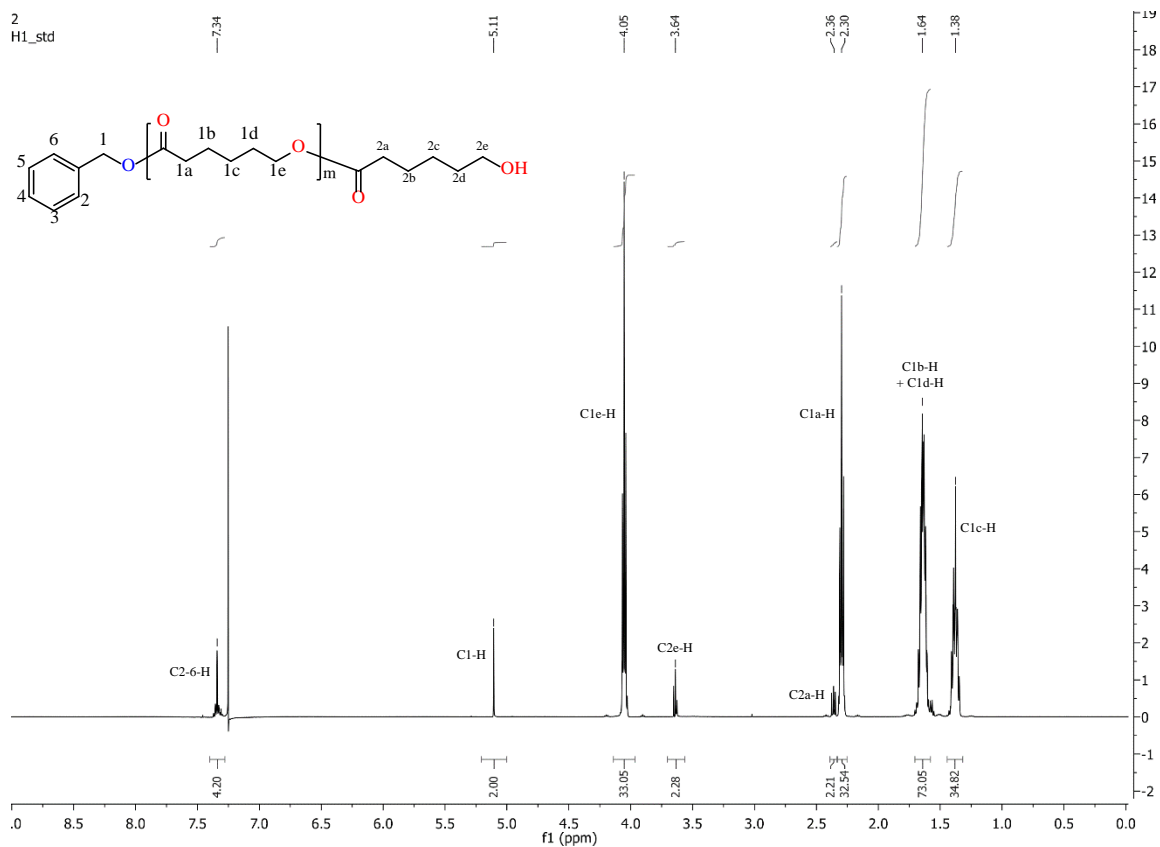


Figure 4.11. ¹H NMR (CDCl₃, 500 MHz) 4b.

Synthesis of (4c). 200 mg (.095 mmol, 1 eq.) of BzO-PCL_{2K} was dissolved into 5 ml of anhydrous DCM. To this was added 1.7 mg (.105 mmol, 1.1 eq.) of CDI in one portion. The solution was stirred for 30 min at room temperature. Following this, the reaction was diluted with 5 ml of DCM then extracted with DI H₂O (5 x 10 ml). The organics were collected, dried over MgSO₄, and the solvent removed under reduced pressure. The product was isolated as a white solid (0.2 g, 95%).

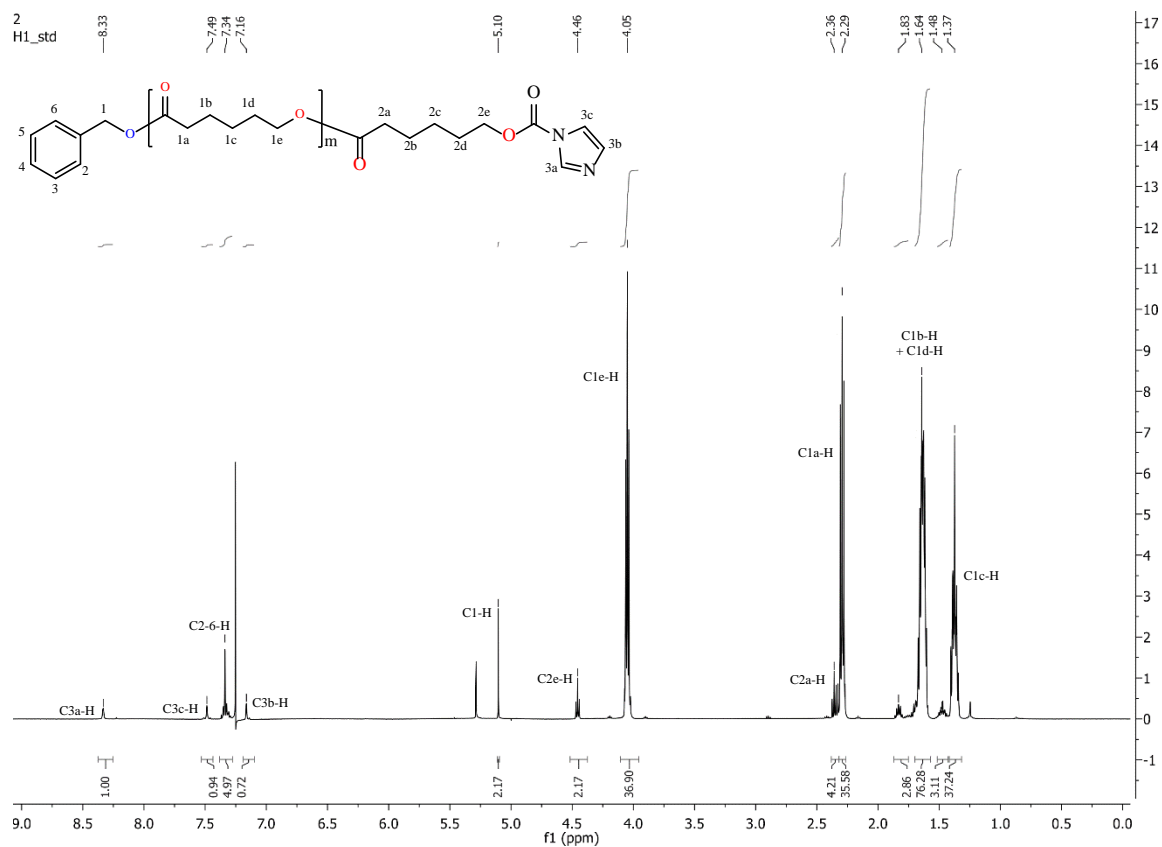


Figure 4.12. ¹H NMR (CDCl₃, 500 MHz) **4c**.

Synthesis of (4d). 100 mg (.045 mmol) of Im-PCL_{2K} was dissolved into 3 ml of anhydrous ACN in a screwcap vial. To this was added 28 μ l (.45 mmol, 10 eq) of MeI. The solution was left to sit at 25 C for 24 hrs. Following this, volatile organics were removed under reduced pressure. The product was isolated as a lightly yellowed solid in quantitative yield.

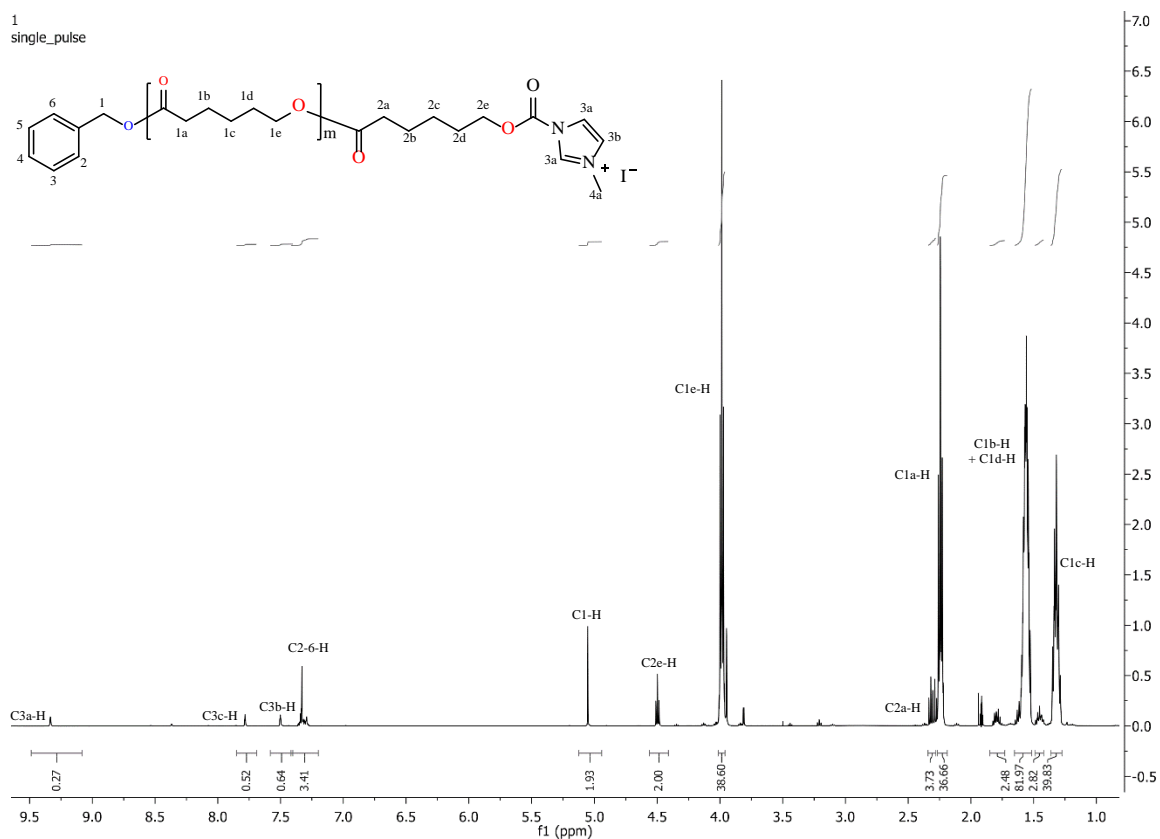


Figure 4.13. ¹H NMR (CD₃CN, 500 MHz) **4d**.

Synthesis of (4e). 100 mg (.043 mmol, 1 equiv) of MeIm-PCL_{2K} was dissolved into 3 ml of anhydrous ACN in a screwcap vial. To this was added 40 mg (1.05 mmol, 1eq) of PTX and 12.5 μl (.09 mmol, 2 eq.) of TEA. The resulting solution was left to sit overnight at room temperature. Following this the organics were diluted into 10 ml of EtOAc and extracted sequentially with 5% citric acid (5 × 10 ml), sat. NaHCO₃ (aq) (3 × 10 ml), and sat. NaCl (aq) (3 × 10 ml). The organics were dried over MgSO₄, concentrated under reduced pressure, then left overnight under high vacuum. The product was isolated as a white solid (129 mg, 94%) as a white solid.

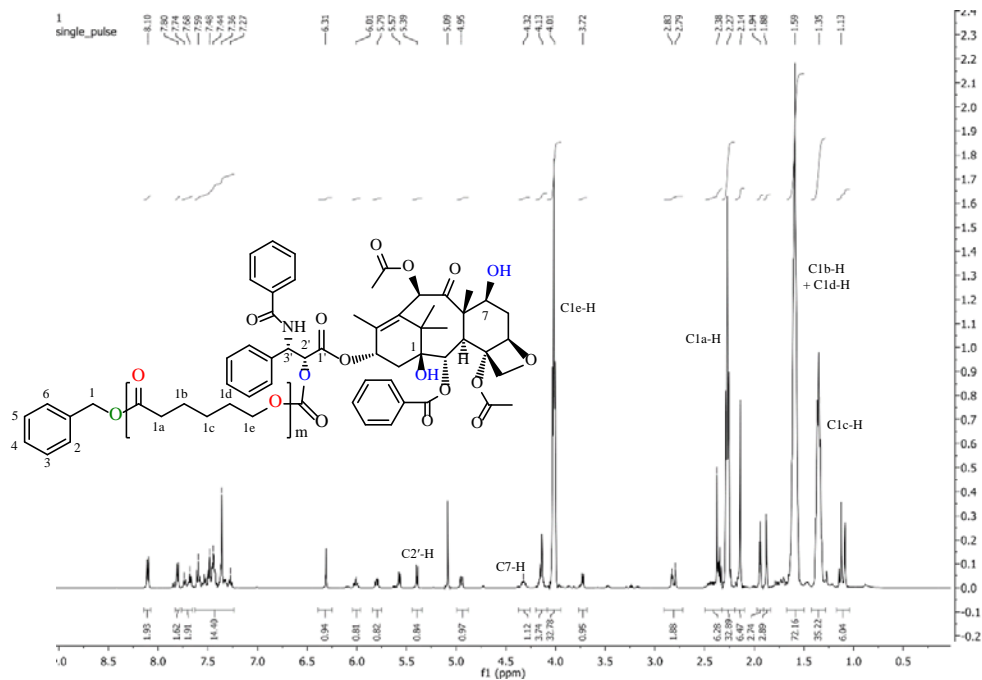


Figure 4.14. ¹H NMR (CD₃CN, 500 MHz) **4e**.

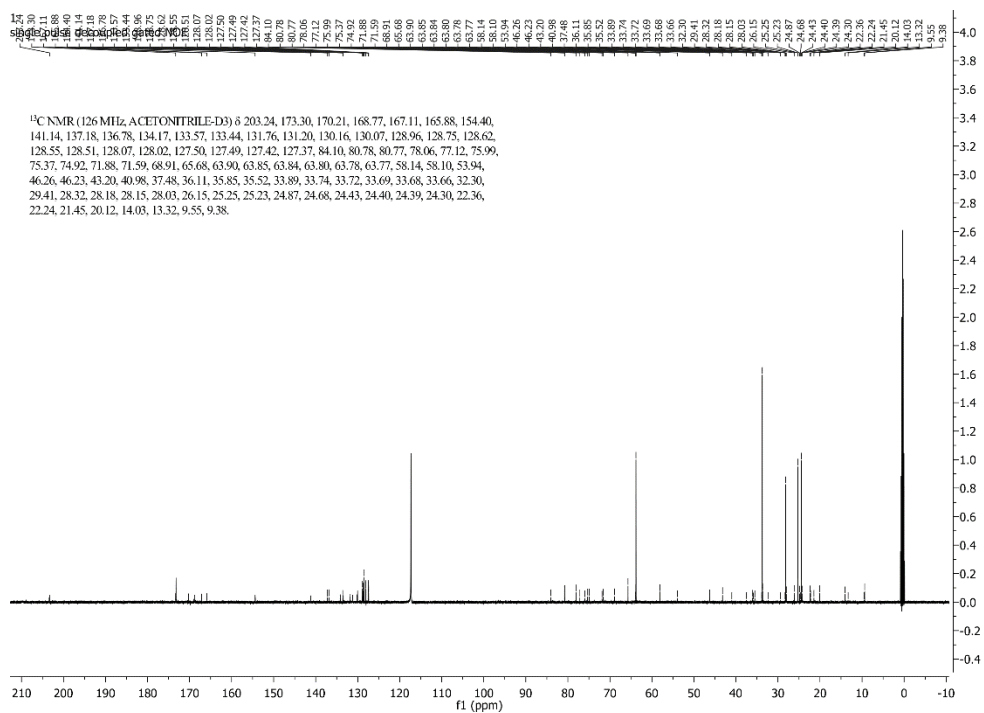


Figure 4.15. ¹³C NMR (CD₃CN, 500 MHz) **4e**.

Preparation of high capacity NPs using cholesterol-PCL and PTX-PCL PDCs. High capacity nanoparticles were prepared by the nanoprecipitation method. Briefly; 100 mg of the PDC was dissolved into 10 ml of acetone. This solution was then added dropwise via syringe into a stirred solution of 1% PVA (50 ml) at a rate of 90 ml/hr controlled using a syringe pump. The resulting colloidal suspension was then transferred to a 100 ml round-bottom flask, and the acetone removed under reduced pressure using a rotary evaporator. NPs were then purified by centrifugation following precipitating of the particles with sat. NaCl (aq). This process was repeated three times. The resulting NP pellet was then resuspended into sterile filtered 18 Ω water (15 ml) and dialyzed to remove the salt. These particles were then analyzed by DLS.

Table 4.1. Characterization of high capacity nanomaterials

Nanomaterial	HD (nm)	PDI	ZP (ζ)	(wt/wt) % drug
Cholesterol-PCL _{2K} NPs	140	.245	-12.8	16
PCL _{2K} -PTX NPs	103	.091	1.39	29.9

HD = Hydrodynamic Diameter, PDI = Polydispersity Index, ZP = Zeta Potential.

CHAPTER 5: Treatment of Bovine Mammary Mastitis with Polyester Nanomaterials.

Forward

This chapter recognizes the contributions of: *Bayer Animal Health, Germany*. All biological studies were performed by Bayer Animal Health according to prescribed therapeutic paradigms. Results of these studies have been reproduced here.

5.1 Introduction

The use of nanotechnology in drug delivery and diagnostics is on the rise. With nanotechnology in cancer chemotherapy already FDA approved,⁶ nanomaterials are set to provide a boon in technological advancements for a variety of biomedical applications. While strongly entrenched in the field of cancer chemotherapeutics, the use of nanotechnology for the treatment of infectious disease is comparatively nascent.^{115, 116} The use of nanotechnology in the treatment of infectious disease has many potential benefits, particularly these efforts may: 1) improve the drug delivery by selectively targeting bacteria,^{117, 118} 2) overwhelm bacterial response through increased localized drug concentrations, 3) and improve therapeutic efficacy through sustained local delivery of combination therapeutics.¹¹⁹

Staphylococcus aureus (*S. aureus*) is the major causative agent of clinical and subclinical intramammary infections (IMI) in bovine mastitis responsible for the largest economical losses to the dairy industry.¹²⁰ Estimates of the financial impact on the American dairy industry suggest that bovine mastitis is responsible for nearly US\$2 billion annually in losses due to lost milk production, herd productivity, and animal losses.¹²¹

Infections by *S. aureus* are problematic at all stages of the milk production chain. To date, the principle treatment for *S. aureus* infections in bovine mastitis is the intramammary administration of antibiotics (Abs).¹²² There is a wide variety of approved curative Abs available for the treatment of bovine mastitis, however, this treatment paradigm has a relatively low cure rate resulting in persistence of infection which inexorably leads to chronic infection. With low cure rates, and high financial impact, a variety of new therapies have been investigated.

Two principle strategies for the treatment of IMI involve the use of vaccination against *S. aureus*, and the identification of new and more powerful Abs. Two multivalent vaccines, Lysigin® (Boehringer Ingelheim Vetmedica Inc.)¹²³ and Starvac® (Hipra)¹²⁴ for the treatment of *S. aureus* are commercially available. While the use of vaccines against *S. aureus* have generally shown reduced clinical symptoms, this strategy is not yet sufficient as a sole treatment.¹²⁵ The use of Abs is problematic against *S. aureus* infections. Firstly, *S. aureus* is known to exhibit susceptibility to a wide variety of medications. For example, semisynthetic penicillins such as such as oxacillin and nafcillin have a long history in the treatment of *S. aureus* infections in both humans and animals and are effective agents where resistance is not a factor. However, Abs often fail to treat *S. aureus* infections *in vivo* resulting in chronic infection. This factor may be due to adaptive bacterial responses enabling survival within the host cell, or in acquired antimicrobial resistance (AMR) through mutation or chronic ineffective drug exposure. Further, low cellular penetrance of Abs resulting in minimal cellular accumulation of drugs can render the therapy incapable of fully eradicating the infection. While the exact mode of bacterial persistence in bovine mastitis is not fully understood, recent studies suggest that this is likely a confluence of

several of these factors. In a 2014 study, antimicrobial resistant mastitis was detected in nearly 60% of the bovines studied, with *S. aureus* accounting for 44% and methicillin resistant *S. aureus* nearly 5% of the resistant bacteria detected.¹²⁶ Studies have confirmed that *S. aureus* is able to invade (through cell surface proteins such as protein A and fibronectin)¹²⁷ and persist (using a host of secreted virulence factors)¹²⁸ in bovine mammary cells.

Knowledge of these key physiological factors are leading to new avenues for the targeting of pathogenic infections of bovine IMI. In this present work we sought to develop a nanoparticle platform for the intramammary delivery of nafcillin. We reasoned that nanoparticles could be rendered capable of overcoming several of the key physiological barriers in the treatments of IMI using the following design criteria. First, nanomaterials could be used for the selective treatment of bacterial infections through the incorporation of a targeting moiety. While the incorporation of a species-specific targeting agent (e.g. antibodies or aptamers) could - in theory - result in a highly-specific therapeutic, its incorporation would needlessly limit the scope of the platform and greatly increase the financial burden of the final product. Because bovine IMI can consist of multiple gram-positive (*S. aureus*) and gram-negative bacteria (*Escherichia coli* [*E. coli*])¹²⁹ we chose to target the negatively charged bacterial cell wall through electrostatic interactions via incorporation of constitutively charged quaternary ammonium salts. This modality for targeting can be easily applied and is highly cost effective. Further, this will provide a broad therapeutic platform against a variety of pathogenic disease. Thus, through the incorporation of a cationic surface, NPs could be rendered that adhere to bacterial cell walls. Additionally, cationic nanomaterials have been shown to have improved cellular

uptake in eukaryotic cells, thereby this platform could aid in the improved intracellular accumulation of the therapeutic cargo.¹³⁰ Secondly, we chose polyester nanomaterials for its demonstrated ability to encapsulate a variety of therapeutics. For this study we opted for Poly(Lactide-co-Glycolide) (PLGA) due to its biodegradability and biocompatibility and its use in therapeutic devices has already been approved. Applications of PLGA in the construction of nanomaterials is growing rapidly and the use of PLGA in the encapsulation of nafcillin has previously been demonstrated for the treatment of osteomyelitis.

5.2 Results and Discussion

Design and Characterization of Negatively Charged Nanoparticles Loaded with Nafcillin. Nanoparticles composed of PLGA and laden with nafcillin were prepared using a single oil-in-water emulsion method previously described. Using this method we were able to produce nanoparticles with structural characteristics similar to those reported previously. Specifically, we prepared NPs with a negative zeta potential (-20 mV) and a hydrodynamic diameters (HD) of 121 nm with an apparent drug loading of approximately 7% (wt/wt). Due to the free carboxyl of the PLGA matrix, NPs composed thereof are expected to exhibit a negative zeta potential (ζ). This value is expected to further decrease due to nafcillin's pKa of 2.7 and its incorporation into the NP matrix and due to surface bound compound. Results of previous studies indicate a major "burst-release" of nafcillin with nearly 42-47% of drug released within the first 48 hrs. of study. The "burst-release" is attributed to the simple diffusion of the nafcillin facilitated by the proximity of nafcillin to the surface of the NP. The remainder of the material was shown to release slowly over

35-40 day either due to nafcillin being “encapsulated” or merely buried deeper within the NP matrix. We reasoned that surface bound nafcillin could be removed through ionic exchange by treatment with a high concentration of an aqueous salt solution. To test this theory we treated 100 mg of this nanomaterial with increasing amounts of sat. NaCl (aq). Addition of this solution to the NP results in the rapid precipitation of the NPs from solution which can then be conveniently removed through centrifugation. Upon resuspension with distilled (DI) H₂O the nanomaterial is recovered. Under these conditions we could remove a majority of the nafcillin as confirmed by ¹H NMR. This could be due to two reasons, these are; 1) The addition of sat. NaCl (aq) results in degradation of the NP thus liberating the nafcillin, or 2) The bulk of the nafcillin is not encapsulated within the NP core. We analyzed the NPs recovered from the treatment with sat. NaCl (aq) by DLS and these exhibited no apparent loss of NP integrity with only a slight increase in HD likely due to particle aggregation. Further, we could recover > 95% of the sample following precipitation. Based on these results we believe the majority of the nafcillin is not encapsulated as previously reported.

Table 5.1. Characterization of (-) Nafcillin NPs and (+) Nafcillin NPs

Preparation Method	Nanomaterial	Cargo Loading (mg)	Amount Encapsulated*	EE (%)
Oil-in-water	(-) Nafcillin NPs	330	66	20
Nanoprecipitation	(+) Nafcillin NPs	5	1.6	32

*EE = Encapsulation Efficiency. * Determined by ¹H NMR.*

Table 5.2. Structural Properties of PTX, FL(OAC)₂, NR, and ICG Nanomaterials

Nanomaterial	HD (nm)	PDI	ZP (ζ)
(-) Nafcillin NPs	121	.11	-20
(+) Nafcillin NPs	151	.099	+10

HD = Hydrodynamic Diameter, PDI = Polydispersity Index, ZP = Zeta Potential.

Design and Characterization of Positively Charged Nanoparticles Loaded with Nafcillin. To generate cationic NPs we chose to use the nanoprecipitation method used previously (see chapter 3). To encapsulate nafcillin using nanoprecipitation we first rendered nafcillin neutral through acidification of the sodium salt. This serves to make the nafcillin hydrophobic with minimal solubility in an aqueous environment. This characteristic is ideal for nanoprecipitation as it results in improved compound encapsulation within the hydrophobic core of the NP matrix. Using this method NPs were prepared with HD of 151 nm (see table 5.1 and 5.2) with a nafcillin loading of \approx 1.6% (wt/wt). NPs were rendered cationic using a strategy similar to previous reports.¹³¹ Incubation of the resulting particles with hexadecyltrimethylammonium bromide (CTAB) for 24 hrs. resulted in NPs with positive zeta potentials of approximately +10 mV. The encapsulation of the nafcillin was determined by ¹H NMR following precipitation of the NPs with sat. NaCl (aq) as previously described under neutral conditions.

Treatment of Bovine Mastitis using Negatively and Positively Charged Nanoparticles.

Using the modified chronic mouse model of mastitis (MCM³) NPs were assessed for efficacy against free nafcillin and the current front-line treatment pirlimycin. NPs were prepared using a hydrogel based carrier which is in line with current industry standard practices. The first NPs screened in this study were the negatively charged NPs with 7%

nafcillin loading (wt/wt). Under these conditions, the nafcillin loaded NPs demonstrated attenuated activity against *S. aureus in vivo* compared to free nafcillin (Fig. 5.1). This reduction in activity of the nafcillin was not necessarily expected but may be attributed to several factors. Firstly, the treatment of *S. aureus* is multifaceted and occurs in highly complex milieu of cellular environments consisting of the following; Intracellular and extracellular infections, infections either lacking or involving complex biofilm formation, and both acute and chronic infections at all stages of milk production. During treatment, nafcillin is expected to freely distribute under first order kinetics and diffuse rapidly within the cellular space. In contrast, NPs loaded with nafcillin have been shown to liberate nafcillin in a biphasic system with an initial burst with 42 – 47 % liberated within the first 48 hrs. and the remainder slowly released over 35 – 40 days.¹³² The initial burst of the NPs is well within the time-frame of the 68 hr. therapeutic exposure of this study. Secondly, eukaryotic uptake of nanomaterials is generally attenuated for NPs with a negative zeta potential and may not have been maximized during the therapeutic exposure. Due to these results we reasoned that cationic NPs could serve to mitigate these limitations of these NPs.

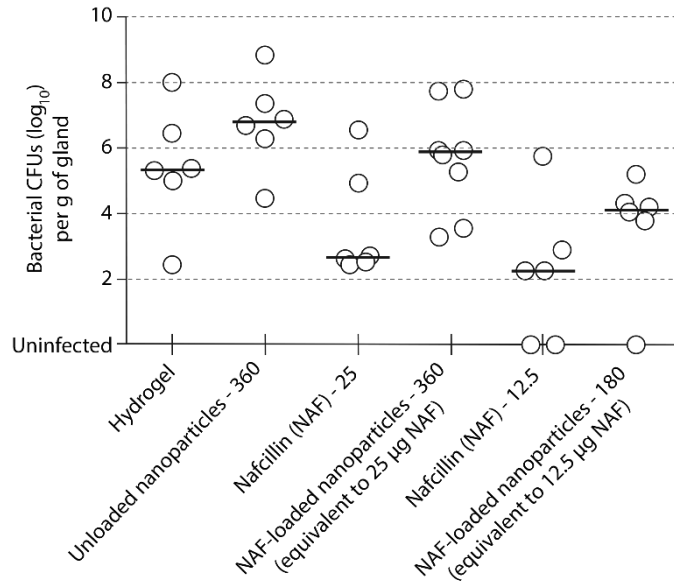


Figure 5.1. Treatment of mastitis using MCMMM with (-) Nafcillin NPs.

NPs with cationic surfaces were screened against both free nafcillin and pirlimycin. Using the same parameters as above, mice were treated with cationic NPs, free nafcillin, and pirlimycin at the indicated dosages (Fig. 5.2). Results of this study indicate there is a dramatic increase in efficacy for the treatment of IMI with nafcillin loaded in cationic NPs with 4/6 animal being fully cleared of all infection compared to 0/8 animals rendered uninfected by free nafcillin. We reason these results are likely due to two factors, these are; 1) improved cellular uptake of the cationic NPs making this treatment more capable of fully eradicating bacteria responsible for intracellular infection within mammary cells not treatable with free nafcillin, or 2) NP localization to bacterial infection through electrostatic interaction of the cationic particles with bacterial cells thereby increasing localized drug concentration relative to the pathogen. Further, cationic NPs were found to be comparable to pirlimycin which resulted in 5/7 uninfected animals indicating this NP platform could

be a potential replacement for currently used therapeutics. While the above proposed models require further studies, the results suggest further investigation is warranted.

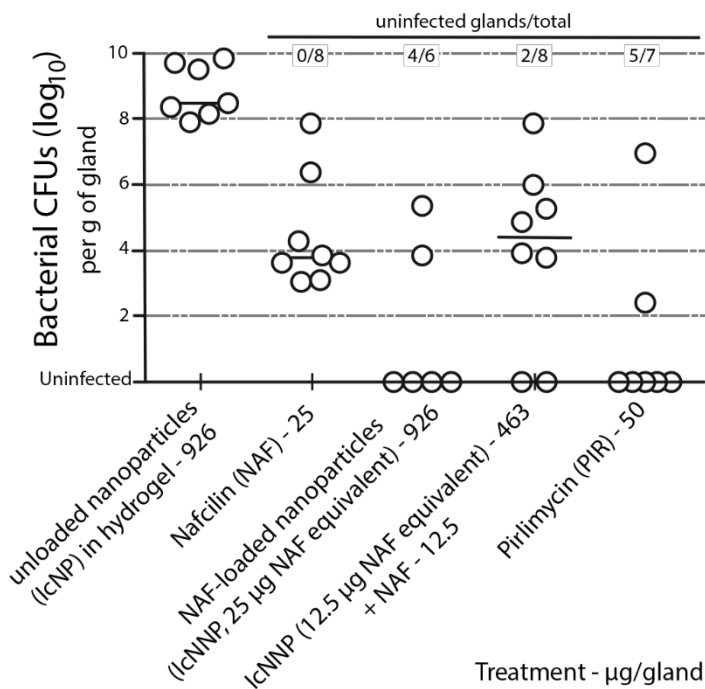


Figure 5.2. Treatment of mastitis using MCMMM with (+) Nafcillin NPs.

5.3 Summary

In summary, we have developed a platform for the effective delivery of nafcillin using PLGA NPs and explored its applicability *in vivo* using the modified chronic mouse model of mastitis (MCMMM). We compared two PLGA NP formulations prepared by different methods. In the first, we prepared NPs using single oil-water solvent emulsion method. NPs with 7% (wt/wt) were prepared but failed to demonstrate efficacy in the MCMMM. Further investigation of the NP formulation we have shown that much of the nafcillin was likely not encapsulated but rather complexed on the surface of the NP. Using

nanoprecipitation, we prepared a second formulation having 2% (wt/wt) nafcillin and a cationic surface. In the MCMMM these cationic NPs demonstrated increased efficacy against nafcillin, and compared favorably with the front-line medication pirlimycin. We reasoned these results were likely due to improved cellular uptake within the mammary cells, and thereby were more effective and eradicating bacteria within the intracellular environment. Due to the major impact of bovine mammary mastitis on the dairy industry worldwide, we reason that these formulations can have major impact on the delivery of therapeutics. Further, using the MCMMM as a model of other *S. aureus* related infections, we believe these results will translate into therapeutic models of major importance to human health.

5.4 Materials and Methods.

All chemical reagents use for the study were of analytical grade and above. Poly(DL-lactide-co-glycolide) Mw 20,000 (PLGA) (50:50) PolySciences, Inc. (Warrington, PA). Poly(vinyl alcohol) MW 6000 (PVA) (80 mol% hydrolyzed), Dextrose was purchased from Sigma Aldrich (St. Louis, MO). Nafcillin was purchased from Matrix Scientific (Columbia, SC). Determination of NP size and polydispersity. Particle size, polydispersity index (PDI), along with zeta potential were performed using a Zeta Pals, Brookhaven Instruments Co. (Holtsville, NY). ¹H and ¹³C NMR was obtained on a JEOL ECX-500 MHz spectrophotometer and referenced to the solvent. Particle size, polydispersity index (PDI), along with zeta potential were performed using a Zetasizer Nano (Malvern Instruments).

Synthesis of Negatively Charged Nafcillin Loaded PLGA Nanoparticles. NPs composed of PLGA (50:50) were prepared by a single oil-in-water solvent emulsion method previously described with minor modification. PVA was used a surfactant to aid in maintaining colloidal dispersity of the particle solutions. NPs with and without nafcillin were prepared by this method. Briefly, 1 g of PLGA was dissolved into 30 ml of a DCM and acetone mixture (8:2) in a glass beaker. 330 mg of Nafcillin was dissolved into 30 ml of acetone with the aid of approximately 54 drops of water to assist in complete dissolution of the nafcillin. The acetone solution containing the nafcillin was added dropwise to the first organic solution under constant stirring. During addition of the two solutions additional acetone was added as necessary to maintain complete dissolution of the nafcillin. The final solution was then transferred to 500 ml amber glass jar and to this was added slowly 60 ml of a 1% PVA solution in sterile filtered DI H₂O. This solution was then cooled on ice for five minutes. Following this the solution was then emulsified using the highest setting of a whole cell homogenizer for 10 min resulting in a milky white emulsion. This emulsion was then transferred to a 250 ml beaker and stirred uncovered at room temperature for 72 hrs resulting in the evaporation of the organics. These particles were then purified and collected using two distinct methods.

Method 1: NPs were purified by centrifugation (25 min, 30,000 × g) using three successive washes of sterile filtered 18 Ω water at 4 °C. The resulting NP pellet was then resuspended into sterile filtered 18 Ω water (100 ml), whereupon dextrose (100 mg) was added as a lyoprotectant. This colloidal suspension was then divided into 25 ml volumes and placed in four 50 ml round bottom flasks, then flash frozen in liquid nitrogen lyophilized at RT and 50 mTorr for 24 - 48 hrs resulting in a flocculent white solid.

Method 2: NPs were then purified by centrifugation following precipitating of the particles with sat. NaCl (aq). This process was repeated three times. The resulting NP pellet was then resuspended into sterile filtered 18 Ω water (100 ml), whereupon dextrose (100 mg) was added as a lyoprotectant. This colloidal suspension was then divided into 25 ml volumes and placed in four 50 ml round bottom flasks, then flash frozen in liquid nitrogen lyophilized at RT and 50 mTorr for 24 - 48 hrs resulting in a flocculent white solid.

Preparation of Positively Charged Nafcillin Loaded PLGA Nanoparticles. Cationic NPs composed of PLGA were prepared using the nanoprecipitation method. Nanoparticles (NPs) were prepared by the nanoprecipitation method. Briefly; 250 mg of PLGA (50:50, $M_w \sim 20$ K), and 12.5 mg of nafcillin free acid was dissolved into 25 ml of acetone. This solution was then added dropwise via syringe into a stirred solution of 1% PVA (50 ml) at a rate of 90 ml/hr controlled using a syringe pump. The resulting colloidal suspension was then transferred to a 250 ml round-bottom flask, and the acetone removed under reduced pressure using a rotary evaporator. NPs were then purified by centrifugation following precipitating of the particles with sat. NaCl (aq). This process was repeated three times. The resulting NP pellet was then resuspended into sterile filtered 18 Ω water (25 ml) dialyzed to remove the salt. These particles were then incubated with 25 mg of CTAB for 24 hrs. at RT Following this the NPs were purified of excess CTAB through three sequential washing steps performed as previously described. Finally, NPs were resuspended into sterile filtered 18 Ω water (25 ml), whereupon dextrose (25 mg) was added as a lyoprotectant. This colloidal suspension was then added to a clean 50 ml round

bottom flask and flash frozen in liquid nitrogen then lyophilized at 25 °C and 50 mTorr for 24 - 48 hrs resulting in a flocculent solid.

Determination of NP loading. 20 mg of NP sample were dissolved into 600 μ l of DMSO-*d*₆ and the concentration of the respective cargo determined using ¹H NMR at 25 °C by comparing unique resonances of the cargo to the methylene residue of PLGA at [5.2 ppm].

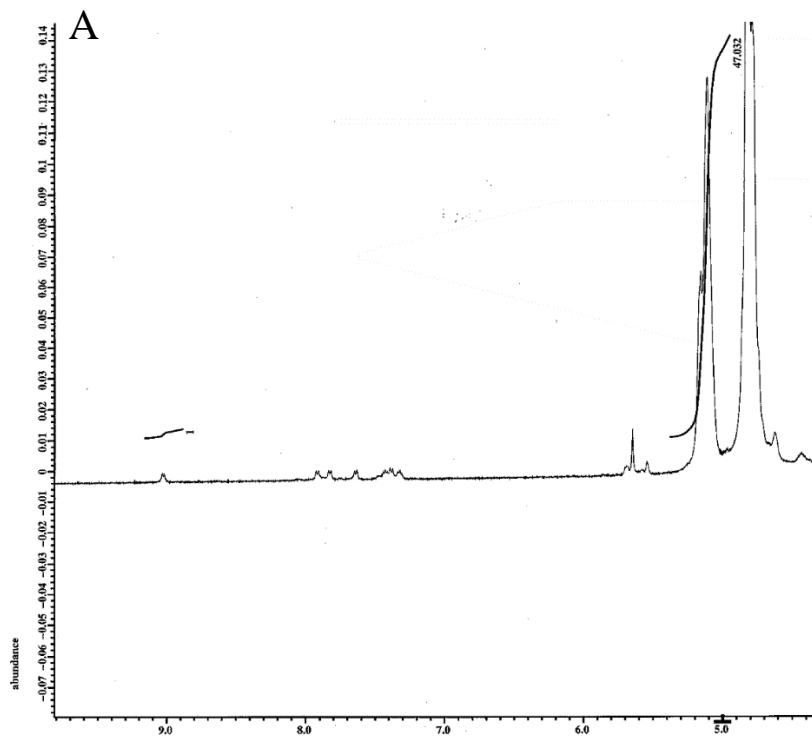


Figure. 5.3. ¹H NMR (DMSO-*d*₆, 500 MHz) used for determining nafcillin concentration in (-) nafcillin NPs.

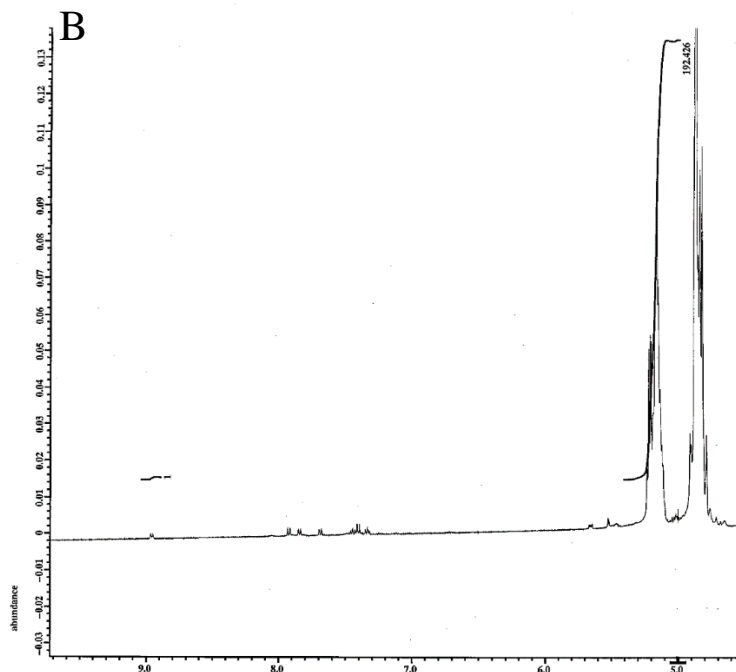


Figure. 5.4. ^1H NMR (DMSO- d_6 , 500 MHz) used for determining nafcillin concentration in (+) nafcillin NPs.

Biological Results. All biological studies were furnished by Bayer Animal Health, Germany. Animal studies were performed in accordance within institutional parameters of Bayer Animal health using a modified chronic mouse model of mastitis (MCMMM) (Fig. 5.5). Briefly; lactating mice were used for the induction of intramammary infection. The pups were removed 1 hr. before bacterial inoculation of mammary glands. Following a 1 hr. incubation, the pups were returned to the mother for approximately 2 hrs. at which time they were removed again 1 hr. prior to therapeutic treatment. Following a 2 hr. period, pups were once again returned to the mother for the remainder of the 68 hr. therapeutic exposure. Upon completion of the treatment period, pups were removed from the mother, the mother sacrificed, and the glands harvested.

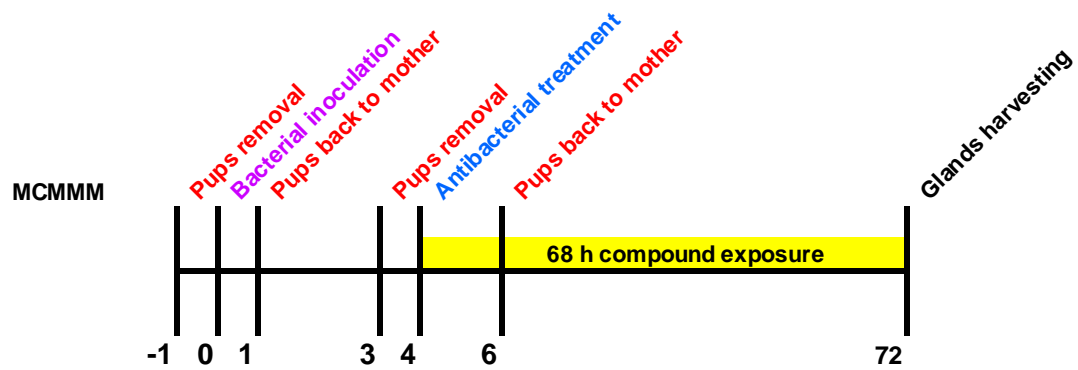


Figure. 5.5. Experimental design for the MCMMM.

REFERENCES

1. E. Silverberg and A. I. Holleb, *CA Cancer J Clin*, 1975, **25**, 2-8.
2. in *Health, United States, 2016: With Chartbook on Long-term Trends in Health*, Hyattsville (MD), 2017.
3. *American Cancer Society*, 71.
4. G. Xu and H. L. McLeod, *Clin Cancer Res*, 2001, **7**, 3314-3324.
5. V. V. Padma, *Biomedicine (Taipei)*, 2015, **5**, 19.
6. J. Shi, P. W. Kantoff, R. Wooster and O. C. Farokhzad, *Nat Rev Cancer*, 2017, **17**, 20-37.
7. Y. Barenholz, *J Control Release*, 2012, **160**, 117-134.
8. J. S. James, *AIDS Treat News*, 1995, 6.
9. O. K. Nag and V. Awasthi, *Pharmaceutics*, 2013, **5**, 542-569.
10. H. I. Chang and M. K. Yeh, *Int J Nanomedicine*, 2012, **7**, 49-60.
11. M. N. Kundranda and J. Niu, *Drug Des Devel Ther*, 2015, **9**, 3767-3777.
12. D. Bobo, K. J. Robinson, J. Islam, K. J. Thurecht and S. R. Corrie, *Pharm Res*, 2016, **33**, 2373-2387.
13. O. C. Farokhzad and R. Langer, *ACS Nano*, 2009, **3**, 16-20.
14. A. Kumari, S. K. Yadav and S. C. Yadav, *Colloids Surf B Biointerfaces*, 2010, **75**, 1-18.
15. F. Masood, *Mater Sci Eng C Mater Biol Appl*, 2016, **60**, 569-578.
16. S. Parveen and S. K. Sahoo, *J Drug Target*, 2008, **16**, 108-123.
17. J. W. Hickey, J. L. Santos, J. M. Williford and H. Q. Mao, *J Control Release*, 2015, **219**, 536-547.
18. J. L. Perry, K. P. Herlihy, M. E. Napier and J. M. Desimone, *Acc Chem Res*, 2011, **44**, 990-998.
19. K. S. Chu, A. N. Schorzman, M. C. Finnis, C. J. Bowerman, L. Peng, J. C. Luft, A. J. Madden, A. Z. Wang, W. C. Zamboni and J. M. DeSimone, *Biomaterials*, 2013, **34**, 8424-8429.
20. D. Brambilla, R. Verpillot, B. Le Droumaguet, J. Nicolas, M. Taverna, J. Kona, B. Lettiero, S. H. Hashemi, L. De Kimpe, M. Canovi, M. Gobbi, V. Nicolas, W. Scheper, S. M. Moghimi, I. Tvaroska, P. Couvreur and K. Andrieux, *ACS Nano*, 2012, **6**, 5897-5908.
21. S. W. Choi, W. S. Kim and J. H. Kim, *Methods Mol Biol*, 2005, **303**, 121-131.
22. S. Dhar, F. X. Gu, R. Langer, O. C. Farokhzad and S. J. Lippard, *Proc Natl Acad Sci U S A*, 2008, **105**, 17356-17361.
23. O. C. Farokhzad, J. Cheng, B. A. Teply, I. Sherifi, S. Jon, P. W. Kantoff, J. P. Richie and R. Langer, *Proc Natl Acad Sci U S A*, 2006, **103**, 6315-6320.
24. W. Gao, J. M. Chan and O. C. Farokhzad, *Mol Pharm*, 2010, **7**, 1913-1920.
25. J. S. Suk, Q. Xu, N. Kim, J. Hanes and L. M. Ensign, *Adv Drug Deliv Rev*, 2016, **99**, 28-51.
26. P. Ruenraroengsak and T. D. Tetley, *Part Fibre Toxicol*, 2015, **12**, 19.
27. E. A. Warren and C. K. Payne, *RSC Adv*, 2015, **5**, 13660-13666.

28. F. Danhier, E. Ansorena, J. M. Silva, R. Coco, A. Le Breton and V. Preat, *J Control Release*, 2012, **161**, 505-522.
29. N. Kamaly, B. Yameen, J. Wu and O. C. Farokhzad, *Chem Rev*, 2016, **116**, 2602-2663.
30. R. Gref, A. Domb, P. Quellec, T. Blunk, R. H. Muller, J. M. Verbavatz and R. Langer, *Adv Drug Deliv Rev*, 1995, **16**, 215-233.
31. B. D. Ulery, L. S. Nair and C. T. Laurencin, *J Polym Sci B Polym Phys*, 2011, **49**, 832-864.
32. D. W. H. Maria AnnWoodruff, *Progress in Polymer Science*, 2010, **35**, 39.
33. M. Labet and W. Thielemans, *Chem Soc Rev*, 2009, **38**, 3484-3504.
34. X. Q. Zhang, X. Xu, N. Bertrand, E. Pridgen, A. Swami and O. C. Farokhzad, *Adv Drug Deliv Rev*, 2012, **64**, 1363-1384.
35. Y. Nakamura, A. Mochida, P. L. Choyke and H. Kobayashi, *Bioconjug Chem*, 2016, **27**, 2225-2238.
36. K. Greish, *Methods Mol Biol*, 2010, **624**, 25-37.
37. H. Kobayashi, R. Watanabe and P. L. Choyke, *Theranostics*, 2013, **4**, 81-89.
38. S. Zhang, J. Li, G. Lykotrafitis, G. Bao and S. Suresh, *Adv Mater*, 2009, **21**, 419-424.
39. S. D. Steichen, M. Caldorera-Moore and N. A. Peppas, *Eur J Pharm Sci*, 2013, **48**, 416-427.
40. S. E. Gratton, P. A. Ropp, P. D. Pohlhaus, J. C. Luft, V. J. Madden, M. E. Napier and J. M. DeSimone, *Proc Natl Acad Sci U S A*, 2008, **105**, 11613-11618.
41. H. Meng, S. Yang, Z. Li, T. Xia, J. Chen, Z. Ji, H. Zhang, X. Wang, S. Lin, C. Huang, Z. H. Zhou, J. I. Zink and A. E. Nel, *ACS Nano*, 2011, **5**, 4434-4447.
42. A. M. Scott, J. P. Allison and J. D. Wolchok, *Cancer Immun*, 2012, **12**, 14.
43. R. Seigneuric, J. Gobbo, P. Colas and C. Garrido, *Oncotarget*, 2011, **2**, 557-561.
44. G. Zhou, G. Wilson, L. Hebbard, W. Duan, C. Liddle, J. George and L. Qiao, *Oncotarget*, 2016, **7**, 13446-13463.
45. A. Huang, S. J. Kennel and L. Huang, *J Biol Chem*, 1983, **258**, 14034-14040.
46. J. Connor and L. Huang, *J Cell Biol*, 1985, **101**, 582-589.
47. S. M. Sullivan and L. Huang, *Biochim Biophys Acta*, 1985, **812**, 116-126.
48. J. Connor, N. Norley and L. Huang, *Biochim Biophys Acta*, 1986, **884**, 474-481.
49. N. Karra, T. Nassar, A. N. Ripin, O. Schwob, J. Borlak and S. Benita, *Small*, 2013, **9**, 4221-4236.
50. F. Fay and C. J. Scott, *Immunotherapy*, 2011, **3**, 381-394.
51. T. Carter, P. Mulholland and K. Chester, *Immunotherapy*, 2016, **8**, 941-958.
52. C. Yu, Y. Hu, J. Duan, W. Yuan, C. Wang, H. Xu and X. D. Yang, *PLoS One*, 2011, **6**, e24077.
53. D. Arosio, L. Manzoni, E. M. Araldi and C. Scolastico, *Bioconjug Chem*, 2011, **22**, 664-672.
54. L. D. Field, J. B. Delehanty, Y. Chen and I. L. Medintz, *Acc Chem Res*, 2015, **48**, 1380-1390.
55. E. J. Chung, *Exp Biol Med (Maywood)*, 2016, **241**, 891-898.
56. S. A. Kularatne and P. S. Low, *Methods Mol Biol*, 2010, **624**, 249-265.
57. A. Akinc and G. Battaglia, *Cold Spring Harb Perspect Biol*, 2013, **5**, a016980.

58. I. Sassoon and V. Blanc, *Methods Mol Biol*, 2013, **1045**, 1-27.
59. A. Beck, L. Goetsch, C. Dumontet and N. Corvaia, *Nat Rev Drug Discov*, 2017, **16**, 315-337.
60. S. Farkona, E. P. Diamandis and I. M. Blasutig, *BMC Med*, 2016, **14**, 73.
61. B. Yu, H. C. Tai, W. Xue, L. J. Lee and R. J. Lee, *Mol Membr Biol*, 2010, **27**, 286-298.
62. B. Zhang, S. Shen, Z. Liao, W. Shi, Y. Wang, J. Zhao, Y. Hu, J. Yang, J. Chen, H. Mei, Y. Hu, Z. Pang and X. Jiang, *Biomaterials*, 2014, **35**, 4088-4098.
63. E. Basle, N. Joubert and M. Pucheault, *Chem Biol*, 2010, **17**, 213-227.
64. G. T. Hermanson, *Bioconjugate techniques*, Elsevier/AP, London ; Waltham, MA, Third edition. edn., 2013.
65. S. Ursuegui, R. Yougnia, S. Moutin, A. Burr, C. Fossey, T. Cailly, A. Laayoun, A. Laurent and F. Fabis, *Org Biomol Chem*, 2015, **13**, 3625-3632.
66. S. Ursuegui, N. Chivot, S. Moutin, A. Burr, C. Fossey, T. Cailly, A. Laayoun, F. Fabis and A. Laurent, *Chem Commun (Camb)*, 2014, **50**, 5748-5751.
67. K. E. Deigan, T. W. Li, D. H. Mathews and K. M. Weeks, *Proc Natl Acad Sci U S A*, 2009, **106**, 97-102.
68. K. M. Weeks and D. M. Mauger, *Acc Chem Res*, 2011, **44**, 1280-1291.
69. M. J. Smola, J. M. Calabrese and K. M. Weeks, *Biochemistry*, 2015, **54**, 6867-6875.
70. C. S. McKay and M. G. Finn, *Chem Biol*, 2014, **21**, 1075-1101.
71. J. E. Hein and V. V. Fokin, *Chem Soc Rev*, 2010, **39**, 1302-1315.
72. H. K. H. Jr., *Journal of the American Chemical Society*, 1957, **79**.
73. D. R. Lide, *CRC Handbook of Chemistry and Physics* CRC Press, Boca Raton, FL, 72 edn., 1991.
74. E. J. Merino, K. A. Wilkinson, J. L. Coughlan and K. M. Weeks, *J Am Chem Soc*, 2005, **127**, 4223-4231.
75. V. Hong, S. I. Presolski, C. Ma and M. G. Finn, *Angew Chem Int Ed Engl*, 2009, **48**, 9879-9883.
76. K. Sivakumar, F. Xie, B. M. Cash, S. Long, H. N. Barnhill and Q. Wang, *Org Lett*, 2004, **6**, 4603-4606.
77. ThermoFisher.
78. P. J. Bracher, P. W. Snyder, B. R. Bohall and G. M. Whitesides, *Orig Life Evol Biosph*, 2011, **41**, 399-412.
79. J. Kalia and R. T. Raines, *Chembiochem*, 2006, **7**, 1375-1383.
80. J. Franke and C. Hertweck, *Cell Chem Biol*, 2016, **23**, 1179-1192.
81. E. C. Johnson and S. B. Kent, *J Am Chem Soc*, 2006, **128**, 6640-6646.
82. L. R. Malins and R. J. Payne, *Top Curr Chem*, 2015, **362**, 27-87.
83. Cancer.net.
84. M. Waghay, M. Yalamanchili, M. P. di Magliano and D. M. Simeone, *Curr Opin Gastroenterol*, 2013, **29**, 537-543.
85. M. Erkan, S. Hausmann, C. W. Michalski, A. A. Fingerle, M. Dobritz, J. Kleeff and H. Friess, *Nat Rev Gastroenterol Hepatol*, 2012, **9**, 454-467.
86. A. Teague, K. H. Lim and A. Wang-Gillam, *Ther Adv Med Oncol*, 2015, **7**, 68-84.

87. T. Conroy, F. Desseigne, M. Ychou, O. Bouche, R. Guimbaud, Y. Becouarn, A. Adenis, J. L. Raoul, S. Gourgou-Bourgade, C. de la Fouchardiere, J. Bennouna, J. B. Bachet, F. Khemissa-Akouz, D. Pere-Verge, C. Delbaldo, E. Assenat, B. Chauffert, P. Michel, C. Montoto-Grillot, M. Ducreux, U. Groupe Tumeurs Digestives of and P. Intergroup, *N Engl J Med*, 2011, **364**, 1817-1825.
88. M. Tehfe, S. Dowden, H. Kennecke, R. El-Maraghi, B. Lesperance, F. Couture, R. Letourneau, H. Liu and A. Romano, *Adv Ther*, 2016, **33**, 747-759.
89. L. F. Dodson, W. G. Hawkins and P. Goedegebuure, *Immunotherapy*, 2011, **3**, 517-537.
90. M. A. Cheever, J. P. Allison, A. S. Ferris, O. J. Finn, B. M. Hastings, T. T. Hecht, I. Mellman, S. A. Prindiville, J. L. Viner, L. M. Weiner and L. M. Matrisian, *Clin Cancer Res*, 2009, **15**, 5323-5337.
91. S. Nath and P. Mukherjee, *Trends Mol Med*, 2014, **20**, 332-342.
92. R. Kumar, A. Kulkarni, J. Nabulsi, D. K. Nagesha, R. Cormack, M. G. Makrigiorgos and S. Sridhar, *Drug Deliv Transl Res*, 2013, **3**, 299-308.
93. F. Danhier, N. Lecouturier, B. Vroman, C. Jerome, J. Marchand-Brynaert, O. Feron and V. Preat, *J Control Release*, 2009, **133**, 11-17.
94. C. Fonseca, S. Simoes and R. Gaspar, *J Control Release*, 2002, **83**, 273-286.
95. E. Bernabeu, L. Gonzalez, M. J. Legaspi, M. A. Moretton and D. A. Chiappetta, *J Nanosci Nanotechnol*, 2016, **16**, 160-170.
96. P. Ma and R. J. Mumper, *J Nanomed Nanotechnol*, 2013, **4**, 1000164.
97. M. L. Amin, D. Kim and S. Kim, *Eur J Pharm Sci*, 2016, **91**, 138-143.
98. N. Graf, D. R. Bielenberg, N. Kolishetti, C. Muus, J. Banyard, O. C. Farokhzad and S. J. Lippard, *ACS Nano*, 2012, **6**, 4530-4539.
99. A. Sahu, U. Bora, N. Kasoju and P. Goswami, *Acta biomaterialia*, 2008, **4**, 1752-1761.
100. J. J. Kamphorst, M. Nofal, C. Commisso, S. R. Hackett, W. Lu, E. Grabocka, M. G. Vander Heiden, G. Miller, J. A. Drebin, D. Bar-Sagi, C. B. Thompson and J. D. Rabinowitz, *Cancer research*, 2015, **75**, 544-553.
101. C. M. Sousa and A. C. Kimmelman, *Carcinogenesis*, 2014, **35**, 1441-1450.
102. V. K. Sarin, S. B. H. Kent, J. P. Tam and R. B. Merrifield, *Analytical Biochemistry*, 1981, **117**, 147-157.
103. F. A. Shiekh, *Int J Nanomedicine*, 2014, **9**, 1627-1628.
104. M. Grzelczak, J. Vermant, E. M. Furst and L. M. Liz-Marzan, *ACS Nano*, 2010, **4**, 3591-3605.
105. R. Tong and J. Cheng, *Macromolecules*, 2012, **45**, 2225-2232.
106. D. Trung Bui, A. Maksimenko, D. Desmaele, S. Harrisson, C. Vauthier, P. Couvreur and J. Nicolas, *Biomacromolecules*, 2013, **14**, 2837-2847.
107. H. Sun, L. Mei, C. Song, X. Cui and P. Wang, *Biomaterials*, 2006, **27**, 1735-1740.
108. D. D. Stéphanie Gazeau-Bureau, Blanca Martín-Vaca, Didier Bourissou, Christophe Navarro, Stéphanie Magnet, *Macromolecules*, 2008, **41**, 3782-3784.
109. Q. Fu, Y. Wang, Y. Ma, D. Zhang, J. K. Fallon, X. Yang, D. Liu, Z. He and F. Liu, *Sci Rep*, 2015, **5**, 12023.

110. E. W. Damen, P. H. Wiegerinck, L. Braamer, D. Sperling, D. de Vos and H. W. Scheeren, *Bioorg Med Chem*, 2000, **8**, 427-432.
111. F. M. de Groot, L. W. van Berkomp and H. W. Scheeren, *J Med Chem*, 2000, **43**, 3093-3102.
112. C. Jin, S. Wen, Q. Zhang, Q. Zhu, J. Yu and W. Lu, *ACS Med Chem Lett*, 2017, **8**, 762-765.
113. M. Gund, A. Khanna, N. Dubash, A. Damre, K. S. Singh and A. Satyam, *Bioorg Med Chem Lett*, 2015, **25**, 122-127.
114. X. He, W. Lu, X. Jiang, J. Cai, X. Zhang and J. Ding, *Bioorg Med Chem*, 2004, **12**, 4003-4008.
115. M. Ramasamy and J. Lee, *Biomed Res Int*, 2016, **2016**, 1851242.
116. E. Taylor and T. J. Webster, *Int J Nanomedicine*, 2011, **6**, 1463-1473.
117. Y. C. Chang, C. Y. Yang, R. L. Sun, Y. F. Cheng, W. C. Kao and P. C. Yang, *Sci Rep*, 2013, **3**, 1863.
118. A. F. Radovic-Moreno, T. K. Lu, V. A. Puscasu, C. J. Yoon, R. Langer and O. C. Farokhzad, *ACS Nano*, 2012, **6**, 4279-4287.
119. L. Wang, C. Hu and L. Shao, *Int J Nanomedicine*, 2017, **12**, 1227-1249.
120. R. Abebe, H. Hatiya, M. Abera, B. Megersa and K. Asmare, *BMC Vet Res*, 2016, **12**, 270.
121. C. Viguier, S. Arora, N. Gilmartin, K. Welbeck and R. O'Kennedy, *Trends Biotechnol*, 2009, **27**, 486-493.
122. S. Pyorala, *Ir Vet J*, 2009, **62 Suppl 4**, S40-44.
123. J. R. Middleton, J. Ma, C. L. Rinehart, V. N. Taylor, C. D. Luby and B. J. Steevens, *J Dairy Res*, 2006, **73**, 10-19.
124. H. Landin, M. J. Mork, M. Larsson and K. P. Waller, *Acta Vet Scand*, 2015, **57**, 81.
125. A. J. Bradley, J. E. Breen, B. Payne, V. White and M. J. Green, *J Dairy Sci*, 2015, **98**, 1706-1720.
126. P. V. D. Chandrasekaran, K. G. Tirumurugaan, A. P. Nambi, P. S. Thirunavukkarasu, K. Kumanan, and S. R. S. Vairamuthu, *Veterinary World*, 2014, **7**, 389-394.
127. B. G. T. Eric Brouillette, François Malouin, *INFECTIO AND IMMUNITY*, 2003, **71**, 2292-2295.
128. D. S. Bouchard, L. Rault, N. Berkova, Y. Le Loir and S. Even, *Appl Environ Microbiol*, 2013, **79**, 877-885.
129. R. N. Zadoks, J. R. Middleton, S. McDougall, J. Katholm and Y. H. Schukken, *J Mammary Gland Biol Neoplasia*, 2011, **16**, 357-372.
130. C. A. Fromen, G. R. Robbins, T. W. Shen, M. P. Kai, J. P. Ting and J. M. DeSimone, *Proc Natl Acad Sci U S A*, 2015, **112**, 488-493.
131. W. Zou, C. Liu, Z. Chen and N. Zhang, *Nanoscale Res Lett*, 2009, **4**, 982-992.
132. R. R. Pillai, S. N. Somayaji, M. Rabinovich, M. C. Hudson and K. E. Gonsalves, *Biomed Mater*, 2008, **3**, 034114.